Climate Variability of Seasonal Wind Extreme Events in North America

by

Ameneh Mollasharifi Targhi
B.Sc., University of Tehran, 2010
M.Sc., University of Tehran, 2018

A Dissertation Submitted in Partial Fulfillment of the
Requirements for the Degree of

MASTER OF SCIENCE

in the School of Earth and Ocean Sciences

Climate Variability of Seasonal Wind Extreme Events in North America

by

Ameneh Mollasharifi Targhi
B.Sc., University of Tehran, 2010
M.Sc., University of Tehran, 2018

Supervisory Committee

Dr. Adam H. Monahan, Supervisor
(School of Earth and Ocean Sciences, University of Victoria)

Dr. Roberta C. Hamme, Departmental Member
(School of Earth and Ocean Sciences, University of Victoria)

Dr. Tara J. Troy, Outside Member
(Department of Civil Engineering, University of Victoria)

Supervisory Committee

Dr. Adam H. Monahan, Supervisor
(School of Earth and Ocean Sciences, University of Victoria)

Dr. Roberta C. Hamme, Departmental Member
(School of Earth and Ocean Sciences, University of Victoria)

Dr. Tara J. Troy, Outside Member
(Department of Civil Engineering, University of Victoria)

ABSTRACT

This study investigates the climate variability and seasonal predictability of large-scale wind extreme events across North America, with a particular focus on their relationship with Pacific sea surface temperature (SST) patterns. Wind Droughts (WD) and Wind Floods (WF) are defined as prolonged seasonal anomalies in surface wind speed, with substantial implications for climate science and renewable energy systems. Using large ensembles of historical simulations from three climate models (CanESM2, CanRCM4, and CESM2), the frequency, spatial distribution, and predictability of these extreme events are analyzed across six North American regions.

Time-series analysis reveals that WF events occur most frequently in northern regions during winter, while WD events are more prevalent in southern regions during summer. Composite wind and SST anomaly maps indicate distinct and largely opposing patterns associated with WF and WD events in most regions in North America. WD events are characterized by a band of warm anomalies in the Gulf of Alaska—occasionally extending into the subtropical and tropical Pacific—coupled with a contrasting band of cold anomalies spanning from Asia to the eastern Pacific, whereas WF events display the opposite pattern. In the Southeast of North America (SENA), however, wind extremes exhibit a localized response with a reversed SST pattern, likely tied to the Pacific–North American (PNA) pattern.

Furthermore, our evaluation of the predictive skill of Pacific SST anomalies shows that WF events are more predictable than WD events, with extratropical Pacific SST anomalies enhancing predictability more effectively than equatorial or full-basin SST patterns. Importantly, the relationships between SST patterns and WD/WF events are predominantly statistically significant at the 5% level, further bolstering confidence in SST-based seasonal predictability. These findings provide new insights into the large-scale drivers of wind extremes and their seasonal predictability, offering valuable implications for renewable energy resource management and climate modeling.

Contents

List of Tables

List of Figures

ACKNOWLEDGEMENTS

I would like to express my sincere gratitude to my **supervisor, Prof. Adam Monahan**, for his invaluable guidance, insightful feedback, and continuous support throughout this research.

A special thank you goes to my **parents** for their endless encouragement, and to my **husband, Naser**, whose love, understanding, and unwavering support—especially in caring for our daughter—made this journey possible. Most of all, to my **daughter, Leili**, who accompanied me through almost half of this program and patiently endured our time apart during her early months.

I am also deeply grateful to my **colleagues and friends** for their encouragement and the moments of camaraderie that made this journey more enriching.

Finally, I extend my appreciation to the **School of Earth and Ocean Sciences** and the **Faculty of Graduate Studies at the University of Victoria** for their generous awards and scholarship support.

This journey has been both challenging and rewarding, and I am profoundly grateful to everyone who has been a part of it.

DEDICATION

To my little Leili, who has been with me on this journey from the very beginning of her life. Your patience, laughter, and presence have been my greatest source of strength and motivation. Though we spent time apart in your early months, your love has always been with me, guiding me through every challenge. This work stands as a testament to the resilience, joy, and unconditional love you have brought into my life.

Chapter 1

Introduction

Wind extreme events are important phenomena in the Earth's climate system, with wide-ranging implications across various sectors, including energy systems. As the global transition to renewable energy accelerates, wind energy has emerged as a cornerstone of sustainable energy transitions, offering a clean and effective pathway for mitigating climate change through the decarbonization of power production. However, wind energy production depends heavily on the availability of wind resources, which exhibit large temporal and spatial variability across multiple scales. Temporal variability ranges from seconds to millennia, while spatial variability spans from specific locations (e.g., stations or sites) to large regions. These variations arise from the physical processes governing each scale and the extreme events associated with them, contributing to the inherent uncertainty in studying such phenomena. This study focuses on large-scale structures of variability, specifically seasonal and regional surface wind anomalies.

Over the past several decades, substantial long-term variability in surface wind speeds has been observed across North America, attracting considerable scholarly attention. Studies have identified variability on monthly, seasonal, and interannual timescales, often linked to large-scale circulation patterns and modes of climate variability. Pryor et al. (2009) conducted an extensive intercomparison of wind speed trends across the contiguous United States, focusing on the late 20th and early 21st centuries. Their study utilized two observational datasets, four reanalysis datasets, and outputs from two regional climate models (RCMs). They identified substantial discrepancies in the temporal trends across these eight datasets. Moreover, they performed a trend analysis of annual mean wind speed as well as of interannual variability, the latter defined as the standard deviation of the seven-year annual mean

wind speeds. They concluded that there was no clear consensus on whether changes in the annual mean wind speed were linked to shifts in interannual variability. Wan et al. (2010) assessed monthly mean near-surface wind speeds recorded at 117 stations across Canada from 1953 to 2006, and found notable wind decreases throughout western Canada and most of southern Canada (excluding the Maritimes) in all seasons, with substantial increases observed in the central Canadian Arctic in all seasons and in the Maritimes during spring and autumn. Tuller (2004) explored interannual and seasonal trends in mean wind speeds at four land stations along the west coast of Canada. Their analysis revealed a decline in annual and winter wind speeds at three stations, while one station saw an increase. They noted that the changes are in line with large-scale climate variability such as Pacific Decadal Oscillation (PDO) and the Pacific-North American (PNA) pattern. Klink et al. (2003) examined interannual (and hourly) variability of 70 m wind speeds from five tall-tower sites in Minnesota during the late twentieth century and suggested that large-scale circulation patterns contribute significantly to the variability of turbine-level wind speeds. St. George and Wolfe (2009) used a network of quality-controlled wind records to examine interannual and monthly mean near-surface wind variations in the southern Canadian Prairies since the mid-1950s at six locations, two in Alberta and four in Saskatchewan. They identified a correlation between the low wind years and El Niño events, suggesting the potential for seasonal or interannual predictability in regional wind energy production. Lledó et al. (2018) investigated a severe decline in surface wind speed across the United States during the first quarter of 2015 and examined the role of sea surface temperature (SST) in the western tropical Pacific Ocean in driving wind anomalies. Pryor et al. (2020) reviewed the magnitude and variability of wind resources around the globe and provided evidence for increased wind energy resources by the end of the current century in the US Southern Great Plains. Collectively, these studies highlight the interannual variability of wind speed across North America, which complicates reliable wind energy output.

Climate model projections suggest that seasonal anomalies in wind power potential may intensify by the end of the century. Using historical and projected wind speed data from seven global climate models in the CMIP6, Qian and Zhang (2021) concluded that wind energy resources in the region south of the Northwest Passage would decrease by more than 20%, while resources in northern regions (north of 72°N) would increase. Wang et al. (2020) examined onshore and offshore wind power densities in Ontario using a high-resolution regional climate model. They found

that wind speed along Great Lakes shorelines, where many wind farms are located, would decrease, while offshore wind production would increase, recommending an expansion of offshore wind farms to meet Ontario's future energy needs. Expanding the analysis to a national scale, Ma et al. (2022) used a higher resolution RCM (convection-permitting Weather Research Forecasting simulations) to assess variations in Canadian wind power production. They found that although the spatial distribution of annual wind power density is not expected to change substantially by the end of the century, seasonal variations will occur, with winter emerging as the primary season contributing to changes in wind power density. The study also highlighted that regions near the Great Lakes in southern Ontario, the Southeast coast, and northern Quebec will remain suitable for wind energy development due to their high wind power density and growing extractable potential, while most of Canada will experience a decline in wind energy potential in the future. Given the sensitivity of wind power density and extractable wind energy to extreme events on seasonal timescales, the authors recommend future research focus on analyzing seasonal and spatial variations in extreme wind events. Using seasonal prediction products from a climate model (15 ensemble members of SPEAR's SRF), and analyzing interannual variations of El Niño-Southern Oscillation in the tropical Pacific, Yang et al. (2024) assessed seasonal prediction skill of wind energy resources over the U.S. Great Plains during peak energy seasons (winter and spring), using El Niño–Southern Oscillation (ENSO) variations, demonstrating the potential for seasonal predictability in wind energy resources.

Prolonged wind extremes, lasting several months, pose substantial risks to power production. For instance, a 150 W/m^2 reduction in wind power potential can severely impact regional energy output (St. George and Wolfe, 2009). Such risks are particularly acute in regions that rely heavily on wind energy, such as the North American wind corridor spanning from Texas through the Great Plains (Zinaman et al., 2015; St. George and Wolfe, 2009). The interannual variability of wind speeds in these regions further complicates predictability. Therefore, understanding large-scale seasonal anomalies in wind speeds and their drivers is essential for mitigating potential risks to energy facilities, managing resources effectively, ensuring the sustainability of wind energy systems, and supporting the reliable integration of wind energy into power grids amid changing climate conditions.

Large-scale atmospheric-oceanic interactions, particularly those associated with SST anomalies, play a central role in driving remote wind extreme events. SST pat-

terns, particularly in the Pacific Ocean, influence large-scale atmospheric circulation patterns such as storm tracks and and jet stream, ultimately modulating surface wind speeds across North America. For example, SST anomalies in the Equatorial Pacific associated with ENSO or in the North Pacific linked to the PDO are known to influence seasonal atmospheric patterns (Baxter and Nigam, 2015; Bellprat et al., 2016; Hartmann, 2015; Hartmann and Wendler, 2005; L'Heureux and Thompson, 2006; Lledó et al., 2018; McCabe et al., 2004; St. George and Wolfe, 2009; Yang et al., 2024), altering the likelihood of extreme wind events. Given the inherent variability and unpredictability of wind fields, connecting wind variability to slowly evolving components of the climate system is essential for improving the predictability of extreme events. Therefore, analyzing SST variability and its effects on wind resources can enhance our ability to forecast wind events.

Evidence from studies such as St. George and Wolfe (2009), Hartmann (2015), and Lledó et al. (2018) suggests that Pacific SST anomalies can drive large seasonal anomalies in surface wind across North America. However, despite the importance of these observational findings, the connection between SST and wind anomalies remains uncertain. In situ measurements are often sparse and subject to large inhomogeneities, making it difficult to analyze the robustness of the teleconnection's impacts from an instrumental perspective. Furthermore, extreme events, due to their infrequency, present a particular challenge to be robustly studied or replicated with limited observations. Reanalysis products, which integrate observational data with numerical models to provide consistent historical datasets, offer valuable insights into these relationships but are also limited by their relatively short temporal coverage. Earth System Models (ESMs), on the other hand, provide state-of-the-art tools to simulate these processes multiple times, enabling a more comprehensive exploration of complex large-scale ocean-atmosphere interactions.

Extreme events, being inherently rare, are particularly difficult to analyze using a single model realization, as it may fail to capture any occurrences of such events. Additionally, relying on a single realization is insufficient to fully represent natural climate variability, a major source of uncertainty in climate projections. Large ensembles of climate simulations, generated by running multiple realizations of the same experiment in an ESM or RCM by introducing slight perturbations to the model's initial conditions, offer a powerful approach to robustly capturing extreme events. By substantially increasing the sample size through replicating multiple realizations under the same natural and anthropogenic forcing, large ensembles enhance the ability to

detect rare events and reduce the uncertainty associated with the chaotic nature of the climate system (Deser et al., 2012a,b, 2014; Karmalkar, 2018; Kay et al., 2015; Kushner et al., 2018). Given structural differences between climate models and variability in parameterizations, incorporating multiple large ensembles from different models—when available—is essential for studying extreme events and assessing the robustness of wind-SST relationships.

This study explores extremes in large-scale seasonal mean surface wind speeds, focusing on periods characterized by prolonged anomalously high and low wind activity, referred to as Wind Flood (WF) and Wind Drought (WD) events, respectively. In this context, extreme events are defined based on seasonal mean quantities, rather than on instantaneous or sub-daily wind extremes commonly used in weather-based analyses. The analysis spans six large regions across North America and investigates the influence of SST anomalies on seasonal and regional variability in wind extremes. A key objective is to evaluate the robustness of SST-wind relationships using large ensembles of historical simulations (1950-2000) from multiple climate models. The study also aims to improve the understanding of the predictability of wind extremes across diverse geographic regions and to assess the consistency of results across different modeling frameworks. Ultimately, the findings contribute to the advancement of scientific knowledge and inform practical strategies for climate adaptation and mitigation.

To support this analysis, the study employs large ensemble simulations from the Canadian Earth System Model version 2 (CanESM2), the Canadian Regional Climate Model (CanRCM4), and the Community Earth System Model (CESM). Although more recent versions of CanESM are available, CanESM2 was selected due to its direct use in driving the CanRCM4 ensemble. This shared modeling framework enables a robust comparison between global and regional simulations, allowing for the assessment of how increased spatial resolution influences the representation of wind fields and their relationships with SST anomalies.

Previous studies, as discussed earlier in this section, have explored the connections between wind variability and SST patterns. However, these studies often focus on interannual variability of seasonal means rather than extreme events and typically examine limited locations rather than large regions. Those studies that address extreme events in broader regions tend to focus on single events, and specific regions or seasons. For instance, Lledó et al. (2018) studied a single Wind Drought in the SouthWest North America (SWNA) region that happened in January, February, and

March of 2015. During this event, the seasonal-mean wind speed, averaged over SWNA, dropped up to 2.5 standard deviations below the 1979–2014 mean, based on reanalysis datasets. Using empirical orthogonal function (EOF) analysis and linear correlations, they identified relationships between monthly SST fields and wind patterns. They attributed these anomalies to elevated SSTs in the western tropical Pacific Ocean, which were linked to a strongly positive phase of the North Pacific Mode, playing a critical role in establishing and sustaining the observed wind anomalies. They also conducted a series of uncoupled simulations using the atmospheric component of the EC-Earth ESM, with sea ice and SST prescribed from ERA-Interim reanalysis. These retrospective predictions were used to confirm the link between reduced wind speeds in SWNA and anomalous Pacific SST conditions during the winter of 2015. While such studies provide valuable insights, they are often constrained by small sample sizes, region-specific analyses, and the use of a single atmospheric model forced with specified SST, limiting their ability to generalize conclusions. Moreover, many previous studies lack the comparative perspective provided by large ensembles and multiple climate models, which are essential for studying extreme events and evaluating the robustness of wind-SST relationships between different ESMs, due to the variability in parameterizations among climate models.

To address these gaps, this study utilizes large ensembles of historical simulations from three climate models— Canadian Earth System Model 2 (CanESM2), Canadian Regional Climate Model 4 (CanRCM4), and Community Earth System Model version 2 (CESM2). Each model ensemble comprises 50 statistically equivalent realizations, where differences between members arise solely from internal variability due to distinct initial conditions. By combining a total of 150 realizations, this research investigates the probabilistic relationship between Pacific SST patterns and the occurrence of extreme wind events in North America. The study focuses on the period 1950–2000 to disentangle internal climate variability from forced variability. This period minimizes the influence of anthropogenic forcing, ensuring that the observed variability is primarily attributable to internal climate processes.

The approach begins with the identification of wind extreme events, defined as anomalies exceeding ± 2.3 standard deviations from the seasonal mean wind speed. These thresholds, based on the framework of Lledó et al. (2018), are used to classify Wind Drought (WD) and Wind Flood (WF) events. SST anomalies during these events are then analyzed to identify characteristic patterns associated with each extreme. In this study, the term predictive skill refers specifically to the magnitude of

the predictability values associated with these SST patterns. It does not represent formal forecast skill metrics based on model accuracy, but rather reflects the strength of the statistical relationship between SST anomalies and the occurrence of WD and WF events. To assess the statistical significance of these relationships, Monte Carlo simulation approach is applied. The analysis spans six North American regions, divided into northern and southern zones, and covers all four seasons. Results indicate that extratropical SSTs predominantly drive WF events during winter, while SST anomalies in southern regions influence WD events across all seasons.

The structure of the thesis is as follows:

- Chapter 2 outlines the data and methodologies for identifying wind extremes, analyzing wind-SST relationships, and assessing predictability.
- Chapter 3 presents the key findings, focusing on the frequency, patterns, and predictability of these events across models, regions, and seasons.
- Chapter 4 discusses the implications of these findings and highlights future research directions.

Chapter 2

Data and Methodology

2.1 Data

This study utilizes large ensembles of historical simulations (1950–2000) from three climate models:

1. Canadian Earth System Model 2 (CanESM2): Developed by the Canadian Centre for Climate Modelling and Analysis (CCCma), CanESM2 integrates the physical atmosphere-ocean model (CanCM4), the terrestrial carbon model (CTEM), and the ocean carbon model (CMOC), with a horizontal resolution of 2.8125° (von Salzen et al., 2013; Arora et al., 2011). The archived model output for historical experiments provides monthly mean "Near-Surface Wind Speed" (sfcWind) and daily mean "surface temperature where land or ice" (tslsi) data. The variable tslsi contains temperature on land and ice, as well as SST for the ocean which has been used here. The dataset comprises 50 ensemble members, each representing a perturbed initial condition simulation from 1950 to 2020. These simulations, based on five Coupled Model Intercomparison Project Phase 5 (CMIP5) CanESM2 historical runs with ten perturbations each, is then conducted by CMIP5 historical forcings up to 2005, and extended to 2100 using RCP 8.5 forcings (Kushner et al., 2018; Kirchmeier-Young et al., 2017; Cannon et al., 2022).

2. Canadian Regional Climate Model 4 (CanRCM4): This model provides 1-hourly and 3-hourly "Near-Surface Wind Speed" (sfcWind) data for North America, with a horizontal grid resolution of 0.44° (approximately 50 km). The CanRCM4

dataset includes a 50-member ensemble from 1950 to 2100, driven by members of the CanESM2 ensemble. Simulations were conducted with CMIP5 historical forcings up to 2005 and RCP 8.5 forcings from 2006 to 2100, following the CMIP5 protocols (Scinocca et al., 2016).

3. Community Earth System Model version 2 Large Ensemble (CESM2 LENS): Developed by the National Center for Atmospheric Research (NCAR) in collaboration with the IBS Center for Climate Physics (Rodgers et al., 2021). CESM2 is a coupled climate model simulating the Earth's atmosphere, ocean, land, river runoff, land ice, and sea ice (Danabasoglu et al., 2020). The CESM2 LENS dataset consists of 100 members at a 1° spatial resolution, spanning 1850 to 2100 under CMIP6 historical and SSP370 future radiative forcing scenarios. 50 members have been forced with biomass burning (BMB) fluxes from the CMIP6 protocols (Rodgers et al., 2021). This study utilizes fifty CMIP6 BMB members of model output archived as monthly averages for "horizontal total wind speed at the surface" (WSPDSRFAV) and "sea surface temperature" (SST).

2.2 Methodology

To identify wind extreme events during the reference period, standardized anomalies of seasonal regional mean wind speed are computed, referred to hereafter as the "Wind index":

$$\tilde{S}_{\mathrm{y,r}}^{\mathrm{season}} = \frac{\overline{[S_{\mathrm{y,s,r}}]}^{\mathrm{season}} - \overline{\overline{[S_{\mathrm{y,s,r}}]}^{\mathrm{season}}}^{\mathrm{year}}}{\sigma\left(\overline{[S_{\mathrm{y,s,r}}]}^{\mathrm{season}}\right)} \tag{2.1}$$

where [ ] denotes the regional average, the overbar represents the time average, and σ indicates the standard deviation across years. The term $\overline{\overline{[S_{\mathrm{y,s,r}}]}^{\mathrm{season}}}^{\mathrm{year}}$ represents both the seasonal and long-term averages of regional mean wind speed. All notation used in the equations is summarized in Table 2.1.

A standardized anomaly is a statistical measure that quantifies how much a particular data point deviates from the long-term average, relative to the typical variability of the dataset. It is calculated by dividing the anomaly (the difference between the data point and the average) by the standard deviation. This standardization expresses the anomaly in units of typical fluctuations, facilitating easier comparison across different datasets or time periods.

Notation	Meaning
S	Surface Wind Speed
T	Sea Surface Temperature
PC	Pattern Correlation
P.I	SST Pattern Index
WD	Wind Drought
WF	Wind Flood
N(WD)	Number of Wind Drought events
N(WF)	Number of Wind Flood events
σ	Standard Deviation based on years
Σ	Standard Deviation based on years and realizations
$\tilde{X}$	Standardized Anomaly of variable X
$\overline{X}$	Temporal Mean of variable X
[X]	Spatial Mean of variable X
$\langle X \rangle_{\mathrm{WD}}$	Average of variable X over a set of Wind Drought events
$\langle X \rangle_{\mathrm{WF}}$	Same as Wind Drought but for Wind Flood
$\mathrm{X_{y,s,r}}$	Variable X depends on y (year), s (space), r (realization)
$\mathrm{X^{season}}$	Variable X over a season which can be "JFM", "AMJ", "JAS", "OND"

Table 2.1: Meaning of notation used in equations and text

After extracting the wind index, Wind Drought (WD) and Wind Flood (WF) events are defined based on specific thresholds of this index. Choosing the right threshold involves balancing the extremeness of the events with a sufficiently large number of events to increase statistical robustness. While higher thresholds may isolate more pronounced signals of SST influence on wind speed, they result in fewer events, which may reduce representativeness of the events. Lledó et al. (2018) noted that the winter WD event of 2015 fell more than two standard deviations (-2.5) below the 1979–2014 mean. In this study, I use a threshold of -2.3 standard deviations. This selection captures events nearly as extreme as those identified by Lledó et al. (2018), but with a sufficient frequency to allow for a statistically more meaningful sample size. Thus, WD events are defined as those when the wind index drops below -2.3 standard deviations.

In this study, we also establish a positive threshold to define WF events. To maintain symmetry in the analysis, WF events are similarly defined as those where the wind index exceeds +2.3 standard deviations above the mean.

After identifying wind extreme events across ensemble members, the average of wind anomaly patterns over the set of WD/WF events are calculated as represen-

tative WD/WF events, denoted as $\left\langle \tilde{S}_{\mathrm{s}}^{\mathrm{season}} \right\rangle_{\mathrm{WD}}$ and $\left\langle \tilde{S}_{\mathrm{s}}^{\mathrm{season}} \right\rangle_{\mathrm{WF}}$. The subscript "s" emphasizes that these quantities depend on space but not on year or realization.

Analysis of wind data has been conducted across six overlapping regions in North America (Figure 2.1). The regions span latitudes from 26° to 62° N, divided into southern and northern zones:

- Southern Regions (latitudes 26° to 44° N):
  - Southwest North America (SWNA): longitudes from 236° to 265° E
  - South-Central North America (SCNA): longitudes from 250.5° to 279.5° E
  - Southeast North America (SENA): longitudes from 265° to 294° E
- Northern Regions (latitudes 44° to 62° N):
  - Northwest North America (NWNA): longitudes from 224° to 263° E
  - North-Central North America (NCNA): longitudes from 244° to 283° E
  - Northeast North America (NENA): longitudes from 263° to 302° E

The seasonal analysis was performed for four seasons:

- Winter: January, February, March (JFM)
- Spring: April, May, June (AMJ)
- Summer: July, August, September (JAS)
- Fall: October, November, December (OND)

The standard deviation, σ, in equation (2.1) tends to be larger in northern regions than in southern regions, and is generally greater during the winter season compared to summer. Although a smaller σ in southern regions or during summer may amplify the relative magnitude of wind anomalies—making events appear more extreme—we identify extreme events based on standardized anomalies rather than absolute anomalies. This approach allows us to focus on events that are similarly unusual relative to the local climatology, even though actual differences in wind speed—which are crucial for power generation—may vary.

The historical analysis focuses on the period 1950–2000, during which forced climate change remained relatively small, allowing for a clearer assessment of internal

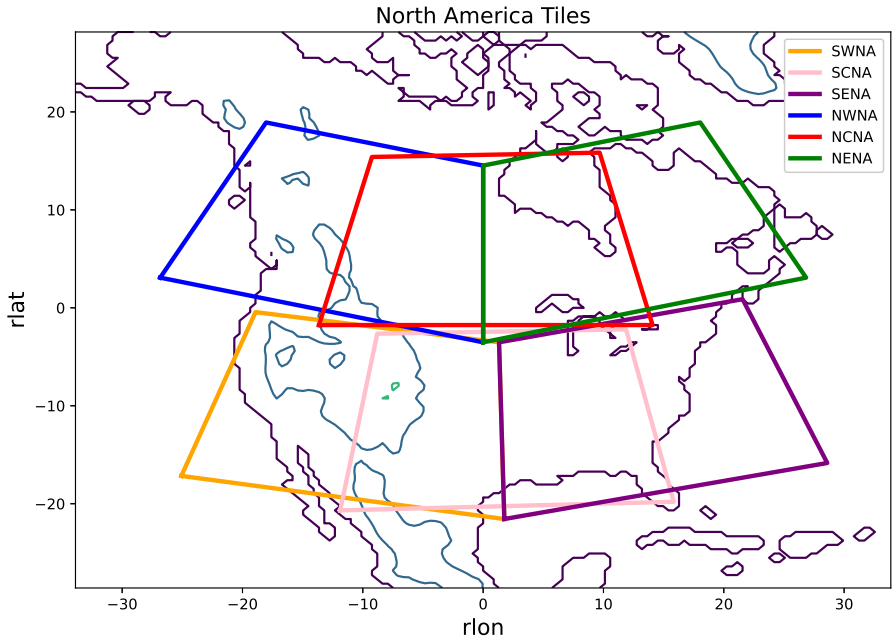

Figure 2.1: North American regions analyzed. The land mask is based on CanRCM4.

climate variability. To verify the limited influence of climate change during this period, the Niño 3.4 index—defined as the standardized anomaly of seasonal mean SST over the central tropical Pacific (5°N–5°S, 120°W–170°W)—is computed. Figure 2.2 displays the Niño 3.4 index time series from 1950 to 2050 for the CanESM2 large ensembles, along with ensemble mean and standard deviation curves.

Trend analysis of the Niño 3.4 index reveals that, from 1950 to 2000, the ensemble mean (representing the climate change signal) remains small relative to the ensemble standard deviation (representing internal climate variability), whereas after 2000 the ensemble mean begins to show an increasing trend. This confirms that the variability analyzed during the 1950–2000 period primarily reflects internal climate processes, with minimal influence from anthropogenic forcing.

To associate SST patterns with wind extreme events, the standardized anomalies of seasonal mean SST for each event are calculated:

$$\tilde{T}^{\text{season}}_{\text{y,s,r}} = \frac{\overline{T_{\text{y,s,r}}}^{\text{season}} - \overline{\overline{T_{\text{y,s,r}}}^{\text{season}}}^{\text{year}}}{\sigma\left(\overline{T_{\text{y,s,r}}}^{\text{season}}\right)} \tag{2.2}$$

The average SST patterns over the identified set of WD and WF events are then

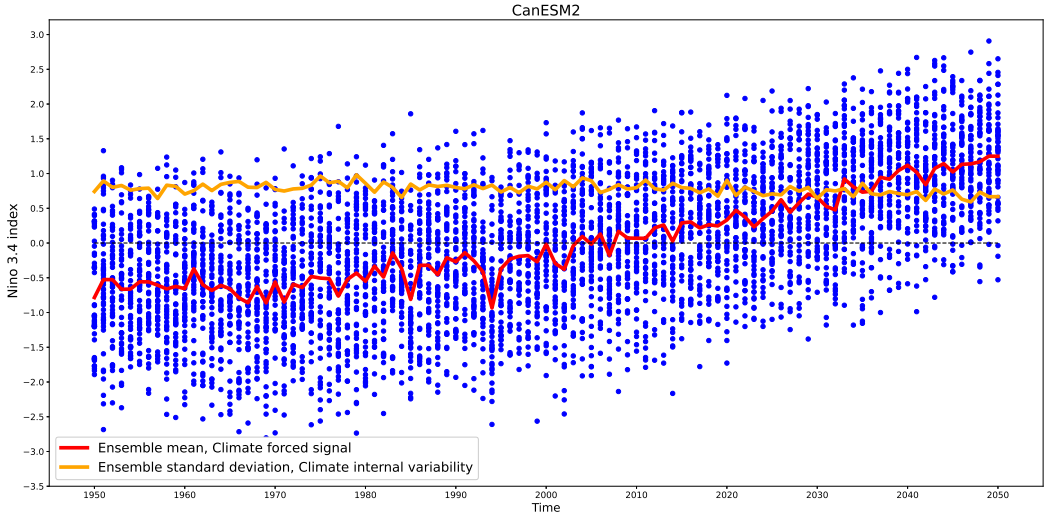

Figure 2.2: Timeseries of Nino 3.4 index, calculated for JFM in 1950-2050, using CanESM2 SST datasets.

computed, denoted as: $\left\langle \tilde{T}_{\mathrm{s}}^{\mathrm{season}} \right\rangle_{\mathrm{WD}}$ and $\left\langle \tilde{T}_{\mathrm{s}}^{\mathrm{season}} \right\rangle_{\mathrm{WF}}$, which serve as representative SST patterns for these events.

Although the representative SST patterns are associated with average conditions during wind extreme events, this does not imply that the occurrence of these patterns guarantees the occurrence of wind extremes. Therefore, it is essential to evaluate the predictive power of these SST patterns in relation to wind extremes.

To assess the probability of wind extreme events based on the representative WD/WF SST patterns, we develop an "WF/WD SST pattern index". This index is determined by calculating the pattern correlation between each realization-year SST pattern and $\left\langle \tilde{T}_{\mathrm{s}}^{\mathrm{season}} \right\rangle_{\mathrm{WD}}$ or $\left\langle \tilde{T}_{\mathrm{s}}^{\mathrm{season}} \right\rangle_{\mathrm{WF}}$:

$$\text{WD SST pattern index} = \mathrm{PC}\left(\left\langle \tilde{T}_{\mathrm{s}}^{\mathrm{season}} \right\rangle_{\mathrm{WD}}, \tilde{T}_{\mathrm{y,s,r}}^{\mathrm{season}}\right) = \frac{\sum_{\mathrm{s}}\left(\left\langle \tilde{T}_{\mathrm{s}}^{\mathrm{season}} \right\rangle_{\mathrm{WD}} \times \tilde{T}_{\mathrm{y,s,r}}^{\mathrm{season}}\right)}{\sqrt{\sum_{\mathrm{s}}\left(\left\langle \tilde{T}_{\mathrm{s}}^{\mathrm{season}} \right\rangle_{\mathrm{WD}}\right)^2 \times \sum_{\mathrm{s}}\left(\tilde{T}_{\mathrm{y,s,r}}^{\mathrm{season}}\right)^2}} \tag{2.3}$$

$$\text{WF SST pattern index} = \mathrm{PC}\left(\left\langle \tilde{T}_{\mathrm{s}}^{\mathrm{season}} \right\rangle_{\mathrm{WF}}, \tilde{T}_{\mathrm{y,s,r}}^{\mathrm{season}}\right) = \frac{\sum_{\mathrm{s}}\left(\left\langle \tilde{T}_{\mathrm{s}}^{\mathrm{season}} \right\rangle_{\mathrm{WF}} \times \tilde{T}_{\mathrm{y,s,r}}^{\mathrm{season}}\right)}{\sqrt{\sum_{\mathrm{s}}\left(\left\langle \tilde{T}_{\mathrm{s}}^{\mathrm{season}} \right\rangle_{\mathrm{WF}}\right)^2 \times \sum_{\mathrm{s}}\left(\tilde{T}_{\mathrm{y,s,r}}^{\mathrm{season}}\right)^2}} \tag{2.4}$$

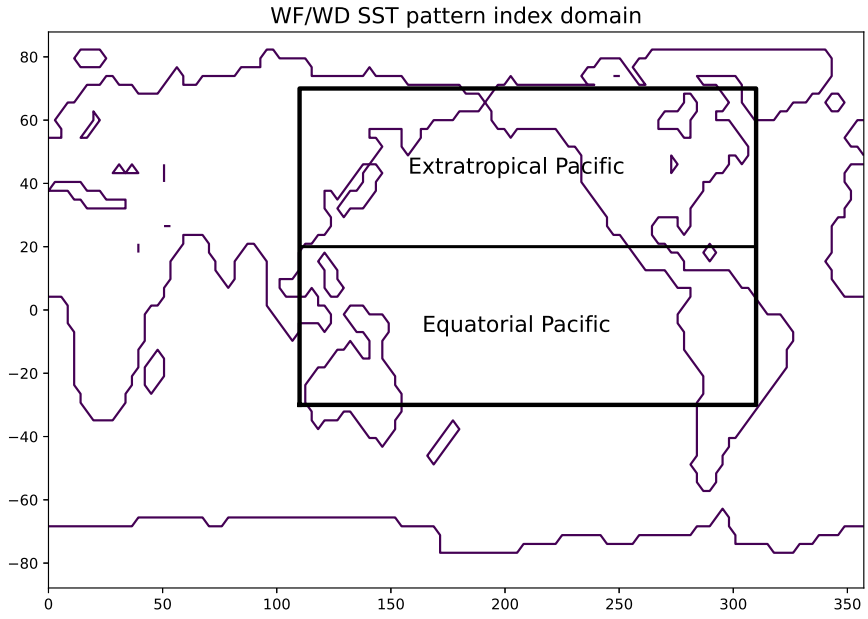

Figure 2.3: Domains used to compute the WD/WF SST pattern index. The full domain is outlined by a thick line, while the two subdomains (Equatorial and Extratropical Pacific) are separated by a thin line. The land mask is based on CanESM2.

The WF/WD SST pattern index has been computed for the Pacific Ocean, spanning latitudes from -30° to 70° and longitudes from 110° to 310° E (Figure 2.3). This domain is selected to enable a direct comparison with the results of Lledó et al. (2018). The index ranges from -1 to 1, where a value close to 1 indicates a strong resemblance to the wind extreme ensemble mean SST pattern, a value close to -1 indicates a mirror image, and a value around 0 shows no correlation.

The conditional probability of extreme events given that WF/WD SST pattern index exceeds a specified value is then calculated. The index, which ranges from -1 to +1, is divided into 200 equal intervals, each with a width of 0.01. For each of these intervals, the probability of an extreme event is determined by calculating the ratio of the number of extreme events to the total number of events where the SST pattern index exceeds a specified threshold:

$$\text{Predictability}_{\text{WD}}(x) = P(\text{WD} \mid \text{P.I} > x) = \frac{N(\text{WD})}{N_{\text{total}}} \mid \text{P.I} > x \tag{2.5}$$

$$\text{Predictability}_{\text{WF}}(x) = P(\text{WF} \mid \text{P.I} > x) = \frac{N(\text{WF})}{N_{\text{total}}} \mid \text{P.I} > x \tag{2.6}$$

For instance, the distribution of WD SST pattern index values for all events, along with WD events from CanRCM4 over SWNA during JFM, are shown in Figure 2.4. When the threshold for the SST pattern index is set at 0.80, the probability of experiencing a WD event for larger index values is $\frac{2}{8} = 0.25$; where 2 represents the number of WD events with WD SST pattern index higher than 0.8, and 8 is the total number of events meeting this SST pattern index criterion.

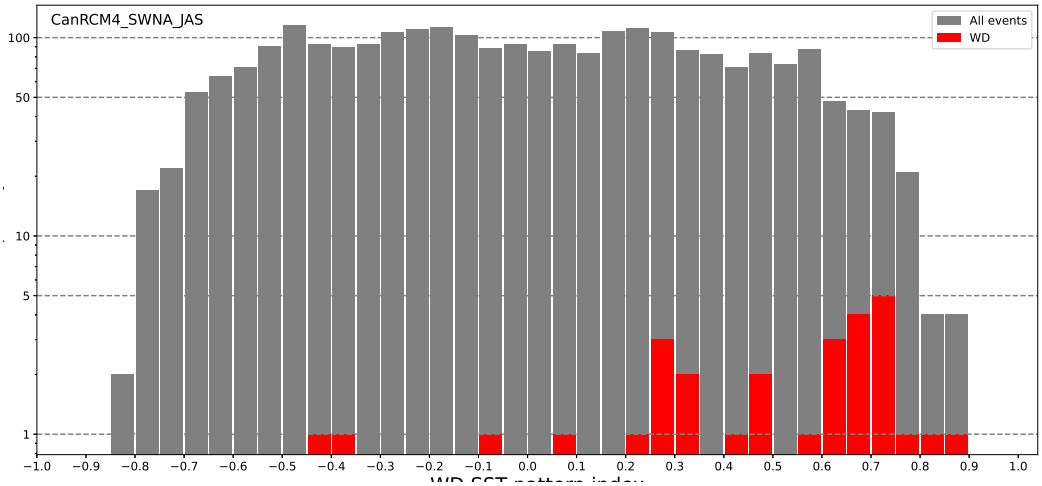

Figure 2.4: WD SST pattern index distribution of all events as well as WD events from CanRCM4 SWNA JAS.

To assess whether the North Pacific SST pattern or the Equatorial Pacific SST pattern plays a more determining role in driving wind extreme events in North America, the WF/WD SST pattern index was computed for both the Equatorial Pacific and Extratropical Pacific regions (Figure 2.3). The Pacific basin was divided into two zones: the Equatorial Pacific, spanning latitudes from -30° to 20°N and longitudes from 110° to 310°E, and the Extratropical Pacific, extending from 20° to 70°N across the same longitudes. SST pattern indices and corresponding probability curves were then calculated for each region and subsequently compared to evaluate their respective influences on wind extremes.

To evaluate the statistical significance of the probability curve for WD/WF events, a Monte Carlo simulation was employed. The objective was to compare the computed WD/WF probability curve with a set of randomly generated probability curves derived from synthetic datasets in which no true relation exists between events and the

Pattern Index, enabling a robust statistical comparison. The following steps were carried out:

1. Sampling of Events: N wind events are randomly selected across years and realizations, effectively randomizing the labeling of extreme events to create alternative scenarios. These synthetic events simulate WD or WF occurrences and their associated SST patterns arising purely by chance. The value of N corresponds to the number of extreme events identified for a given model, region, and season. This approach preserves the total number of extreme events while randomizing their occurrence across the synthetic datasets. This randomization procedure is repeated 100 times, each iteration generating a new synthetic sample of N events, enabling the construction of a reference distribution to assess statistical significance.

2. Generation of Probability Curves: For each of the 100 synthetic datasets, a probability curve was computed using the event corresponding SST pattern index, applying the same method to the true data. These curves represent the distribution of wind extreme predictability for different SST patterns expected by chance.

3. Comparison and Significance Testing: The true WD/WF probability curve, derived from the large ensemble analysis, was compared with the 100 synthetic curves to determine how the true curve deviates from what would be expected under random conditions, and to evaluate whether it is statistically typical or unusual. To assess significance, the 95th percentile of the synthetic curves was computed. If the true curve fell outside this threshold, it was deemed statistically significant, indicating that it is unlikely to have arisen by random chance.

4. Visualization: To aid in interpretation, the true probability curve was plotted alongside the 100 synthetic curves, with the 95th percentile curve highlighted (Figure 3.10). This visualization illustrates the extent to which the true predictability curve deviates from the distribution of random outcomes.

By performing this randomization and comparison, it is ensured that any patterns observed in the true WD/WF probability curve are statistically significant rather than arising from random fluctuations. This approach enables probabilistic predictions to be made regarding the likelihood of extreme events as the SST pattern index increases.

Chapter 3

Results

3.1 Frequency of Wind Extreme Events

Figure 3.1 displays the number of wind extreme events across all regions, seasons, and models, derived from large ensembles of 2,550 realization-years (50 members $\times$ 51 years). The number of WD events ranges from 9 to 36 depending on the specific model-region-season combination, while WF events range from 12 to 40 in similar conditions. Overall, models tend to simulate more WF events than WD events. However, the Canadian models (CanRCM4 and CanESM2) generally produce a greater number of WD events, whereas CESM tends to generate more WF events. Regionally, WF events are more frequent during the JFM season in northern areas, while WD events are more prevalent in southern regions during the JAS season.

Although the overall results are broadly consistent, notable variability exists in the number of extreme events simulated by different models. Given that extreme events lie at the tails of the wind distribution, slight differences in either model dynamics or among multiple realizations of the same model can lead to substantial sampling variability. For example, the global models CanESM2 and CESM exhibit notable discrepancies in the number of WD events during JFM in the NCNA and SENA regions, with one model identifying 31 events compared to just 13 by the other. Similarly, CanESM2 and CanRCM4 show pronounced differences in certain regions and seasons, such as the number of WD events in NWNA during JAS (32 vs. 22) and the number of WF events in SENA during JAS (17 vs. 28).

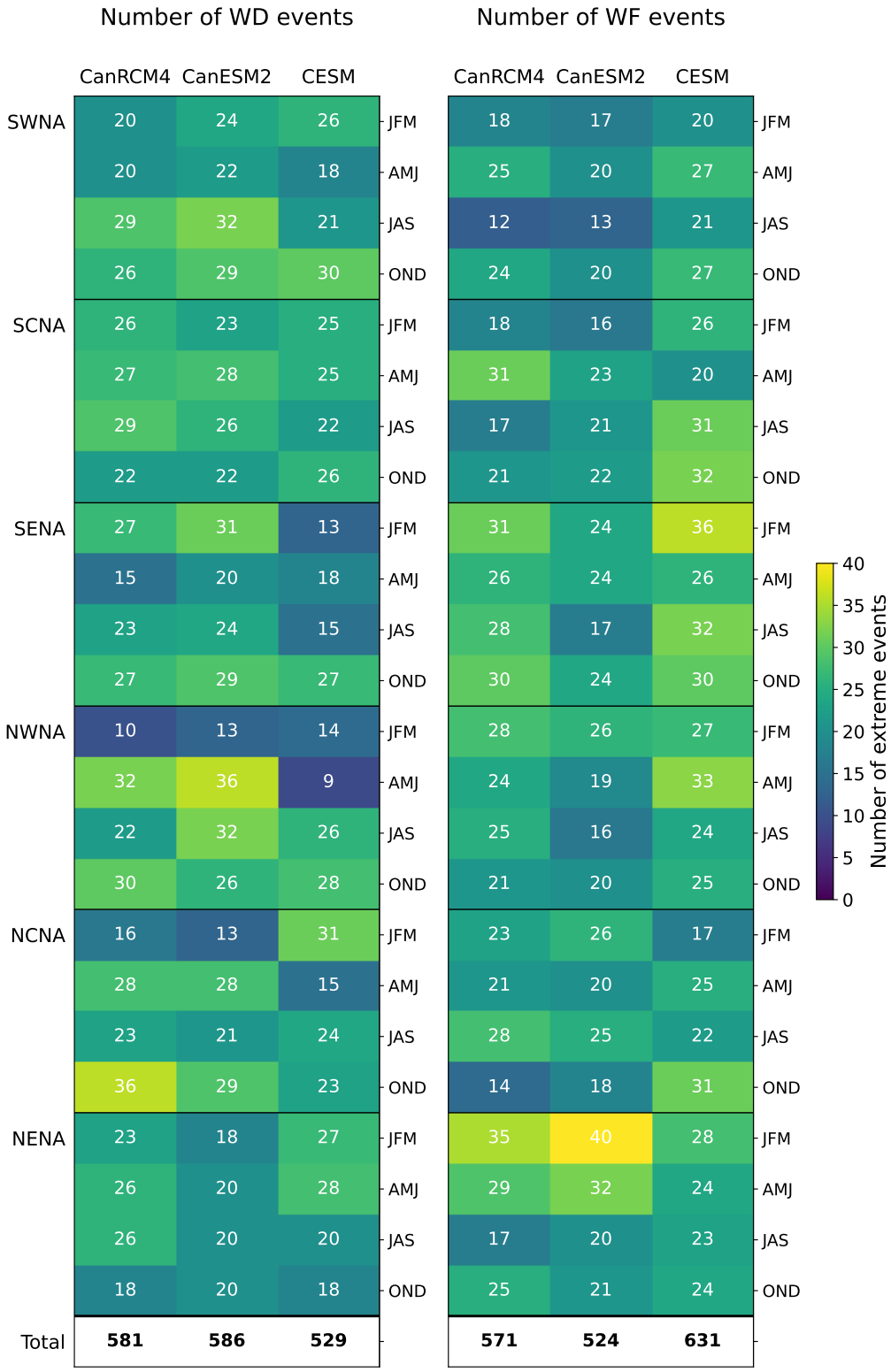

Figure 3.1: Number of Wind Drought (left panel) and Wind Flood (right panel) events across all regions, seasons, and models. The final row displays the column-wise sum, representing the total number of events simulated by each model.

While CanESM2 and CanRCM4 capture many common events, reflecting their shared large-scale meteorological structure, each model also identifies unique occurrences. These differences indicate that CanRCM4, by generating its own weather patterns, does not merely act as a higher-resolution version of CanESM2. Instead, it exhibits distinct behavior, likely influenced by its regional configuration and parameterization schemes. The absence of suitable observational data prevents determining which model provides a more accurate representation of reality. Nevertheless, the divergences between models results underscore the impact of structural differences and sampling variability on the simulation of extreme events.

3.2 Wind Anomaly Patterns

The average standardized wind anomalies associated with WD and WF events reveal consistent spatial patterns for specific regions and seasons, across models. This consistency is evident not only within the target regions but also in surrounding areas, indicating that these wind patterns are robust and spatially coherent. The observed agreement holds across all combinations of models, regions, and seasons, as well as for both extreme event types (3 models $\times$ 6 regions $\times$ 4 seasons $\times$ 2 event types), underscoring the reliability of the results across the ensemble framework.

Figure 3.2 illustrates the robustness of wind anomaly patterns by presenting the JFM mean of standardized surface wind speed anomalies for both WF and WD events in the NCNA region (outlined by a rectangular box) over the period 1950–2000. Results are shown in three rows: CanRCM4 in the first row, CanESM2 in the second, and CESM in the third. The standardized anomalies, displayed on a color scale ranging from -2.5 to +2.5, represent the intensity and spatial distribution of wind variations during WF and WD conditions. Positive wind anomalies (red) and negative wind anomalies (blue) reflect above- and below-normal wind speeds, respectively, with color intensity proportional to the magnitude of deviation.

As expected - given the definition of wind extremes - the WF events (left column) exhibit strong positive anomalies centered over the NCNA region, while WD events (right column) display strong negative anomalies in the same area. The anomaly patterns associated with WD and WF are nearly symmetric, differing primarily in sign. Wind anomalies exceed ± 2.5 standard deviations over many grid points within the region, indicating the extreme nature of these events, situated at the tail ends of the wind distribution. Similar wind anomaly maps for all other combinations of

models, regions, and seasons are provided in Appendix A.

Notably, areas surrounding the NCNA box exhibit alternating positive and negative anomalies, indicative of the influence of larger-scale atmospheric circulation features. In fact, across most regions, WD and WF events tend to extend beyond the boundaries of the target region, often impacting multiple areas simultaneously. However, an exception is observed in the SENA region as shown in Figure 3.3 right panel. In SENA, wind extreme events are more localized, with the sign of wind anomalies generally opposite to much of the rest of the continent, particularly for WF.

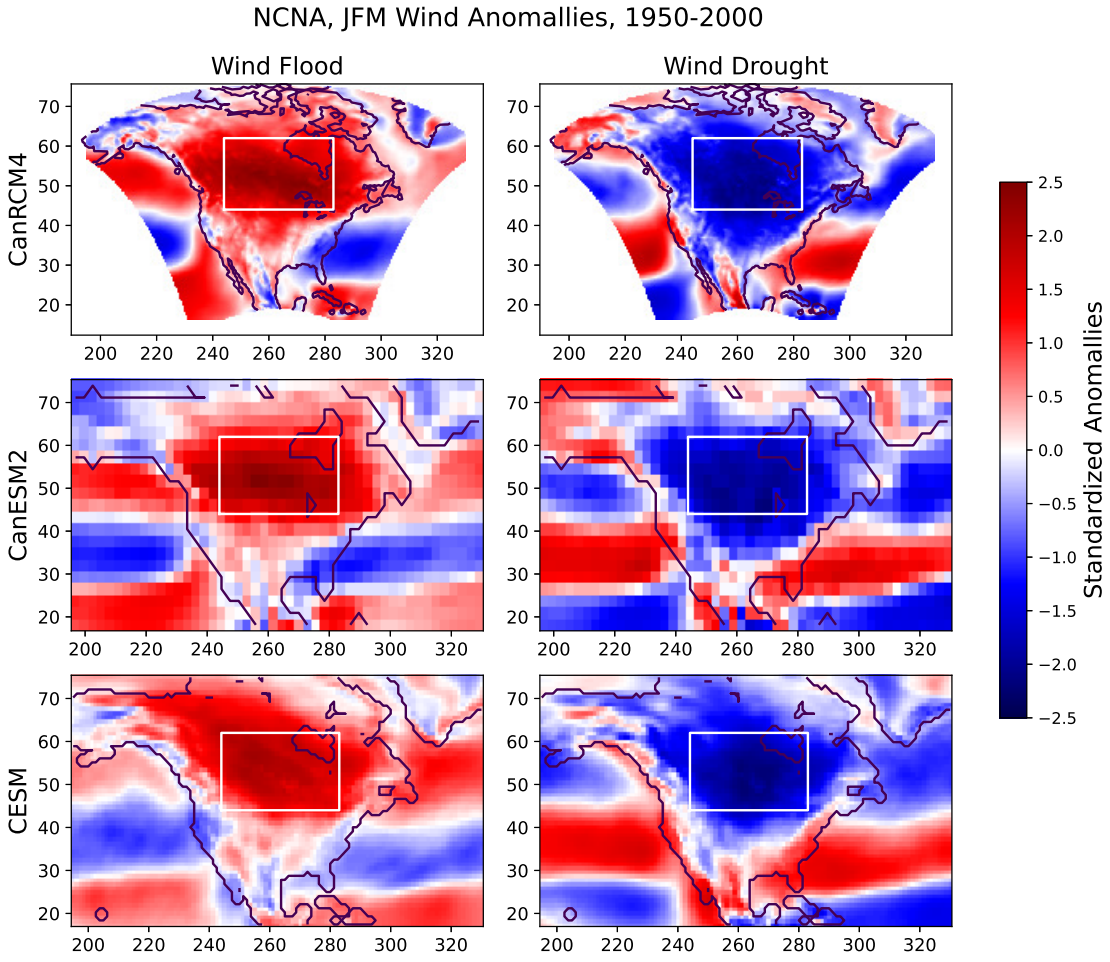

Figure 3.2: JFM mean of standardized anomaly of surface wind speed in NCNA, for WF events (left column), and WD events (right column), in NCNA in 1950-2000. The first row shows results from CanRCM4, the second from CanESM2, and the third from CESM.

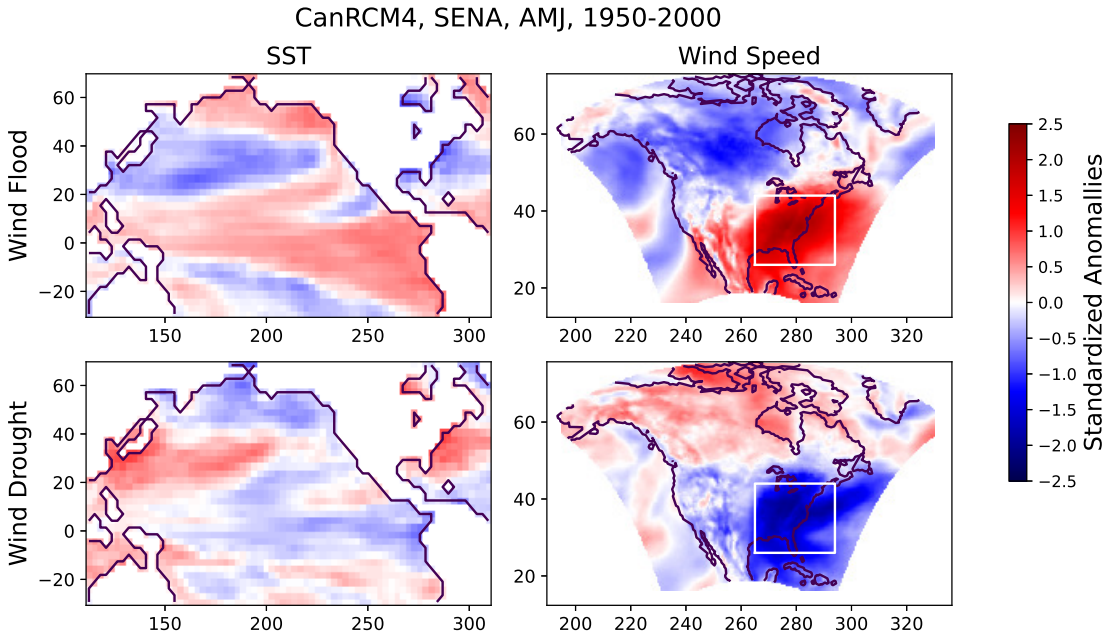

Figure 3.3: AMJ mean of standardized anomaly of sea surface temperature (left column), and surface wind speed (right column) in SENA in 1950-2000, for WF (first row) and WD (second row) from CanRCM4.

3.3 Wind-SST Relationships

As an initial step in analyzing the relationship between wind extremes and SST, the robustness of the wind-SST relationship identified by Lledó et al. (2018) is evaluated using a large-ensemble approach. They observed a substantial Wind Drought event in the SWNA region during January, February, and March of 2015. During this event, the seasonal wind standardized anomaly, averaged over SWNA, dropped up to -2.5 standard deviations below the 1979–2014 mean, based on a reanalysis dataset. Using empirical orthogonal function (EOF) analysis and linear correlations, they identified relationships between monthly SST fields and wind patterns. They attributed wind anomalies to elevated sea surface temperatures in the western tropical Pacific Ocean, which were linked to a strongly positive phase of the North Pacific Mode, playing a critical role in establishing and sustaining the observed wind anomalies.

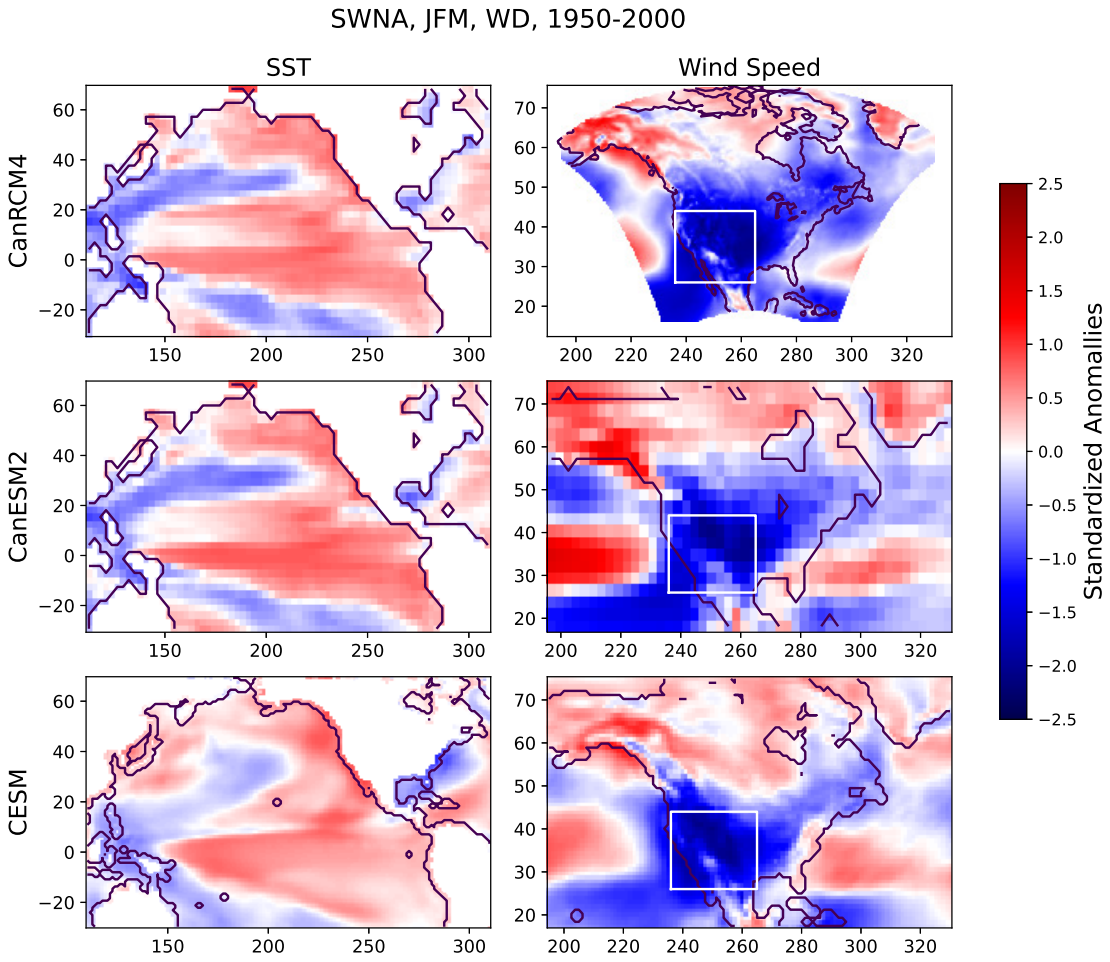

Figure 3.4: JFM mean of standardized anomaly of sea surface temperature (left column), and surface wind speed (right column), in SWNA in 1950-2000 for WD; first row shows results from CanRCM4, second CanESM2, and third CESM.

Figure 3.4 presents the seasonal WD anomaly patterns of wind and SST for SWNA during JFM, derived from the large ensemble analysis. The first row presents composite maps of 20 WD events from the CanRCM4 large ensemble, the second row shows composite maps of 24 WD events from the CanESM2 large ensemble, and the third row displays composite maps of 26 WD events from the CESM large ensemble. All SST anomaly maps show a band of warmer SSTs along the equatorial region, extending northward along the coast of North America, accompanied by alternating bands of cool and warm SST anomalies in the central-Western Pacific at higher latitudes (north of 30°N). These composite patterns, resulting from averaging over all

WD wind speed patterns and WD SST patterns, closely align with those reported by Lledó et al. (2018) from EOF analysis and linear correlations for January, February, March of 2015 (Figure 2 of Lledó et al. (2018)), confirming the relationship between SST pattern and low winds in SWNA.

To enable a direct comparison with Lledó et al. (2018), the composite maps using the same time period (1979–2014) and months (January, February, and March) were produced. However, due to their similarity to the seasonal results, the monthly composites are not shown here. The consistency between the seasonal and monthly analyses of SST anomalies indicates that the extremes persist over a longer temporal scale. Since the monthly analysis reveals no considerable variations among January, February, and March, the seasonal analysis is extended to other North American regions for conciseness.

Figures 3.5 and 3.6 present representative examples of WD/WF seasonal SST anomaly patterns for specific season-region combinations across models. These Figures, along with those in Appendix A, reveal that five out of six regions (SWNA, SCNA, NWNA, NCNA, and NENA) exhibit common features that are broadly consistent with one another. Based on the SST patterns in these regions, we define a characteristic SST pattern for WD events as follows: a warm SST anomaly in North Pacific, particularly over the Gulf of Alaska, often extending to subtropical and tropical Pacific regions. This is accompanied by a cold anomaly band stretching from Asia to the eastern Pacific around 40°N. Conversely, the characteristic SST pattern for WF events features a cold anomaly in the Gulf of Alaska, extending southward into the subtropical and tropical Pacific, alongside a warm anomaly band spanning from Asia to the eastern Pacific. Notably, WF SST maps often exhibit a reverse pattern relative to WD SST pattern.

Comprehensive wind anomaly patterns across all models, regions, and seasons, along with their corresponding SST anomaly patterns, averaged over WD/WF events are provided in Appendix A. These patterns further highlight the common features of SST anomalies across different cases.

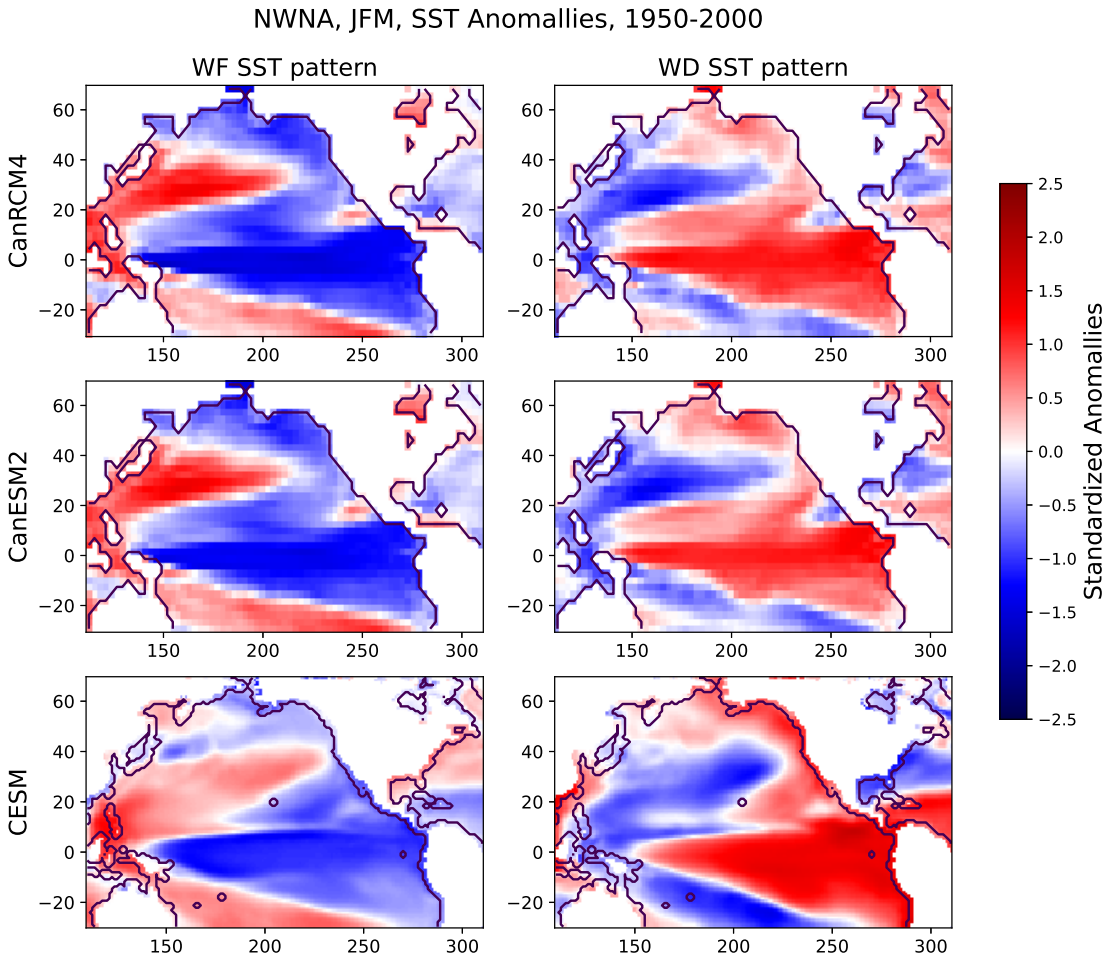

Figure 3.5: JFM mean of standardized anomaly of sea surface temperature for WF events (left column), and WD events (right column), in NWNA in 1950-2000, first row shows results from CanRCM4, second CanESM2, and third CESM.

Overall, the large-scale SST patterns associated with WD and WF events demonstrate notable robustness across the three models, five regions, and four seasons analyzed, capturing 87% of the cases. However, differences in finer details, such as the spatial distribution and magnitude of SST anomalies, are still apparent. Figure 3.5 showcases WF and WD SST anomaly patterns in the NWNA region for the JFM season as an example of a high level of consistency, where the spatial distribution and magnitude of anomalies are largely consistent across models, with only small differences, such as those off the coast of southwestern Mexico. Figure 3.6 presents JFM SST anomaly patterns in the NCNA region, illustrating a region-season combi-

nation with a lower level of consistency between models compared to JFM in NWNA (Figure 3.5). While the three models generally agree on the overall structure of representative WD and WF SST patterns in terms of spatial distribution and magnitudes of anomalies, CESM WF SST anomalies lack the strong magnitude signal seen in CanESM2 and CanRCM4.

Further fine differences between models and seasons are also evident in Figures 3.5 and 3.6, and also found in the Appendix A Figures. For example, a band of warm or cold SST anomalies in the subtropical North Pacific, centered around 20°N, frequently appears in CanESM2 and CanRCM4 but is absent in CESM. Additionally, the magnitudes of SST anomalies are generally stronger during the JFM season and weaker in JAS. Moreover, OND WD patterns in SWNA and SCNA (Figures A.4 and A.8), do not align perfectly with the representative WD SST patterns identified in this study. In these regions, the spatial distribution of WD SST anomalies slightly differ from the characteristic patterns observed elsewhere.

Figure 3.3 shows examples where the identified wind-SST relationship appears to break down. The sixth region, SENA, exhibits considerable variability in the spatial distribution and magnitude of SST anomalies, with nine out of twelve WF SST maps and six out of twelve WD SST maps deviating from the characteristic patterns found elsewhere. Interestingly, however, the sign of SST anomalies in SENA is generally opposite to that in much of the rest of the continent, especially for WF events, aligning with the previously discussed wind anomaly pattern in this region. More specifically, during AMJ and OND, both CanRCM4 and CanESM2 exhibit reversed WF and WD SST patterns in SENA.

As a result, the robustness of the wind-SST relationship must be assessed with the recognition that extremes in SENA often feature opposite-signed anomalies compared to the five other regions of the continent. Rather than indicating a breakdown of the relationship, this pattern suggests that the wind-SST connection remains intact but expresses itself differently across regions. The presence of consistent yet reversed anomalies implies a systematic response to large-scale climate variability, demonstrating that robustness is not solely defined by identical spatial patterns but by the persistence of a structured and predictable relationship even when expressed with opposite signs in different regions.

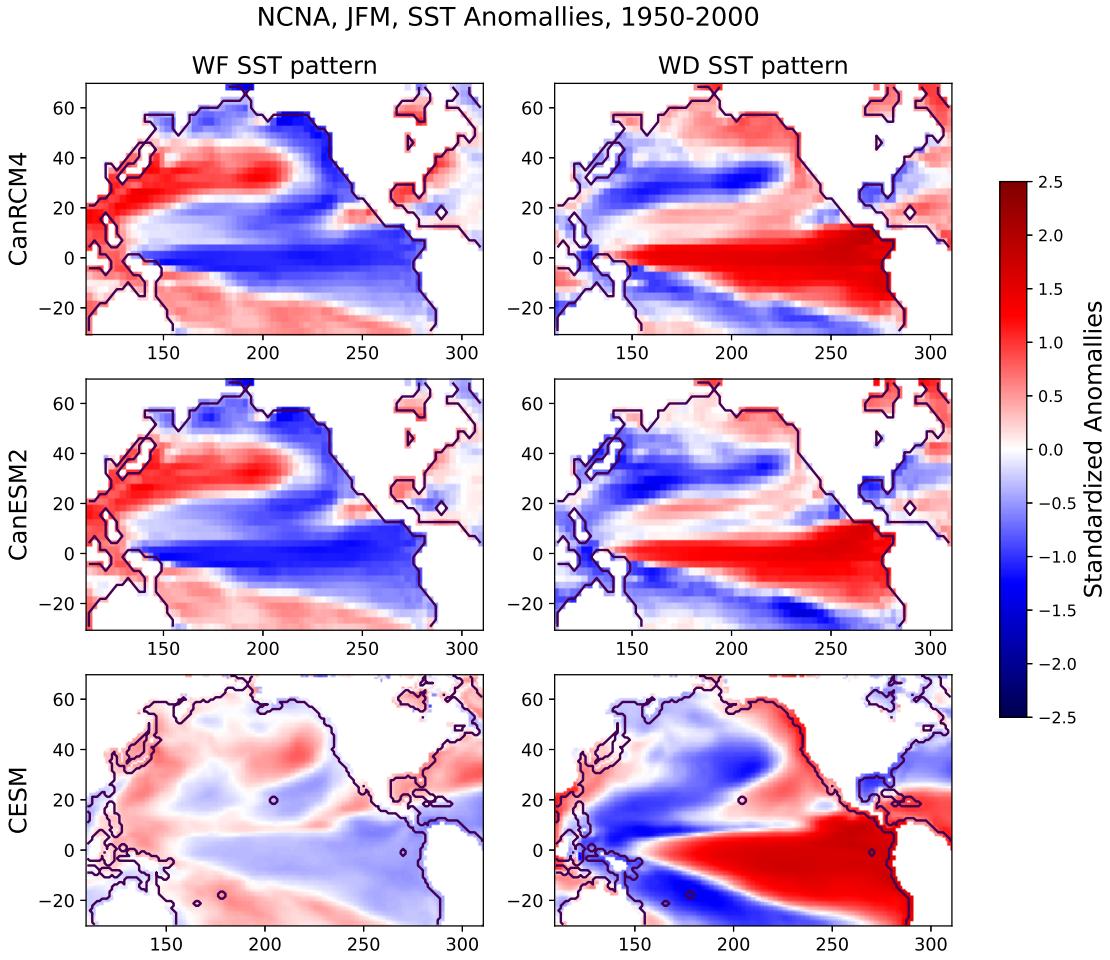

Figure 3.6: JFM mean of standardized anomaly of sea surface temperature for WF events (left column), and WD events (right column), in NCNA in 1950-2000, first row shows results from CanRCM4, second CanESM2, and third CESM.

These results largely support the idea that, with the exception of SENA, WD/WF events are consistently associated with the characteristic WD/WF SST patterns defined earlier. In contrast, in SENA, WD/WF events often tend to correspond with the opposite-signed SST patterns. Notably, the wind-SST relationship appears particularly robust in the northern regions of North America, as confirmed by model agreement across regions and seasons.

3.4 Predictability

Figures 3.7 and 3.8 present the predictability of WD and WF events across all models, regions, and seasons. The regions are arranged in rows, and seasons as columns. The three colored lines—yellow for CanRCM4, green for CanESM2, and red for CESM—depict the predictability skill of each model's WD/WF SST pattern for a given region and season. Although SENA exhibit opposite-signed SST patterns seen in other regions, it is included in this analysis because its SST pattern still demonstrates predictive skill.

In these Figures, predictability is plotted as a function of the SST Pattern Index, where higher values on the horizontal axis correspond to an SST pattern more closely resembling the characteristic SST pattern for the given model, region, and season. Values between -1 and 0 are omitted from the horizontal axis due to negligible predictability in this range, allowing the focus to remain on the 0 to 1 interval. Typically, values on the horizontal axis rarely exceed 0.9, as it is improbable for an event in the large ensemble to align perfectly with the characteristic SST pattern, which represents an average over extreme wind events.

The vertical axis ranges from 0 to 1, where 1 represents 100% predictability. The probability values at each point correspond to the ratio of the number of extreme events to the total number of events for which the SST pattern index exceeds a specified threshold. It is important to mention that both the numerator and denominator of this ratio generally decrease as the pattern index increases. For clarity, the predictability curves are shown only up to the point where the sample predictability falls to zero; sections that drop to zero are omitted, as they result from insufficient sample sizes rather than meaningful signals.

To indicate statistical significance, sections of the curves in Figures 3.7 and 3.8 that pass the hypothesis test are shown in color, while those that fail are marked in black. This distinction illustrates both the strengths and limitations of SST-based predictability for extreme wind events.

Across all regions and seasons, the predictability of extreme wind events generally rises as the SST Pattern Index increases, with a maximum value toward larger values of the SST Pattern Index. This indicates that WD/WF events are more likely to occur when the SST pattern closely resembles the characteristic WD/WF SST pattern for a given model, region, and season. This finding reinforces the link between SST anomalies and the occurrence of WD/WF events.

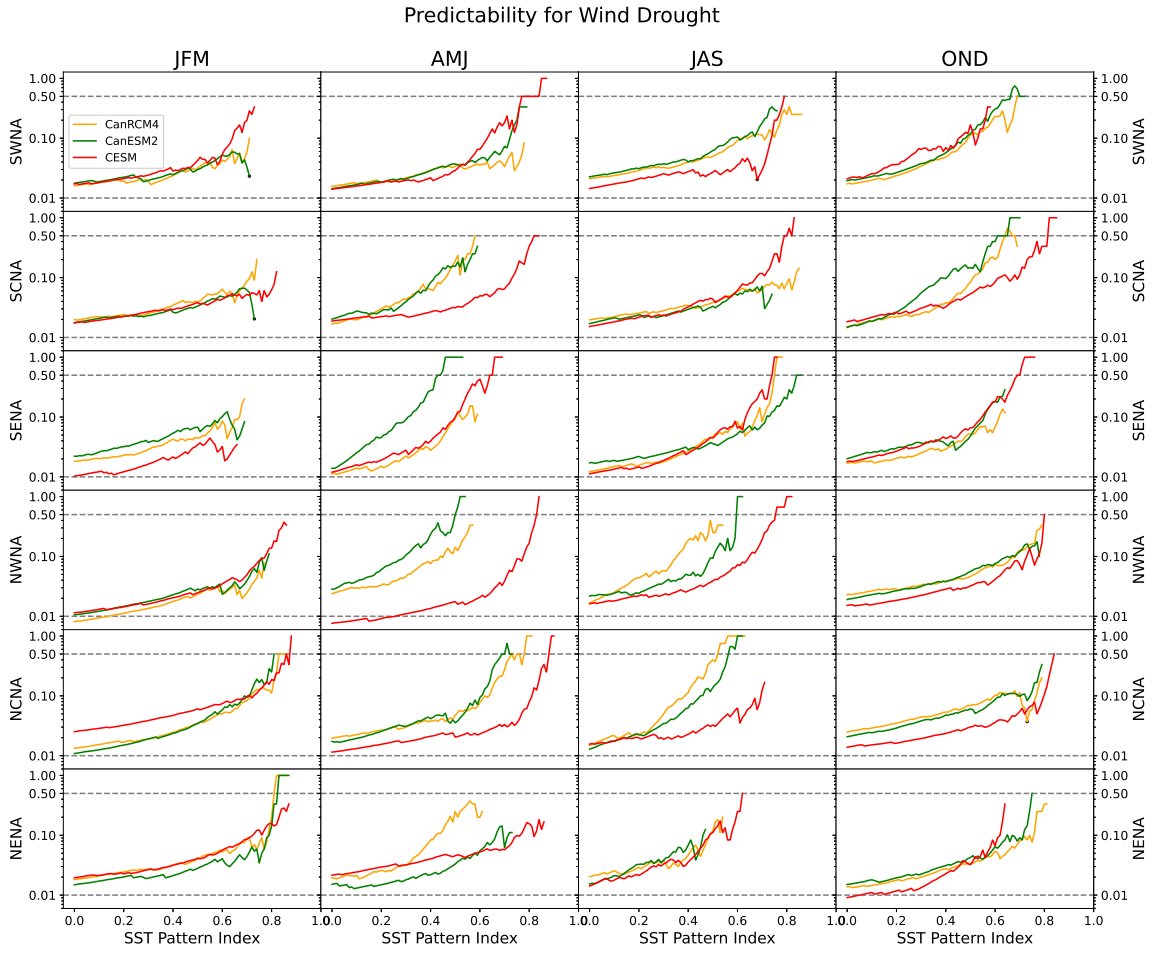

Figure 3.7: Conditional probability of Wind Drought events as a function of the SST Pattern Index for North American regions (rows) and seasons (columns) during 1950–2000. Orange, green, and red curves represent results from CanRCM4, CanESM2, and CESM, respectively. Statistical significance of the probability curves was assessed using a Monte Carlo simulation with 100 synthetic datasets; sections of the curves below the 95th percentile threshold of the synthetic distributions are shown in black. The vertical axis is on a logarithmic scale, and horizontal dashed lines indicate the thresholds (1% and 50%) used to classify predictability as "beyond random chance" and "beyond a coin flip".

Although SST patterns generally carry predictive information, the strength and robustness of this information varies. The robustness of the predictive signal is evaluated by comparing results across models, while its strength is determined by the magnitude of predictability. Certain regions and seasons, particularly northern re-

gions during JFM and OND, exhibit robust and strong predictability. However, in other regions and seasons, the amount of predictive information in SST patterns tends to be weaker and/or less consistent across models. For example, in SCNA and SWNA, predictability during OND and AMJ is generally strong for sufficiently large SST pattern index values, but models disagree on the threshold of SST pattern index at which extreme events become strongly predictable.

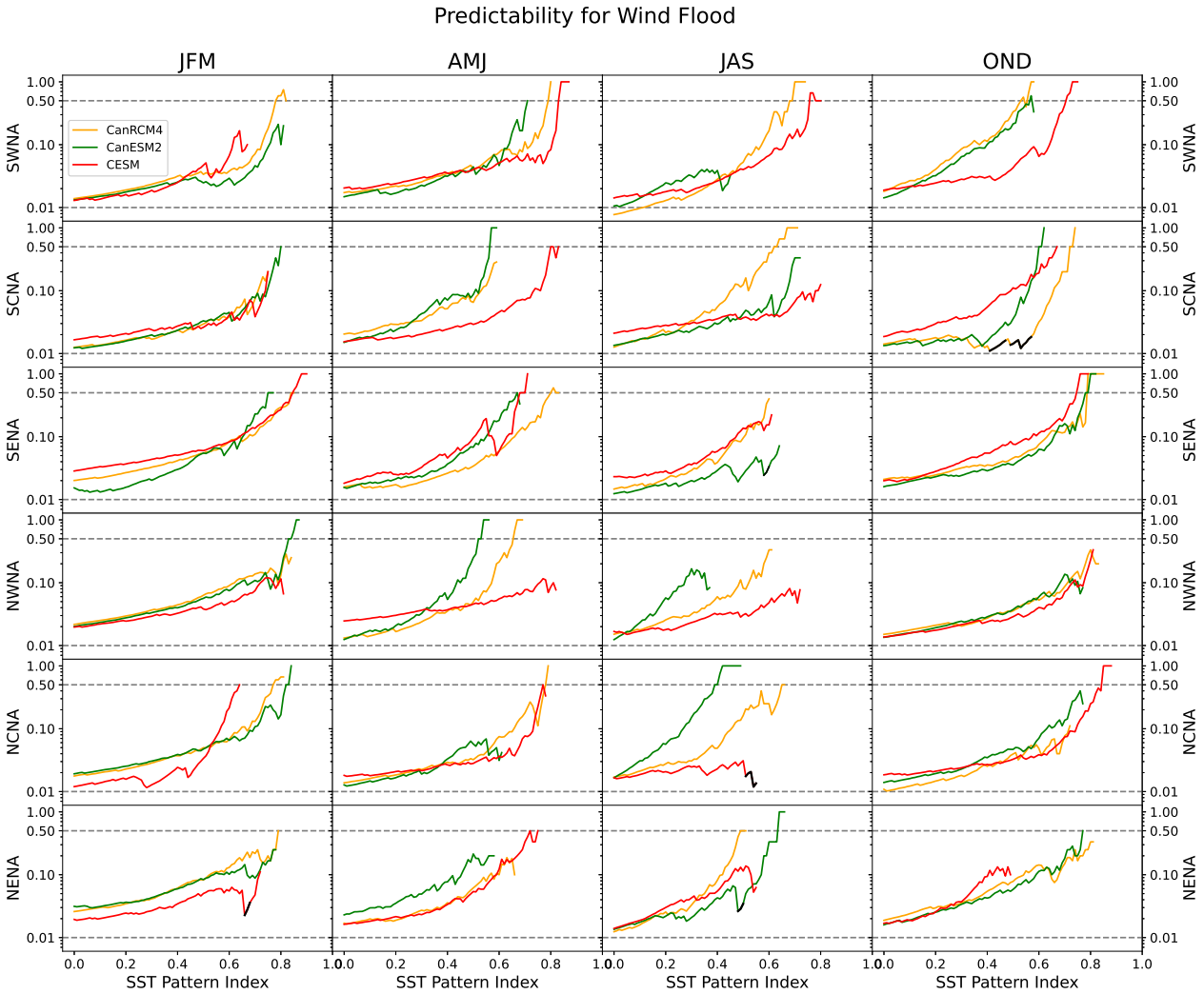

Figure 3.8: Same as Figure 3.7 but for Wind Flood.

This predictability measure is sensitive to sampling, as evidenced by different observations:

- Reducing the number of ensemble members in CanRCM4 analysis from 50 to 35 resulted in consistent wind/SST anomaly maps but altered the predictability

curves, highlighting the influence of sample size on predictability. Figure 3.9 presents the SST anomaly pattern derived from 35 CanRCM4 ensemble members, which remains consistent with the corresponding pattern in Figure 3.5 (right panel of the first row, based on 50 CanRCM4 ensemble members). The figure also compares the predictability curves obtained from these two datasets.

- Despite using the same SST dataset to assess predictability for CanESM2 and CanRCM4, differences in their predictability curves occasionally emerged, even though their extreme events' SST patterns appeared similar.

While the details of the predictability measures are sensitive to sampling, their overall robustness is confirmed by the significance test.

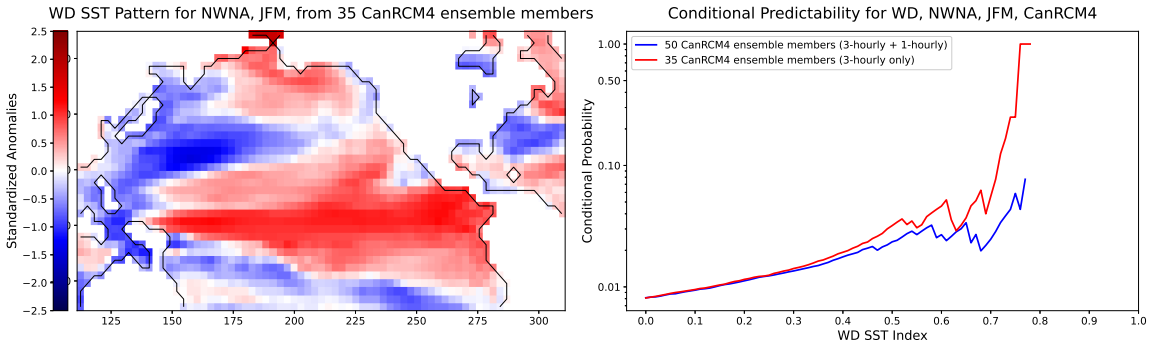

Figure 3.9: Results based on 35 three-hourly CanRCM4 realizations for NWNA during JFM (1950–2000). Left panel: JFM mean of standardized SST anomalies during WD events. Right panel: Conditional probability of WD events.

As mentioned earlier, in the case of SENA, WD and WF SST patterns are generally reversed compared to those in other regions, resembling the characteristic SST patterns of WF and WD, respectively. Despite this inversion, SST patterns in SENA show strong predictability skill, emphasizing the unique dynamics in this region. Notably, WF SST patterns demonstrate particularly high predictability in all seasons except JAS. This distinction indicates the value of considering regional variations in SST patterns when assessing the predictability of extreme wind events.

Figures B.1 to B.4 in the Appendix B illustrate the comparative predictive skill of North Pacific (20° to 70°N, 110° to 310°E) and Equatorial Pacific (-30° to 20°N, 110° to 310°E) SST for wind extreme events across North American regions. These Figures provide a visual representation of how SST variations in different Pacific

regions contribute to the predictability of wind extremes, offering insights into the geographical specificity of SST impacts on wind-related extremes. The results suggest that extratropical SSTs are generally more effective in predicting extreme events in all regions. In northern regions, the extratropical domain plays a key role in predicting WF events during the JFM season, while in southern regions, it exerts a more substantial influence on predicting WD events in the JFM, AMJ, and JAS seasons, compared to the equatorial domain. These results highlight that, despite the presence of robust SST anomalies in the tropical Pacific, the predictive skill for wind extremes is more closely tied to midlatitude processes, indicating that ENSO plays a secondary role in shaping wind extreme anomalies.

3.5 Statistical Significance

Figure 3.10 provides an illustrative example of the methodology for the null hypothesis test described in the previous section, demonstrating its application to a specific model, region, and season. This Figure presents the conditional predictability of WD events in the NCNA region during the OND season, on a logarithmic scale, based on the CanESM2 model. The red line represents the true conditional predictability derived from the large ensemble analysis, while the gray lines indicate predictability metrics obtained from 100 randomly generated samples. To assess statistical significance, the black line marks the 95th percentile of these random samples. Figure 3.10 is described in detail to explain the methodological framework used in previous Figures.

Figure 3.10 also illustrates how statistical significance is determined. The 95th percentile of random samples serves as a benchmark: if the true predictability curve (red line) exceeds the 95th percentile threshold (black line), the predictability is considered statistically significant at the 5% significance level. While individual sample curves (gray lines) may occasionally exceed the red curve at specific points, the overall pattern indicates that the 95th percentile line generally remains below the true predictability curve. This underscores the robustness and statistical significance of the predictive skill, which are unlikely to arise from sampling variability.

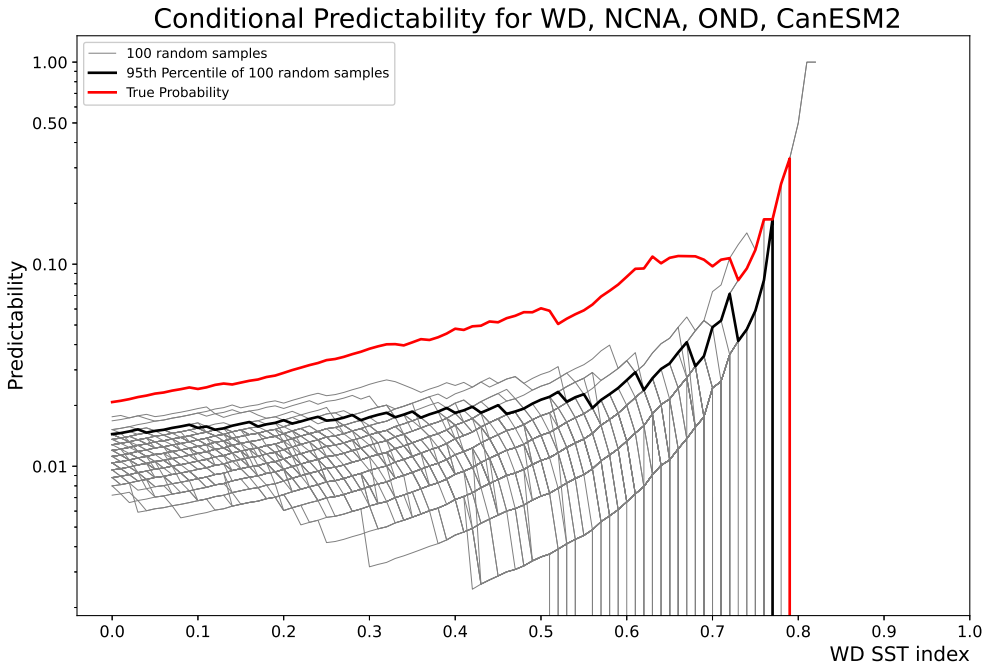

Figure 3.10: Conditional predictability of WD events for the NCNA region during OND based on the CanESM2 model. The gray lines indicate predictability metrics from 100 random samples, the black line represents the 95th percentile threshold, and the red line shows the true predictability based on large ensemble analysis. Vertical axis is scaled logarithmically.

The Monte Carlo simulations conducted for each climate model indicate that WD predictability curves are predominantly statistically significant across North American regions and seasons. Only four points of SST pattern index that failed to reject the null hypothesis of no relationship or predictive skill between SST pattern index and WD occurrence. These points are shown in black in Figure 3.7: CanRCM4 (NCNA during OND), CanESM2 (JFM for SWNA and SCNA), and CESM (JAS for SWNA). However, these exceptions are limited in number and do not undermine the overall robustness of the results. Therefore, the predictability curves, unlikely to be due to random chance, underscore the models' ability to predict WD events based on the SST Pattern Index.

Similarly, WF probability curves are generally statistically significant, though for five curves there are ranges of SST pattern index falling below the 95th percentile

threshold. These include WF predictability for CanRCM4 (SCNA during OND), CanESM2 (SENA and NENA during JAS), and CESM (NCNA during JAS and NENA during JFM) that are shown in black in Figure 3.8. Such instances of failure likely reflect either the limited predictive power of SST anomalies for WF events in these cases or the influence of sample size on robustness of the prediction. Notably, these less robust sections have probability values below 0.1, making the failure to reject the null hypothesis less important from the point of view of practical predictability. Therefore, the non-significant areas do not detract from the overall meaningfulness of the results, as curves exhibiting better predictive skill (above 0.1) remain statistically significant.

Despite isolated exceptions (mostly in WF predictability), the overall pattern of statistical significance supports the hypothesis that SST anomalies have robust skill in predicting extreme wind events. The findings indicate that, as the SST Pattern Index increases, the probability of WD and WF events rises significantly across most regions, with all models demonstrating some predictive skill in capturing these relationships.

3.6 Predictability Classes

To establish a benchmark for extreme event predictability, two thresholds are defined: "beyond random chance" for probabilities exceeding 0.01 and "beyond a coin flip" for probabilities exceeding 0.5. While the 50% threshold is somewhat arbitrary, it serves as a practical "even odds" benchmark. A probability curve exceeding 50% for sufficiently large values of the SST Pattern Index suggests that the likelihood of this unlikely extreme event happening is higher than that of a flipped coin. The threshold value of 0.01 corresponds to the integral of a probability density function (PDF) of a standardized Gaussian variable over $[2.3, \infty)$ or $(-\infty, -2.3]$ which gives the probability of the random variable taking a value greater than 2.3 or taking a value of less than -2.3.

$$\int_{2.3}^{\infty} \frac{1}{\sqrt{2\pi}} \exp\left(-\frac{x^2}{2}\right) dx = \int_{-\infty}^{-2.3} \frac{1}{\sqrt{2\pi}} \exp\left(-\frac{x^2}{2}\right) dx \approx 0.0107$$

It is important to note that we do not assume the probability distribution is Gaussian; rather, Gaussian exceedance probabilities are used as a convenient benchmark. Based on this, the integral yields approximately 0.0107, indicating that the total probability of being above 2.3 (equivalently total probability of being less than

-2.3) is about 1%. Thus, probabilities exceeding 0.01 are labeled as "beyond random chance". These two thresholds (1%, and 50%) are indicated in Figures 3.7 and 3.8.

The results for the range of SST Pattern Index values shown here, from 0 to 1, indicate that predictability consistently exceeds the 0.01 threshold, demonstrating that all cases exhibit predictability "better than chance". Furthermore, the analysis reveals that the "even odds" threshold is surpassed in almost half the cases of WD and WF events.

Figure 3.11 provides a summary of the predictability information presented in Figures 3.7 and 3.8, based on the 50% and 1% thresholds, across six geographic regions in North America. The shading within each quarter indicates the class of predictability skill of the full domain SST pattern for a specific model, region, season, and event: black denotes predictability above 50% (beyond a coin flip), grey denotes predictability above 1% (beyond random chance), and white denotes negligible predictability skill.

The regions are arranged on the Figure to correspond to their locations on the North American map. The bottom row includes SWNA (left), SCNA (middle), and SENA (right) while the top row includes NWNA, NCNA, and NENA (from left to right). Each region features two rows of three circles: the top row represents WD predictability, and the bottom row represents WF predictability. Each circle corresponds to a model—CanRCM4 (left), CanESM2 (center), and CESM (right)—and is divided into four quarters, with each quarter representing a season as indicated in the legend.

It is important to emphasize that this Figure highlights predictability based on the characteristic WD and WF SST patterns discussed earlier. For SENA, the predictability is based on that region specific SST pattern which is opposite signed compared to other regions. The fall WD events in southern regions are excluded from this analysis, as their characteristic SST patterns is not consistent among models and regions. Figure 3.11 provides a concise overview of spatial predictability for WD and WF events across regions, seasons, and models. Similar plots for extratropical versus equatorial domains are illustrated in Figures B.5 and B.6 in the Appendix B.

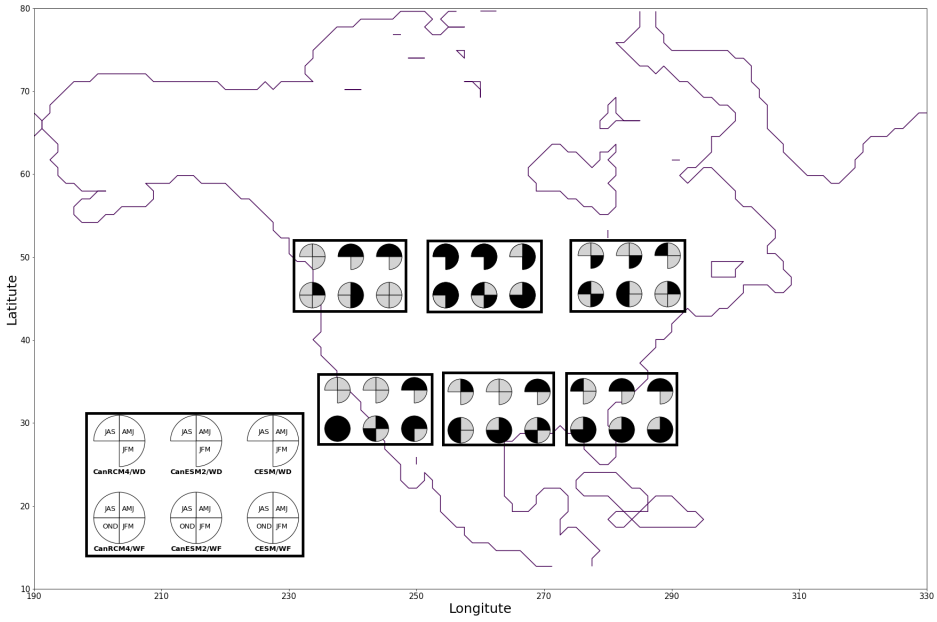

Figure 3.11: Predictability summary for WD and WF events across North American regions. Black, grey, and white colors show different classes of predictability: "beyond a coin flip", "beyond random chance", and "not predictable". SWNA and SCNA, and SENA are displayed in the bottom row, and NWNA, NCNA, and NENA in the top row. Each region displays predictability results for three climate models (CanRCM4, CanESM2, and CESM), with each model represented by a circle divided into seasonal quarters as shown in the legend.

The results presented in Figure 3.11 reveal no instances of white shading, emphasizing that SST patterns consistently exhibit at least "beyond random chance" predictability across all models, regions, and seasons. Examining the black shading, which represents instances classified as "beyond a coin flip", reveals that 46% of model/region/season pairs (25 out of 54) of WD SST patterns meet this criterion. Similarly, 57% of model/region/season pairs (41 out of 72) of WF SST patterns are classified as "beyond a coin flip", highlighting the generally higher predictability of WF events compared to WD events. Notably, CESM demonstrates stronger skill generally in predicting WD events, whereas the Canadian models (CanRCM4 and CanESM2) excel in predicting WF events.

For the remainder of this section, I will examine the seasonal and spatial distribution of strong predictability (i.e., predictability exceeding even odds, as indicated by black shading in Figure 3.11). The seasonal predictability of WD events varies considerably across regions. During AMJ, WD predictability reaches 55% of model/region pairs (10 out of 18) in North America, although predictability in NENA remains low across all three models. In JAS, predictability is also 55%, with substantial disagreements between models except for SENA. Predictability in JFM is lower, at 28% of model/region pairs (5 out of 18), with SWNA, SCNA, SENA, and NWNA showing limited predictability across all models. Overall, AMJ emerges as the most predictable season for WD events across regions.

WF events, by contrast, exhibit stronger and more consistent predictability. In AMJ, predictability reaches 72% of model/region pairs (13 out of 18) across North America, with all three models demonstrating strong skill in SWNA, and SENA. During OND, WF predictability found in 61% of model/region pairs (11 out of 18), with robust predictability of 100% among models in southern regions. In JFM, WF predictability found in 55% of model/region pairs (10 out of 18), with strong skill observed in NCNA and SENA across all models. In JAS, WF predictability declines to 39% of model/region pairs (7 out of 18), with Canadian models performing well in NCNA and NENA. Notably, AMJ consistently emerges as the season with the highest predictability for both WF and WD events.

The regional distribution of predictability reveals distinct patterns. WD events are most predictable in NCNA, with an 89% (8 out of 9) predictability rate, followed by SENA at 55% (5 out of 9), and NWNA at 44% (4 out of 9), NENA and SCNA at 33% (3 out of 9) each, and SWNA at 22% (2 out of 9). For WF events, the highest predictability is in SWNA and SENA at 75% (9 out of 12), followed by NCNA at 67% (8 out of 12), SCNA at 58% (7 out of 12), NENA at 42% (5 out of 12), and NWNA at 25% (3 out of 12). These findings underscore the overall robustness of strong WF predictability compared to WD predictability, with WF events showing stronger predictability in southern regions, while WD events are more predictable in northern regions. NCNA stands out as a region with high predictability for both WF and WD events, particularly in winter, where results are consistent across all models. This highlights the strong relationship between SST anomalies and extreme wind events in this region. Despite these regional and seasonal differences, the general findings remain robust even when the predictability threshold is lowered from 50% to 20%, emphasizing the reliability of the results.

Chapter 4

Discussion and Conclusion

This study investigates the large-scale variability of seasonal wind extreme events across North America, focusing on the role of SST patterns in modulating wind drought (WD) and wind flood (WF) events. Using large ensembles from three climate models—CanESM2, CanRCM4, and CESM2—wind extreme events are identified based on deviations in wind speed exceeding ±2.3 standard deviations from the seasonal mean. The analysis is conducted over six North American regions and four seasons, with a focus on the period 1950–2000 to minimize anthropogenic influences. A WF/WD SST pattern index is developed to characterize Pacific SST patterns, and wind-SST relationships are analyzed by averaging SST anomaly patterns over identified WF/WD events.

4.1 Key Findings on Wind Extreme Events

Analysis of the wind index time series reveals that WF events occur more frequently in northern regions during winter (JFM), likely due to the increased frequency and persistence of extreme synoptic-scale systems, which drive more occurrences exceeding the +2.3 standard deviation threshold. Conversely, WD events are more prevalent in southern regions during summer (JAS), suggesting a seasonal shift in atmospheric circulation patterns that favor prolonged low-wind conditions.

Composite wind and SST anomaly maps reveal generally opposite patterns for WF and WD events. In five of the six regions (SWNA, SCNA, NWNA, NCNA, and NENA), wind anomalies extend beyond regional boundaries, often influencing multiple regions simultaneously. Extending wind anomalies well beyond the defined

regions indicates a large-scale reorganization of atmospheric circulation. Although the composites are based on regional wind extremes, the presence of wind anomalies outside these regions suggests that these events are part of a broader circulation response. This is consistent with the findings of St. George and Wolfe (2009), who observed that negative wind anomalies in the Southern Canadian Prairies were part of widespread wind speed reductions across western Canada. Our results on seasonal extremes build upon their findings, which focused on more modest wind anomalies resulted from the six lowest-wind winters in a 54-year observational record, and extend the analysis to a broader set of regions across North America.

Similarly, in these five regions, composite SST patterns exhibit consistent, opposite characteristic SST patterns for WF and WD events: WD events are associated with a band of warm SST anomalies in the Gulf of Alaska, while WF events correspond to cold SST anomalies in the same region, occasionally extending into the subtropical and tropical Pacific. This is accompanied by a contrasting band of cold SST anomalies for WD and warm SST anomalies for WF, stretching from Asia to the eastern Pacific around 40°N. Comparing these characteristic SST patterns to the dominant modes of SST variability identified by Hartmann (2015) through EOF analysis of monthly mean Pacific SST anomalies, we find that the SST pattern associated with WD events resembles a combination of the positive phase of the PDO, warm ENSO conditions, and the positive phase of the NPM. Conversely, WF SST patterns exhibit the opposite phases of these variability patterns

We interpret that variations in Pacific SST patterns modulate ocean-atmosphere interactions by altering teleconnections, which in turn influence large-scale atmospheric circulation features, including storm tracks and jet stream patterns (St. George and Wolfe, 2009; L'Heureux and Thompson, 2006; Cai et al., 2021; Hu et al., 2023). These changes ultimately affect the strength and direction of remote surface winds, leading to regional variations in the occurrence of wind extreme events across North America.

The fact that systematic wind anomalies are present over the Pacific midlatitude during wind extremes in most regions reinforces the role of large-scale circulation features in shaping extreme wind events. This provides strong evidence that regional wind anomalies are not merely local, but rather responses to broader synoptic-scale atmospheric conditions. In this framework, changes in teleconnections drive shifts in large-scale atmospheric circulation, which in turn create the conditions necessary for regional wind extremes to occur.

The seasonal contrast between winter and summer wind extremes further underscores the coupling between surface wind speeds and atmospheric circulation. The higher frequency of WF events in northern regions during winter and WD events in southern regions during summer is likely linked to jet stream shifts and associated storm track variations, which are in turn influenced by seasonal changes in teleconnections. These results emphasize the crucial role of Pacific SST variability in modulating wind extremes, with distinct seasonal and regional responses shaped by the interplay of large-scale atmospheric patterns.

While most North American regions exhibit similar SST-wind relationships, SENA presents a distinct behavior, characterized by more localized wind anomalies and reversed SST patterns compared to other regions. Wind anomalies in SENA are often opposite in sign to those observed across most of North America, especially for WF events. Likewise, SST anomalies in this region display a reversed pattern compared to other regions. Given these distinct characteristics, the five interconnected regions are classified as one category sharing the characteristic SST pattern, while SENA is designated as a separate category exhibiting an opposite SST–wind relationship. Despite these differences, the opposite-signed SST patterns in SENA still demonstrate strong predictive skill, highlighting the unique climate dynamics governing wind extremes in this region.

Our multi-model analysis reveals that the climate models exhibit broadly similar patterns and predictive capabilities. In particular, CanRCM4, driven by CanESM2, closely replicates the behavior of its driving model, underscoring the consistency of large-scale dynamics. Nonetheless, notable differences emerge in both the magnitude and spatial distribution of anomaly patterns as well as in the predictive skill within the model. These variations likely stem from inherent differences in model physics, parameterizations, and sample sizes.

For instance, CESM demonstrates stronger skill in predicting WD events, while the Canadian models (CanRCM4 and CanESM2) perform better in forecasting WF events. Although the models generally agree on a qualitative level, the quantitative discrepancies in event identification—even among models sharing the same driving conditions—provide additional evidence in support of the SST-wind connection. Overall, there does not appear to be any systematic difference among the model results.

4.2 Comparison to Previous Studies

Our analysis of extreme wind events across five North American regions aligns with and extends previous research on wind variability and its connection to SST patterns. Lledó et al. (2018) identified a strong linkage between Pacific SST anomalies and a single severe wind drought in SWNA during early 2015 (JFM). They attributed the event to anomalously high SSTs off the western coast of North America and positive anomalies in the western tropical Pacific, which contributed to the establishment and persistence of the observed wind anomalies.

Similarly, St. George and Wolfe (2009) demonstrated that wind variability in the Canadian Prairies is strongly influenced by ENSO phases, primarily through shifts in the subtropical branch of the North Pacific jet stream. They concluded that low-wind years in the southern Canadian Prairies coincide with El Niño events. Their study region (101°W to 114°W, 49°N to 51°N) overlaps with the NCNA region analyzed in our study. While this study does not explicitly examine this specific wind-ENSO relationship, the findings support St. George and Wolfe (2009) broader conclusion that El Niño-type Pacific SST anomalies influence WD events in NCNA, reinforcing the role of large-scale climate patterns in shaping regional wind extremes.

Additionally, our analysis indicates that wind extreme events are more strongly associated with midlatitude SST anomalies than with equatorial anomalies. This suggests that ENSO is not the primary driver of wind extremes in most regions, consistent with the findings of Lledó et al. (2018) who concluded that the positive phase of the North Pacific Mode exerts a greater influence on observed WD events than ENSO.

The limited role of tropical Pacific SSTs in our findings contrasts with St. George and Wolfe (2009), who emphasized the association between low-wind winters and tropical SST anomalies. This discrepancy may stem from their analysis being based on only the six lowest-wind winters coincided with El Niño in the Southern Canadian Prairies, which are not as extreme as the events examined in our study. Furthermore, their findings rely on a relatively short observational record (1954–2006) to link low-wind winters in the region to the El Niño–Southern Oscillation, whereas our results, despite focusing on extreme events, are statistically more robust due to the use of a large ensemble. Thus, this contrast may arise either from our focus on more extreme events or from the increased statistical robustness afforded by the large ensemble approach.

By leveraging a large ensemble approach, our study builds on previous research by demonstrating that the wind-SST relationship is not confined to a single event but persists across multiple seasons and regions. Earlier studies, constrained by the limitations of single-realization observational datasets, primarily relied on statistical techniques such as EOF analysis and linear correlations to establish this relationship. However, these methods require a number of assumptions like linear regression between variables, whereas the actual connection between remote wind and SST variability is not straightforward. In contrast, our approach employs a composite analysis that does not impose a predefined relationship between wind and SST, offering a more transparent methodology. This enhances confidence in the robustness of the identified relationships by reducing uncertainties associated with single-realization datasets and avoiding potential biases from statistical assumptions. Furthermore, the use of a multi-model large ensemble strengthens the reliability of these findings, reinforcing the persistence and consistency of the wind-SST connection across different model frameworks.

4.3 Why SENA behaves differently

The Pacific-North American (PNA) pattern is a prominent atmospheric teleconnection focused on the Pacific-North American region that influences North American weather patterns through distinct pressure centers (Hu et al., 2023; Yuan et al., 2015; Tuller, 2004; Bitz and Battisti, 1999). PNA variability is closely linked to SST anomalies in the Pacific. Its positive phase is characterized by positive geopotential height anomalies (ridge) over Western North America and near Hawaii, accompanied by negative anomalies (troughs) over the North Pacific (near the Aleutian Islands) and the Southeastern United States.

Notably, this wavelike teleconnection structure often behaves differently in the SENA region compared to the rest of North America. As reviewed by Pryor et al. (2020), wind resources across North America exhibit region-specific responses to dominant climate modes such as PNA and ENSO, with North America East identified as a distinct region of variability. This helps explain why, in our results, SENA displays wind and SST anomalies of opposite sign compared to the rest of the continent, particularly in winter. The reversed SST pattern suggests a reversed teleconnection, which in turn leads to an opposite impact on remote wind anomalies.

This regional variability across North America is also evident in the results of

St. George and Wolfe (2009), who analyzed mean winter 500 mb geopotential height anomalies averaged over El Niño events. Their findings resemble a positive PNA pattern, which leads to contrasting atmospheric conditions between Western and Central North America and the Eastern United States. Specifically, the response of 500 mb geopotential height anomalies to Pacific SST patterns manifests as a trough over SENA, while a ridge dominates the rest of North America. This pattern is consistent with Lledó et al. (2018) (their Figure 2), who linked higher sea level pressures over the continent to stronger wind anomalies in SWNA.

In fact, the presence of a high-pressure ridge over most of North America can block synoptic-scale storms and divert the jet stream, altering wind directions toward the north and consequently leading to low wind conditions across much of the continent. In contrast, the trough over SENA allows storms to move into the region, creating distinct atmospheric conditions. This regional variation in atmospheric responses to SST patterns helps explain the unique behavior of SENA regarding wind extreme occurrences compared to the other five North American regions.

Thus, it is hypothesized that the characteristic WD SST pattern produces a ridge over the five North American regions and a trough over SENA, modifying atmospheric circulation in a manner that promotes WD events across most of North America while simultaneously increasing the likelihood of WF occurrences in SENA. Conversely, when the characteristic WF SST pattern emerges, an opposite atmospheric response is expected.

4.4 Seasonal Predictability of Wind Extreme Events

As wind energy becomes a critical component of sustainable power generation, understanding seasonal wind variability is essential for grid reliability. The SST-wind relationship identified in this study advances SST-based predictability of wind extreme events, emphasizing the importance of understanding large-scale climate patterns for improving seasonal forecasting and predicting extreme events driven by atmospheric teleconnections. This knowledge allows energy providers to anticipate and mitigate periods of low and high wind speed, which could otherwise disrupt power production.

Based on our analysis, the likelihood of wind extreme events increases when the SST field closely resembles the characteristic SST pattern. However, the influence of SST anomalies on WD and WF events varies depending on geographic and seasonal contexts, leading to spatial and temporal differences in predictability across North

American regions and seasons.

Seasonal variability in predictive skill highlights spring (AMJ) as the season with the highest predictability for both WF and WD events across North America. Regional differences are also evident, with NCNA emerging as a region with a robust strong SST signal and robust high predictability skill of this signal for both WD and WF events in all seasons except summer. In this region, WD events exhibit an 89% predictability rate, while WF events reach 67% predictability, underscoring the strong link between SST anomalies and extreme wind events. This robust SST-wind relationship aligns with the findings of St. George and Wolfe (2009), further emphasizing the key role of Pacific SST patterns in shaping wind variability in NCNA.

The predictive skill of SST anomalies is more strongly linked to midlatitude processes, as extratropical SST anomalies generally exhibit greater predictive power for wind extreme events across all North American regions compared to SST anomalies from the equatorial Pacific or the full domain. This may be attributed to the ability of midlatitude SST anomalies to generate stronger remote (teleconnection) responses in the atmosphere, whereas tropical SST anomalies primarily induce local responses (Thomson and Vallis, 2018a,b).

The predictive strength of extratropical SSTs is particularly valuable for WF events in northern regions during JFM, as WF events occur most frequently in winter of northern regions, according to our large ensemble analysis. Therefore, using extratropical SSTs enhances predictability of WF events in northern regions compared to using the full-domain SST index.

When considering SST anomalies across the entire domain, WF events are generally more predictable than WD events, with their predictability being particularly strong in southern regions, especially SWNA and SENA, while WD events are more predictable in northern regions, particularly NCNA. The SST signal in these cases with high predictive skills is also strong (Figures A.17 - A.20, and A.25 - A.28). When focusing on extratropical SSTs, WF events remain generally more predictable than WD events; however, WD predictability increases markedly in southern regions. Since WD events are most frequent in these areas, extratropical SST patterns serve as particularly strong predictors for these events.

Thus, our findings robustly conclude that WF events are more predictable than WD events using different SST domains, with WF predictability consistently higher in southern regions. The greater predictability of WF events in southern regions is particularly notable given that WF SST patterns exhibit stronger anomalies com-

pared to WD events (Ex: SWNA OND, Figure A.28 vs Figure A.4), suggesting more pronounced ocean-atmosphere interactions in these regions during WF occurrences. The underlying mechanisms driving this higher predictability and stronger SST signal in southern regions WF conditions require further investigation.

The null hypothesis, which assumes no predictive relationship between SST and wind extremes, is tested using statistical hypothesis testing to determine whether the observed probability curves for extreme events differ significantly from those expected by random chance. If no significant difference is found, it implies that SST patterns have no real predictive power for WD/WF events. However, comparing the true probability curves with those generated through random sampling reveals that the true curves deviate significantly from the random ones. The true curves generally fall beyond the 95th percentile of the random curves, indicating that the null hypothesis is rejected. This indicates that the observed pattern is generally unlikely to be due to random chance, providing strong evidence to claim the real predictive power of SST patterns for extreme events.

The predictability curves (derived from both whole-domain SST and extratropical SST) provide useful insight into forecasting seasonal anomalous low or high wind speeds across North America, as they consistently demonstrate predictability beyond random chance. In all regions, predictability of extreme events exceeds the 1% threshold, confirming that all cases exhibit predictability beyond what would be expected by chance alone. However, predictability exceeding random chance does not always translate to practical forecast utility. For example, in SCNA during JFM, WD predictability is relatively low, meaning that only less than 20% of events that having a relatively strong projection onto the SST pattern are WD events. In contrast, in the same region during OND, WD predictability exceeds 70%, indicating substantial forecast skill when the pattern index exceeds the 0.7 threshold. The analysis further reveals that nearly half of all WD and WF events are significantly more than 50% predictable, surpassing the "beyond a coin flip" threshold. Thus, both whole-domain SST and extratropical SST provide valuable insights into the predictability of wind extreme events across North America.

The strength and robustness of SST-based predictability, as well as the degree of resemblance to the characteristic SST pattern required for high predictability, vary across models, regions, and seasons. For example, northern regions during JFM and OND exhibit significant strong, robust predictability of WD/WF events, particularly when the SST pattern index exceeds 0.8. In contrast, southern regions

during AMJ and OND also show significant strong and robust predictability, but model disagreement exists regarding the threshold of SST pattern index at which predictability becomes strong. Additionally, in some cases—such as JAS in northern regions—predictability of WD and WF events is neither strong nor robust, with no clear agreement among models on the threshold at which predictability increases. Overall, seasonal predictability of wind extreme events for a given region and season is reliable when it is significantly both strong and robust. Robustness reflects the level of agreement among models, while a high magnitude of predictability indicates practical usefulness for real-world forecasting. If a case demonstrates significant robust but weak predictability, it may be statistically reliable but not practically useful for seasonal wind extreme event forecasting.

It is important to note that while our statistical analysis reveals a strong relationship between SST patterns and extreme wind events, real predictability of extreme wind events remains inherently imperfect. The atmospheric circulation anomalies associated with SST patterns occur on seasonal timescales, which are longer than the synoptic timescales that govern much of the variability in surface winds. From a meteorological perspective, synoptic-scale variability arises from atmospheric instabilities that are unpredictable beyond a few weeks, leading to weather fluctuations even when large-scale seasonal circulation anomalies remain consistent across different years. For example, shifts in storm tracks influence the likelihood of storms in a given region but do not strictly determine their occurrence. This means that even in the presence of a WD SST pattern, for instance, occasional synoptic-scale storms may still occur, despite an overall reduction in storm activity in the region.

Thus, while SST-driven teleconnections shape the probability of extreme wind events, they do not determine their exact occurrence, and predictability remains imperfect. A characteristic SST pattern increases the likelihood of wind extremes but does not garantee them, as the presence or absence of just a few storms within a season may prevent wind speeds from crossing the extreme threshold.

4.5 Limitations and directions for future

While this study offers new insights into the climatology of wind extremes, it also has several limitations, and numerous avenues for future research remain. A key limitation is the reliance on near-surface wind speed data (measured at heights below 10 meters), whereas wind turbines typically operate at hub heights exceeding 80

meters, where wind characteristics, including mean wind speed, turbulence intensity, and shear, can differ significantly. Future work should incorporate wind speed data at hub height to enhance the relevance of the findings for wind energy applications. Furthermore, it is important to note that the results of this study are not directly transferable to seasonal extremes of wind power production, as seasonal mean wind speed does not linearly determine seasonal mean wind power. An accurate assessment of seasonal wind power variability would require high-temporal-resolution wind data (e.g., at least 3-hourly), along with the application of turbine-specific power curves that map wind speed to power output. Incorporating these elements would provide a more accurate assessment of the impacts of seasonal wind variability on power generation.

Additionally, this analysis was conducted using large ensembles from three climate models. The reliability of the results, particularly for wind energy applications, could be further improved by incorporating additional climate models. While our analysis does not reveal a systematic difference between CanRCM and its driving model, CanESM, future studies could explore higher-resolution regional models for two key reasons: (1) they provide a more detailed representation of surface roughness and topography, and (2) the potential systematic differences between an RCM and its driving ESM can be further examined. Additionally, future work could investigate newer versions of CanESM and CanRCM large ensembles, which may feature advancements in model physics and spatial resolution.

This analysis primarily focused on Pacific SSTs, but other large-scale climate modes—such as the Arctic Oscillation (AO) and North Atlantic Oscillation (NAO)—may also contribute to wind variability in North America (Pryor et al., 2020). Future studies should examine these additional factors to gain a more comprehensive understanding of wind extremes in North America.

Moreover, in categorizing SST patterns and identifying characteristic WD/WF SST patterns, a manual approach was used to assess similarities and differences. Employing machine learning techniques could provide a more systematic, data-driven analysis, increasing confidence in the identified patterns. Additionally, the framework developed here could be extended globally to assess whether similar SST-wind relationships hold in different climatic contexts.

Furthermore, the distinct behavior of SENA in response to dominant climate modes such as the PNA could be further examined through an analysis of large ensembles of 500 hPa geopotential height anomalies, allowing for the creation of

corresponding WF/WD composite anomaly maps. Similarly, a deeper investigation into the role of large-scale atmospheric circulation in altering wind direction and driving extreme events in North America could benefit from this approach.

Since extratropical SSTs have been found to be more effective in predicting extreme wind events, a future analysis could more systematically examine the relationship between seasonal extremes and different variability patterns that may better capture large-scale SST variations in the extratropical North Pacific, such as the North Pacific Index (NPI), North Pacific Gyre Oscillation (NPGO), and Pacific Decadal Oscillation (PDO).

Future research could also investigate long-term climate change impacts on the occurrence and intensity of wind extremes in North America, examining how wind-SST relationships may change under future climate scenarios. Large ensemble projections until the late 21st century could be used to assess changes in different future periods.

Studies such as Ma et al. (2022) suggest that wind power density in Canada is projected to increase in winter but decrease in summer across all regions, highlighting the importance of understanding seasonal wind variability in a changing climate. Expanding the historical analysis to future climate projections could provide valuable insights into how wind extremes are expected to evolve under different greenhouse gas emission scenarios, supporting long-term energy planning and climate adaptation strategies.

Appendix A

Wind-SST Figures, all regions, seasons, models

A.1 Wind Drought

A.1.1 SWNA

1. JFM

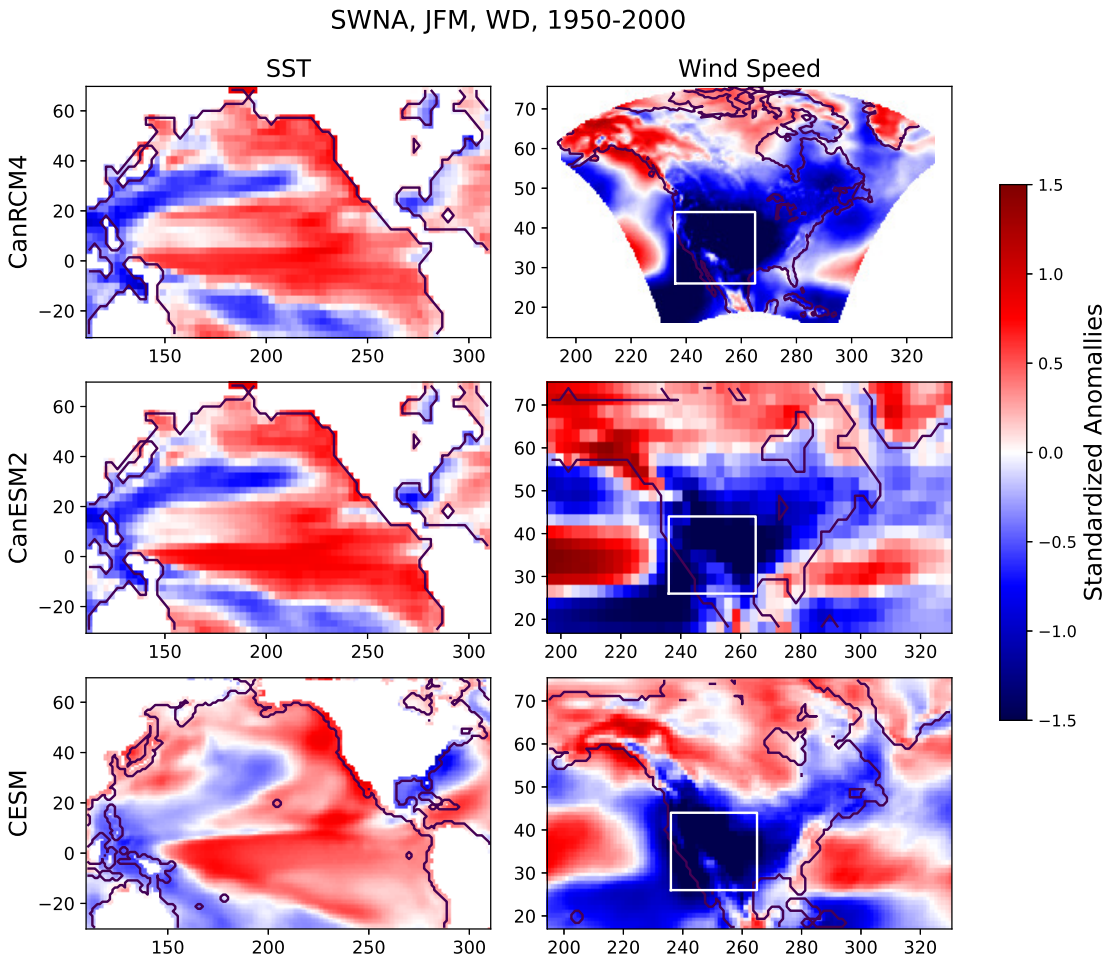

Figure A.1: JFM mean of standardized anomaly of Sea Surface Temperature and surface wind speed in SWNA for WD events, in 1950-2000. First row: CanRCM4, second row: CanESM2, third row: CESM.

2. AMJ

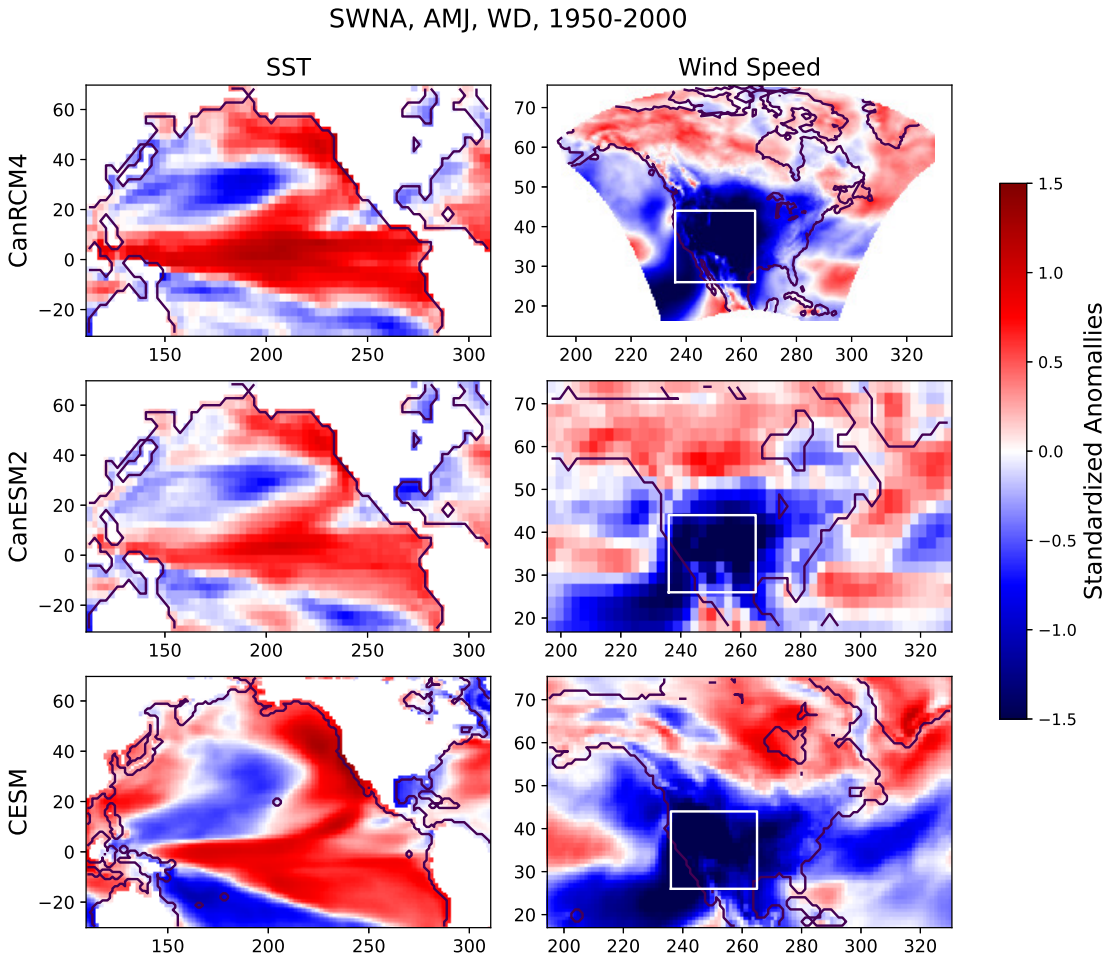

Figure A.2: AMJ mean of standardized anomaly of Sea Surface Temperature and surface wind speed in SWNA for WD events, in 1950-2000. First row: CanRCM4, second row: CanESM2, third row: CESM.

3. JAS

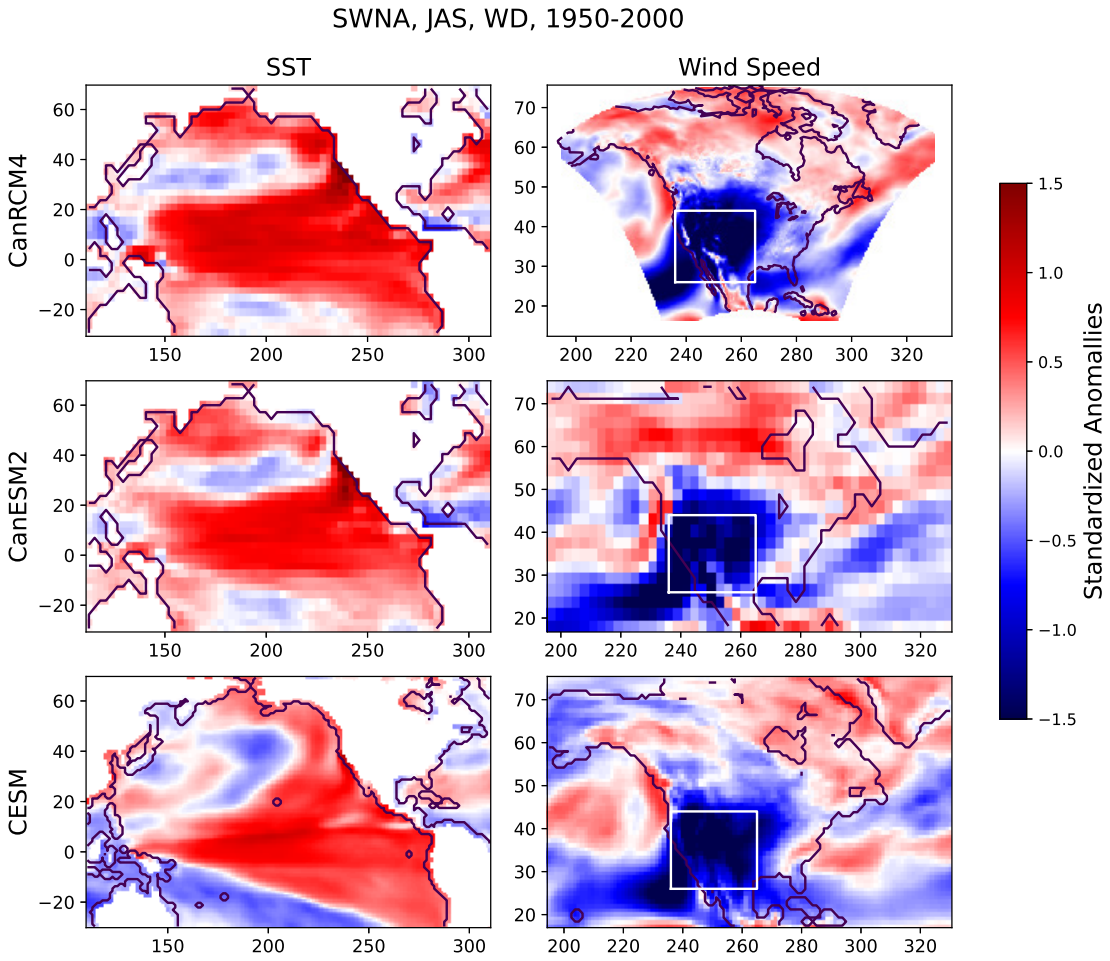

Figure A.3: JAS mean of standardized anomaly of Sea Surface Temperature and surface wind speed in SWNA for WD events, in 1950-2000. First row: CanRCM4 , second row: CanESM2, third row: CESM.

4. OND

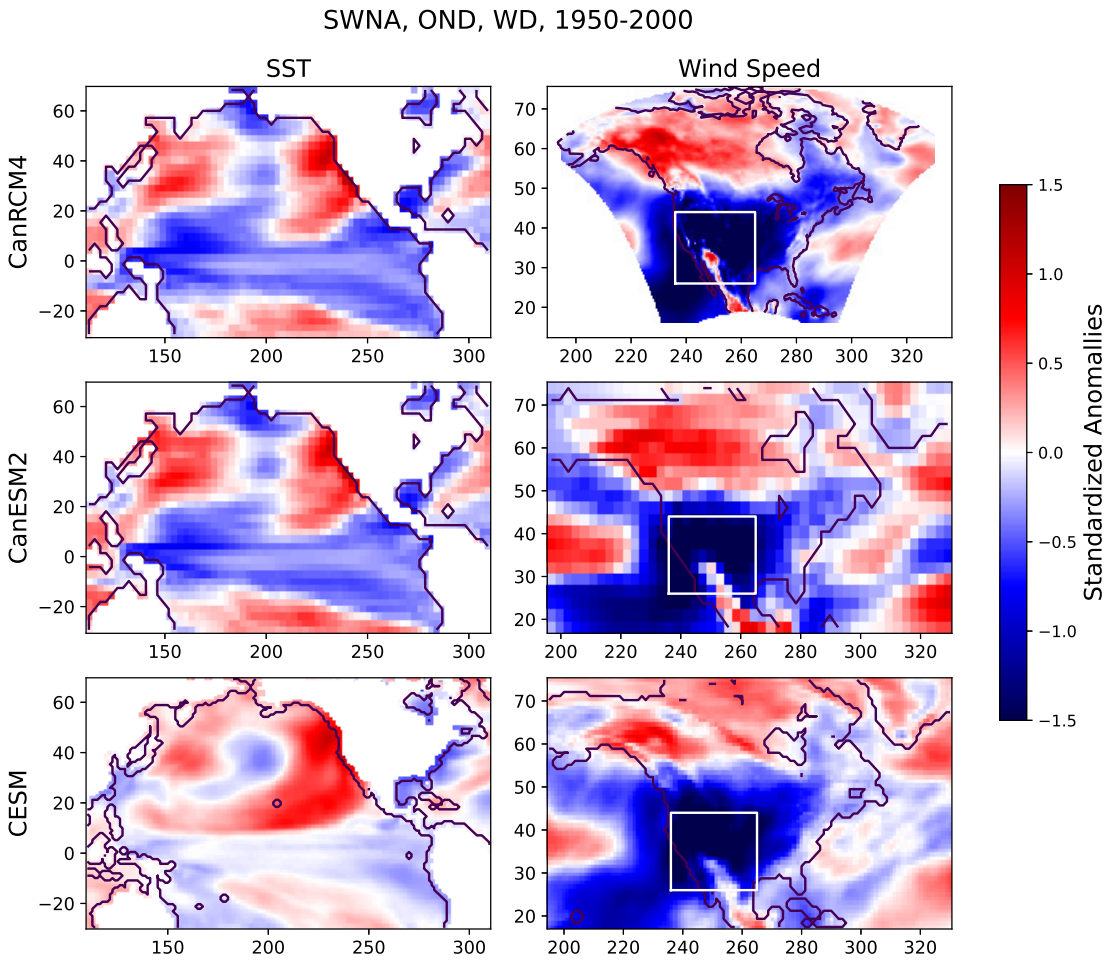

Figure A.4: OND mean of standardized anomaly of Sea Surface Temperature and surface wind speed in SWNA for WD events, in 1950-2000. First row: CanRCM4 , second row: CanESM2, third row: CESM.

A.1.2 SCNA

1. JFM

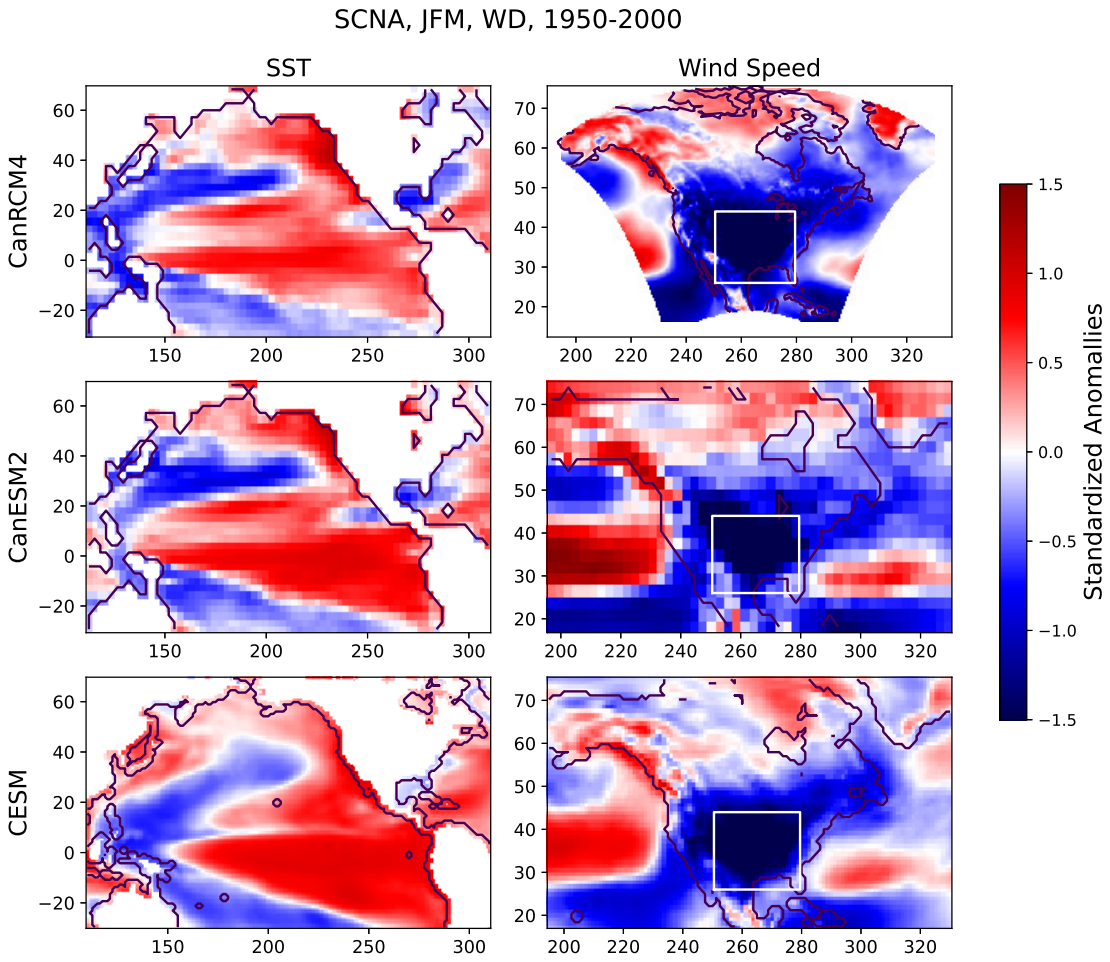

Figure A.5: JFM mean of standardized anomaly of Sea Surface Temperature and surface wind speed in SCNA for WD events, in 1950-2000. First row: CanRCM4 , second row: CanESM2, third row: CESM.

2. AMJ

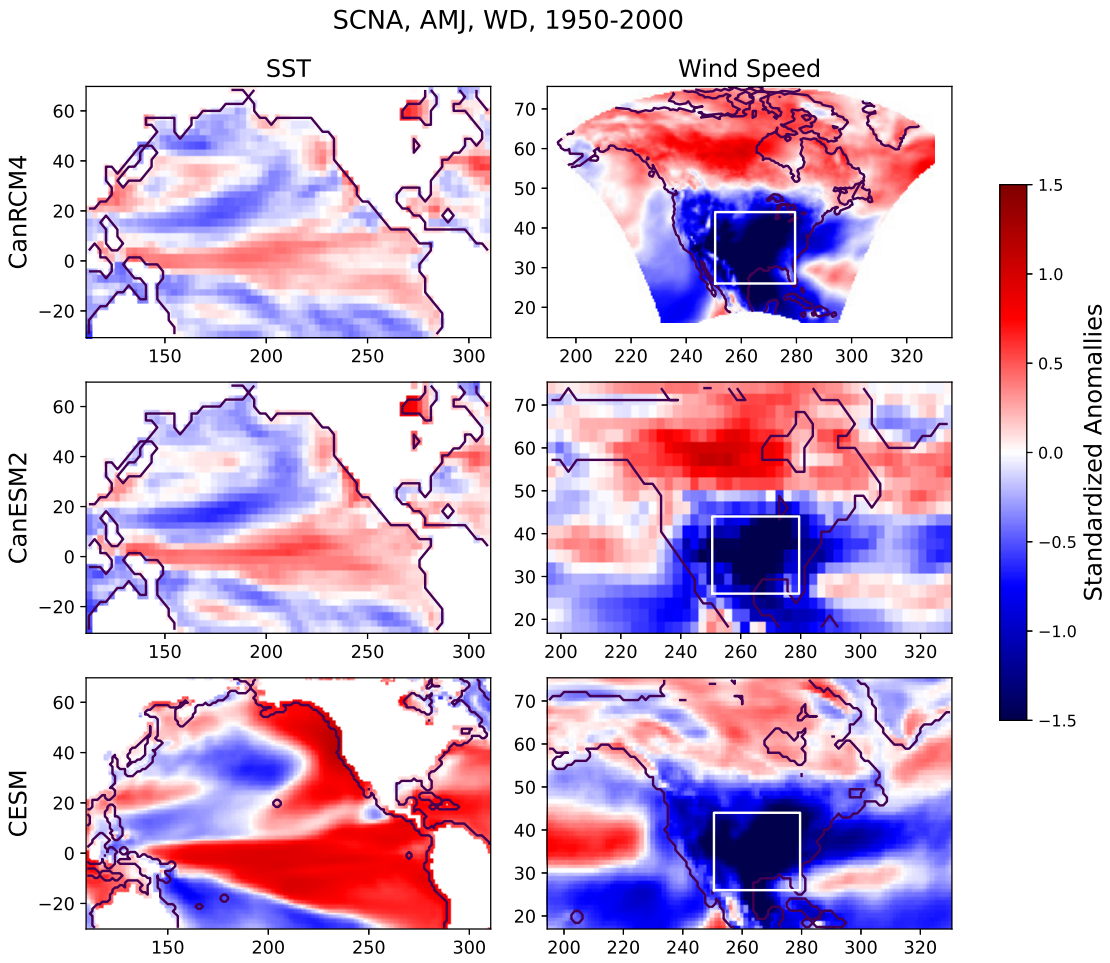

Figure A.6: AMJ mean of standardized anomaly of Sea Surface Temperature and surface wind speed in SCNA for WD events, in 1950-2000. First row: CanRCM4 , second row: CanESM2, third row: CESM.

3. JAS

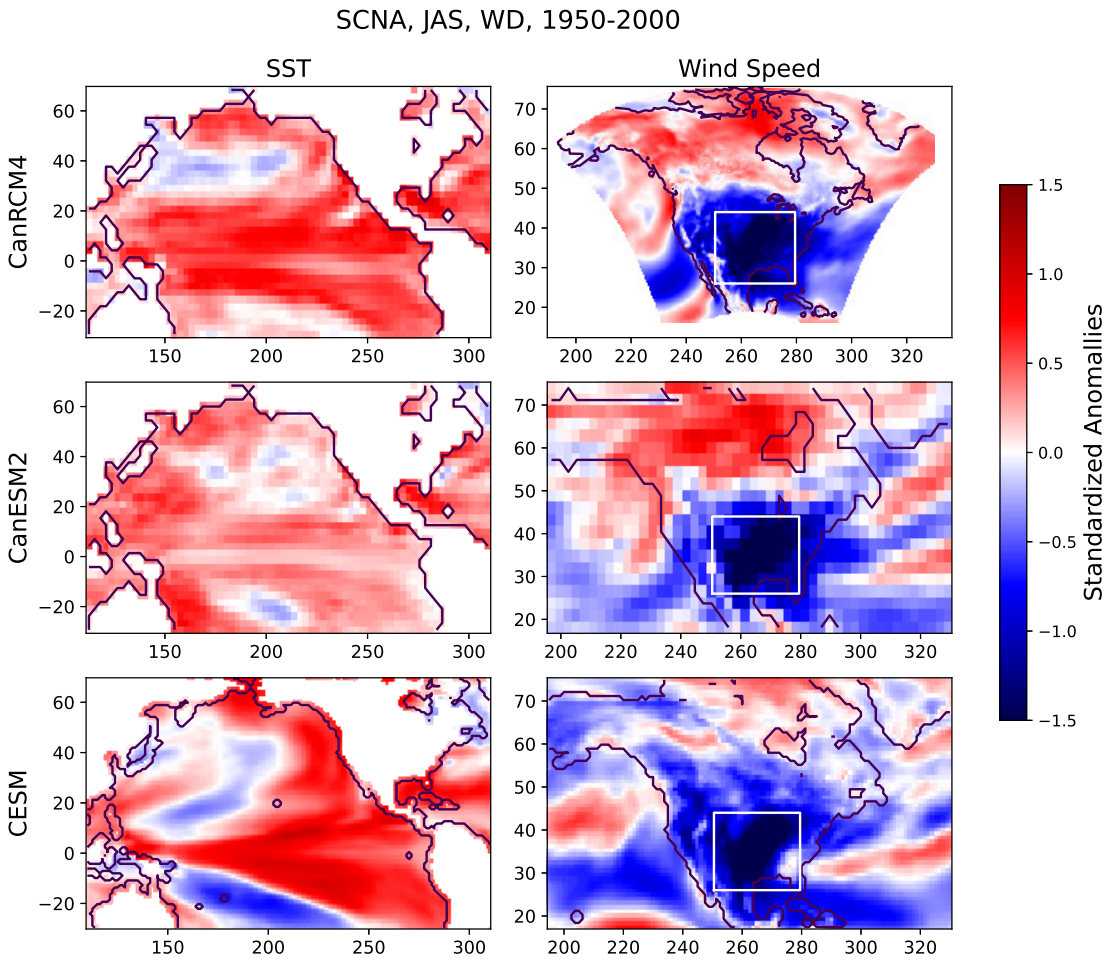

Figure A.7: JAS mean of standardized anomaly of Sea Surface Temperature and surface wind speed in SCNA for WD events, in 1950-2000. First row: CanRCM4 , second row: CanESM2, third row: CESM.

4. OND

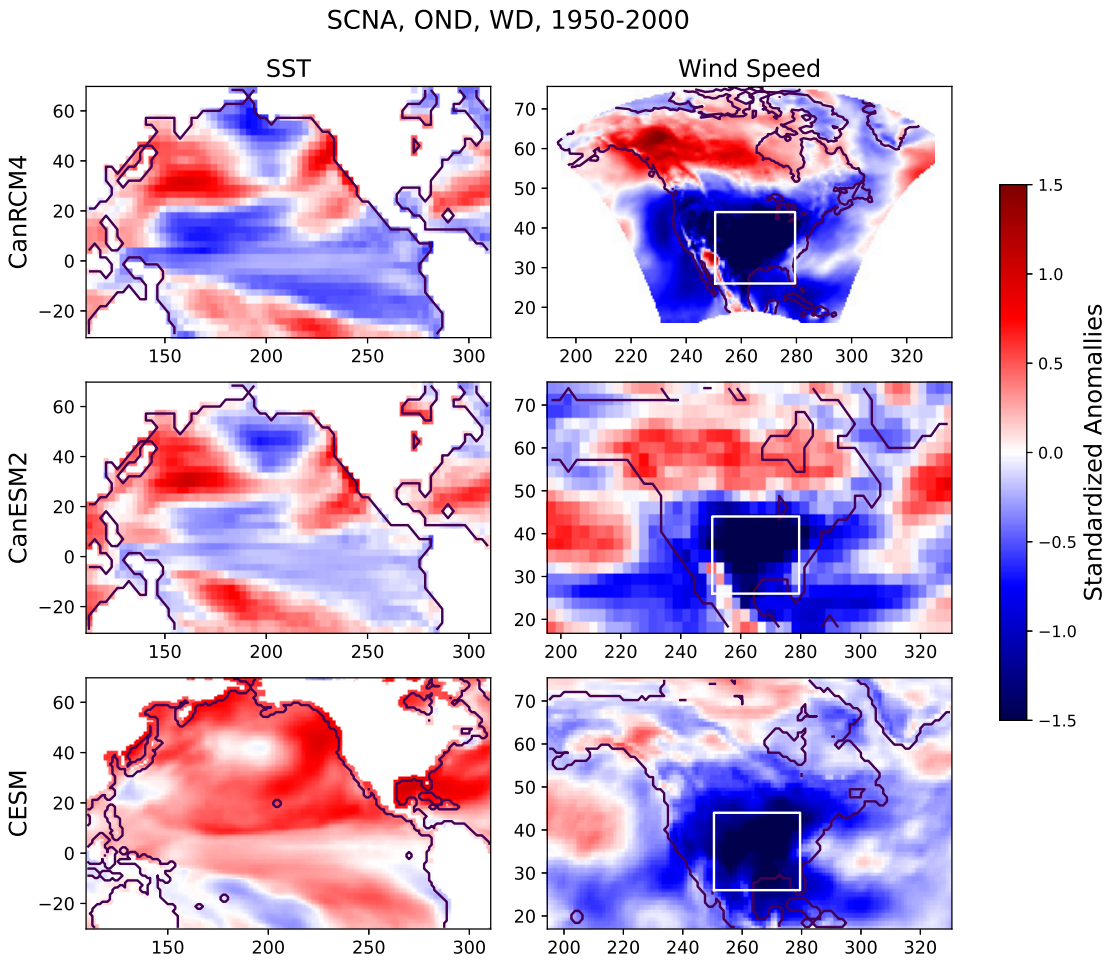

Figure A.8: OND mean of standardized anomaly of Sea Surface Temperature and surface wind speed in SCNA for WD events, in 1950-2000. First row: CanRCM4 , second row: CanESM2, third row: CESM.

A.1.3 SENA

1. JFM

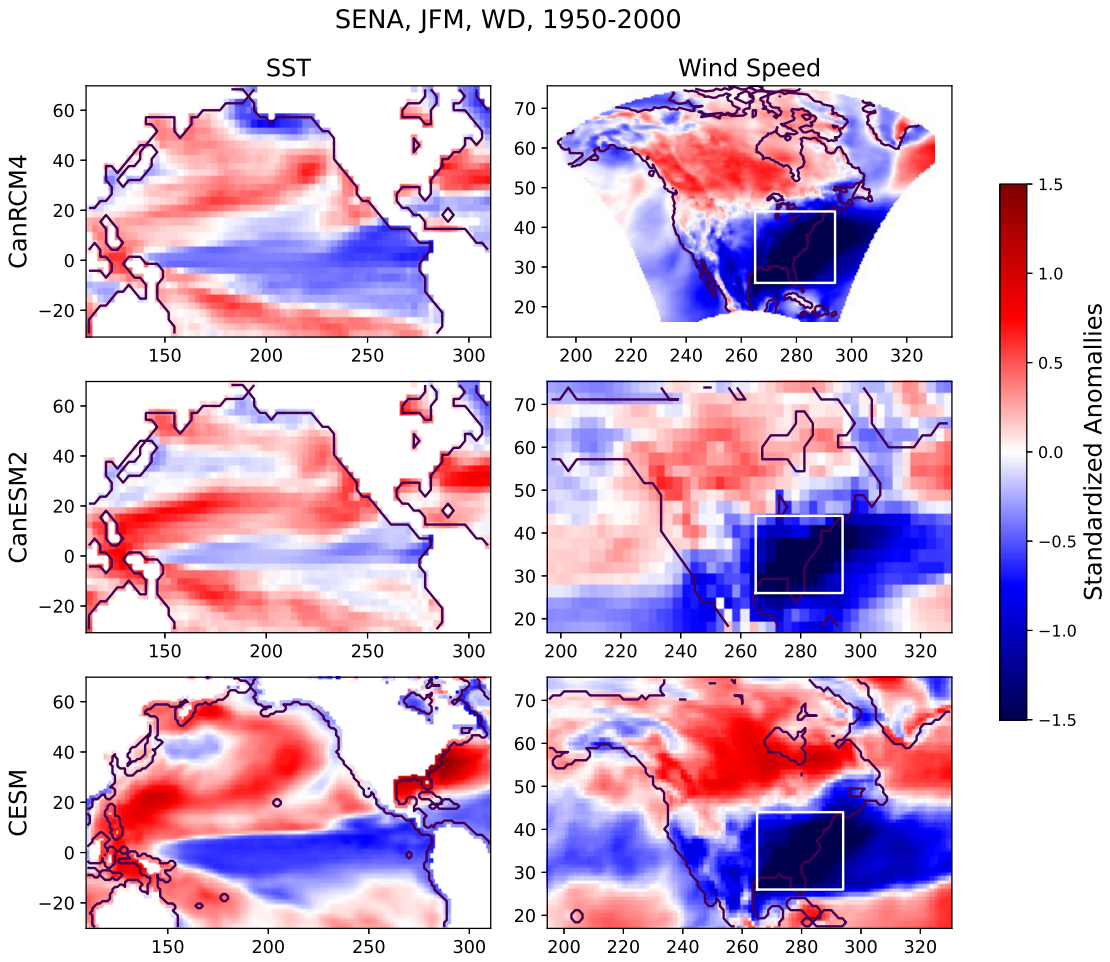

Figure A.9: JFM mean of standardized anomaly of Sea Surface Temperature and surface wind speed in SENA for WD events, in 1950-2000. First row: CanRCM4 , second row: CanESM2, third row: CESM.

2. AMJ

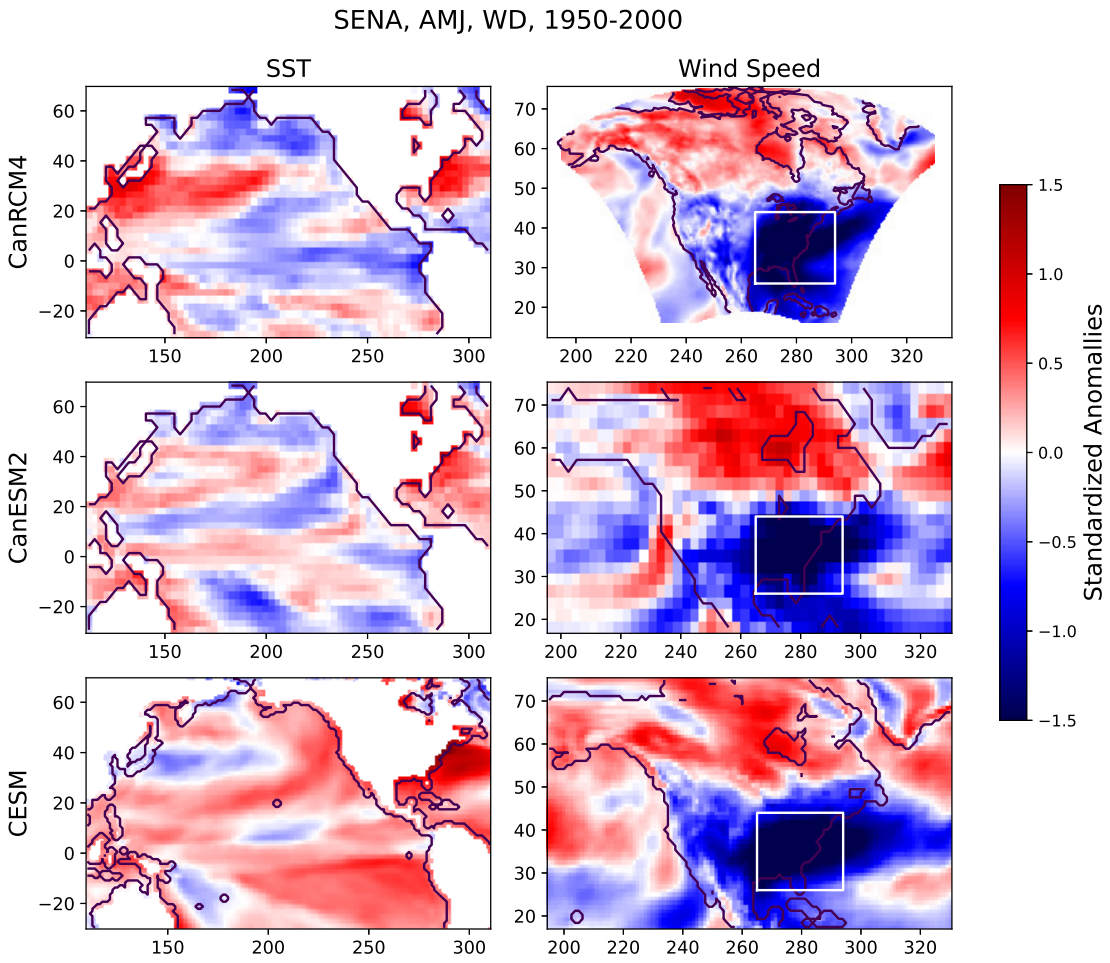

Figure A.10: AMJ mean of standardized anomaly of Sea Surface Temperature and surface wind speed in SENA for WD events, in 1950-2000. First row: CanRCM4 , second row: CanESM2, third row: CESM.

3. JAS

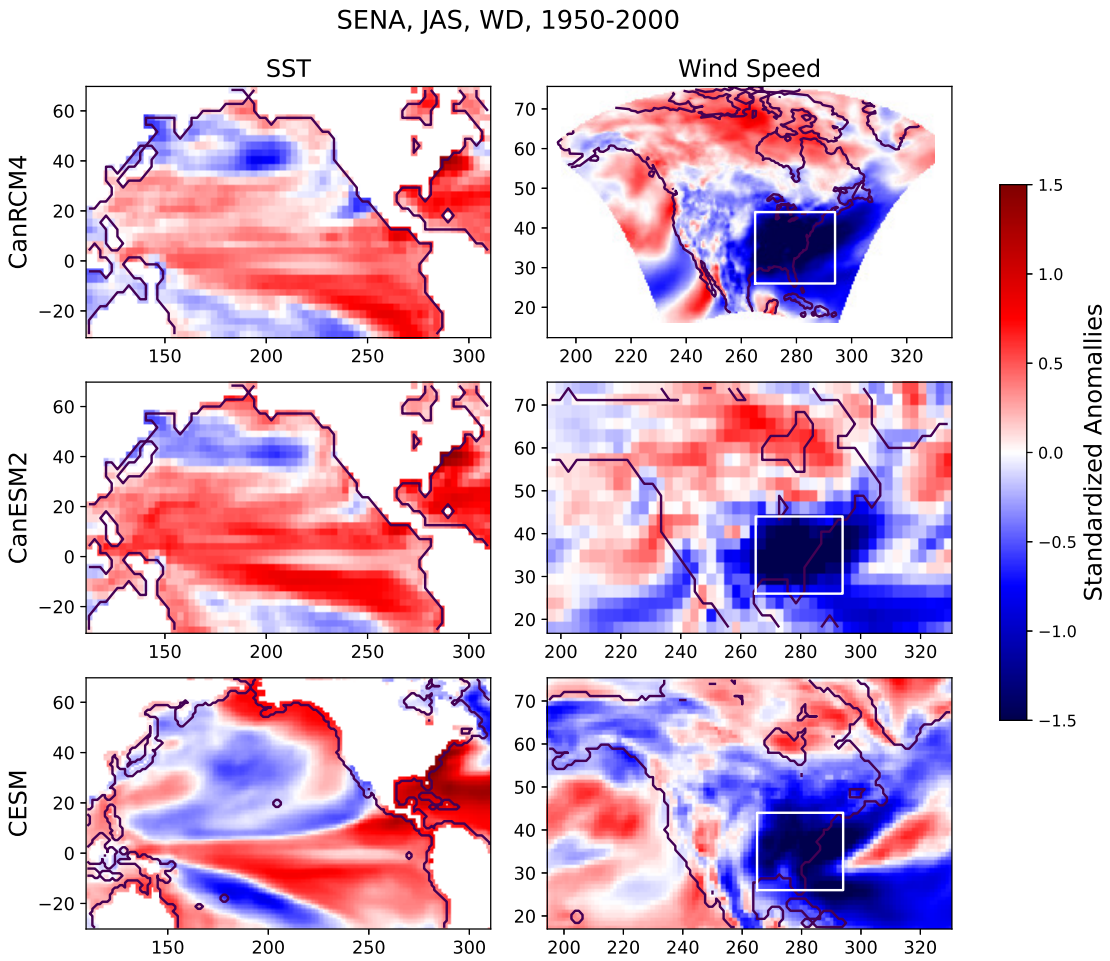

Figure A.11: JAS mean of standardized anomaly of Sea Surface Temperature and surface wind speed in SENA for WD events, in 1950-2000. First row: CanRCM4 , second row: CanESM2, third row: CESM.

4. OND

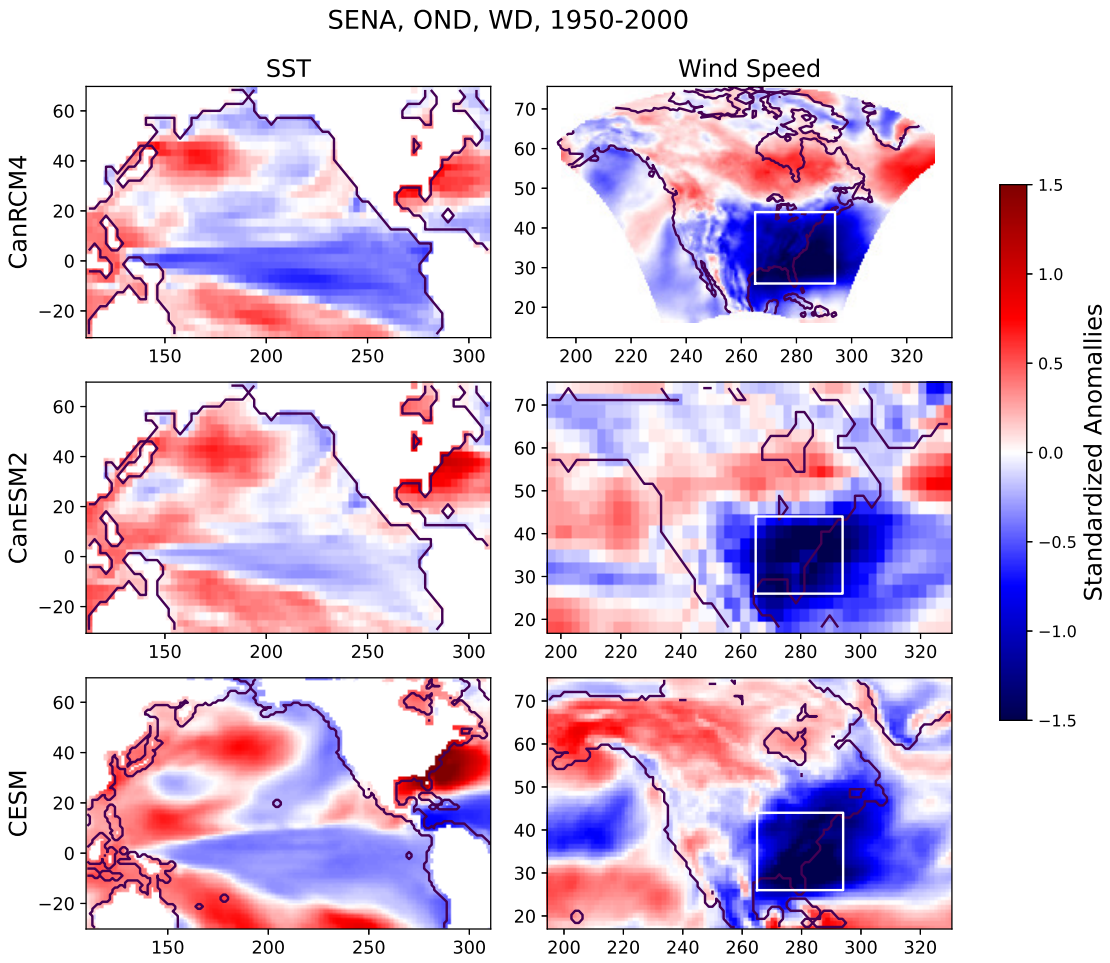

Figure A.12: OND mean of standardized anomaly of Sea Surface Temperature and surface wind speed in SENA for WD events, in 1950-2000. First row: CanRCM4 , second row: CanESM2, third row: CESM.

A.1.4 NWNA

1. JFM

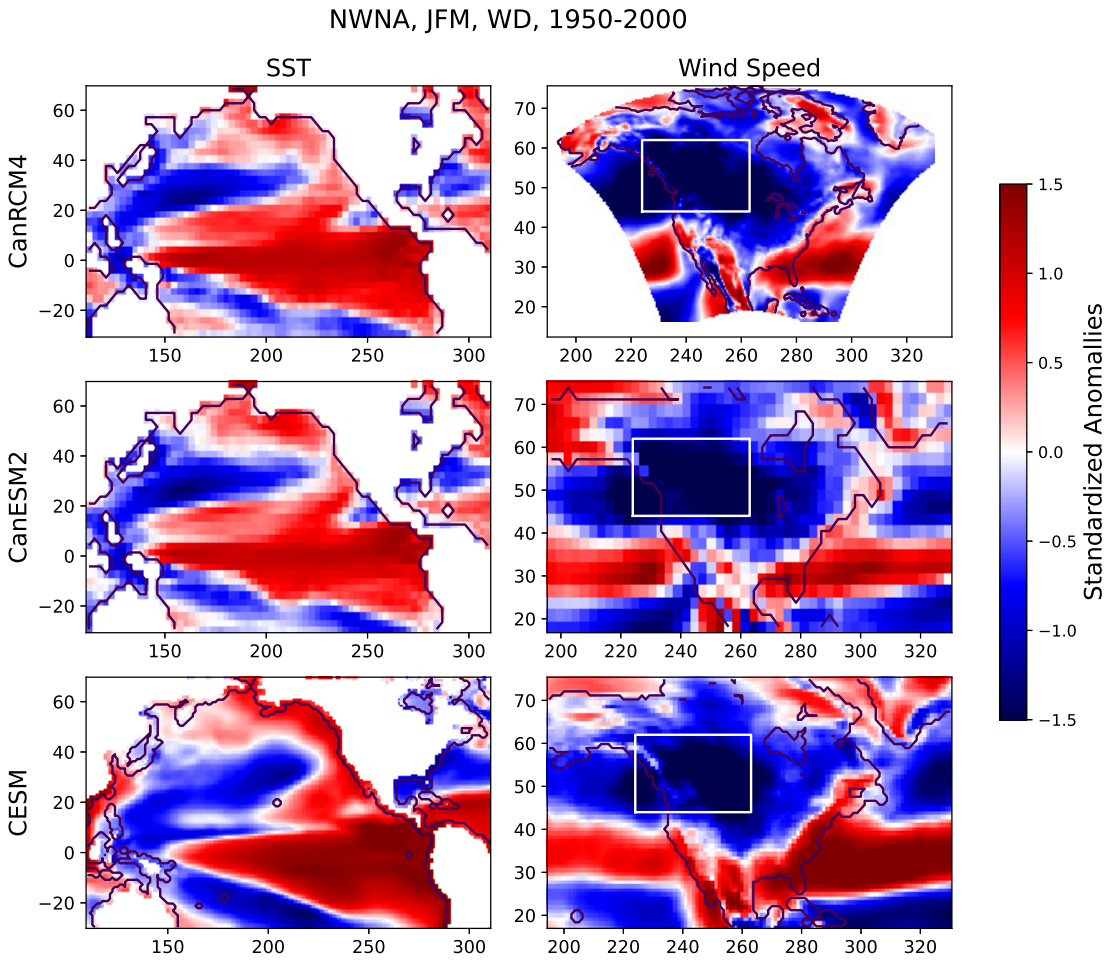

Figure A.13: JFM mean of standardized anomaly of Sea Surface Temperature and surface wind speed in NWNA for WD events, in 1950-2000. First row: CanRCM4 , second row: CanESM2, third row: CESM.

2. AMJ

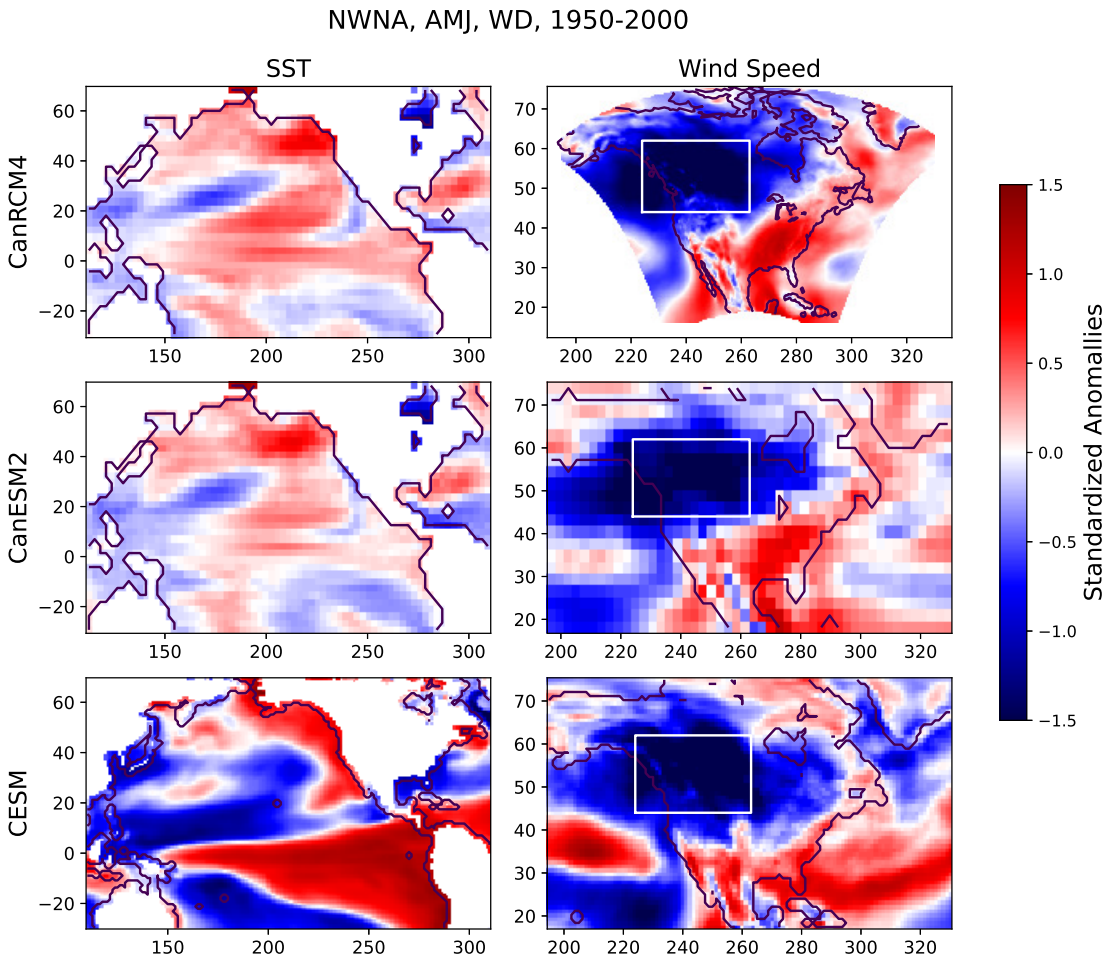

Figure A.14: AMJ mean of standardized anomaly of Sea Surface Temperature and surface wind speed in NWNA for WD events, in 1950-2000. First row: CanRCM4 , second row: CanESM2, third row: CESM.

3. JAS

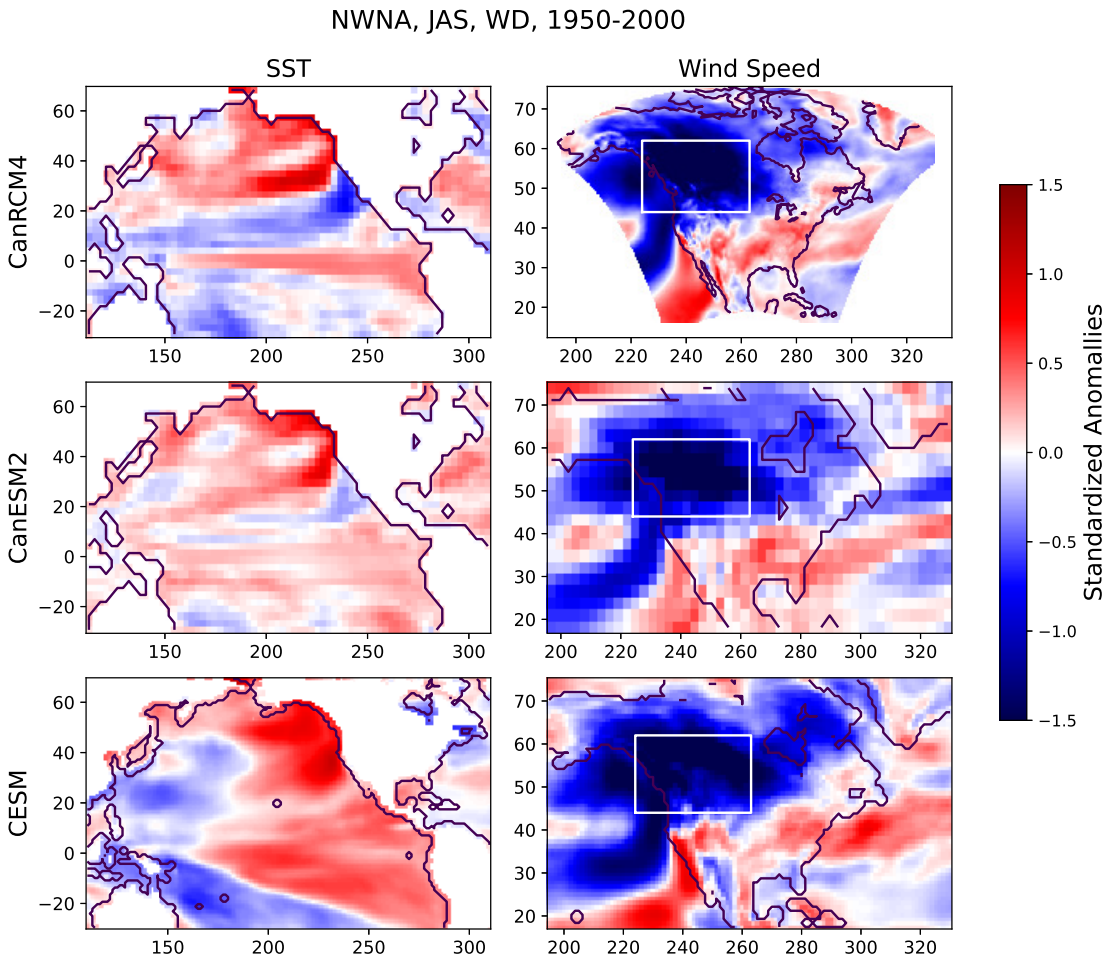

Figure A.15: JAS mean of standardized anomaly of Sea Surface Temperature and surface wind speed in NWNA for WD events, in 1950-2000. First row: CanRCM4 , second row: CanESM2, third row: CESM.

4. OND

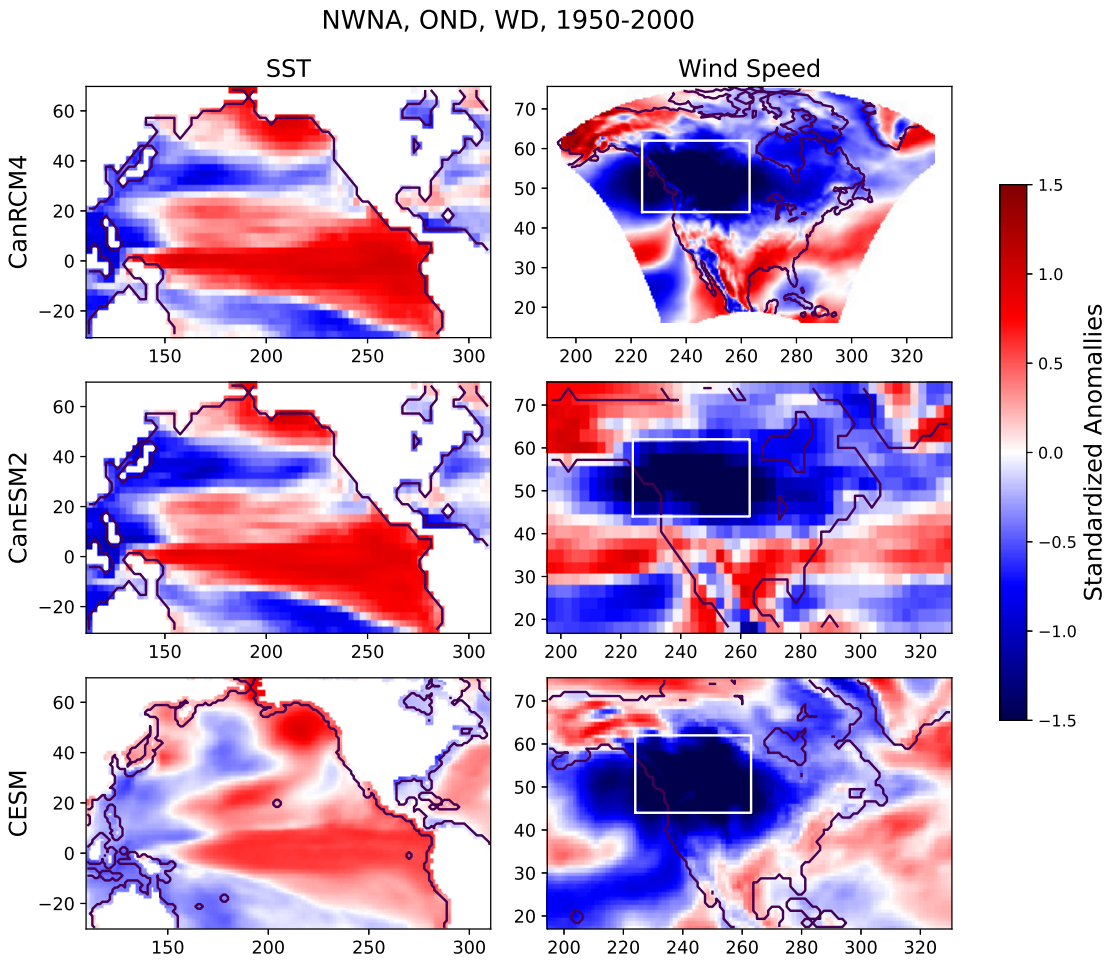

Figure A.16: OND mean of standardized anomaly of Sea Surface Temperature and surface wind speed in NWNA for WD events, in 1950-2000. First row: CanRCM4 , second row: CanESM2, third row: CESM.

A.1.5 NCNA

1. JFM

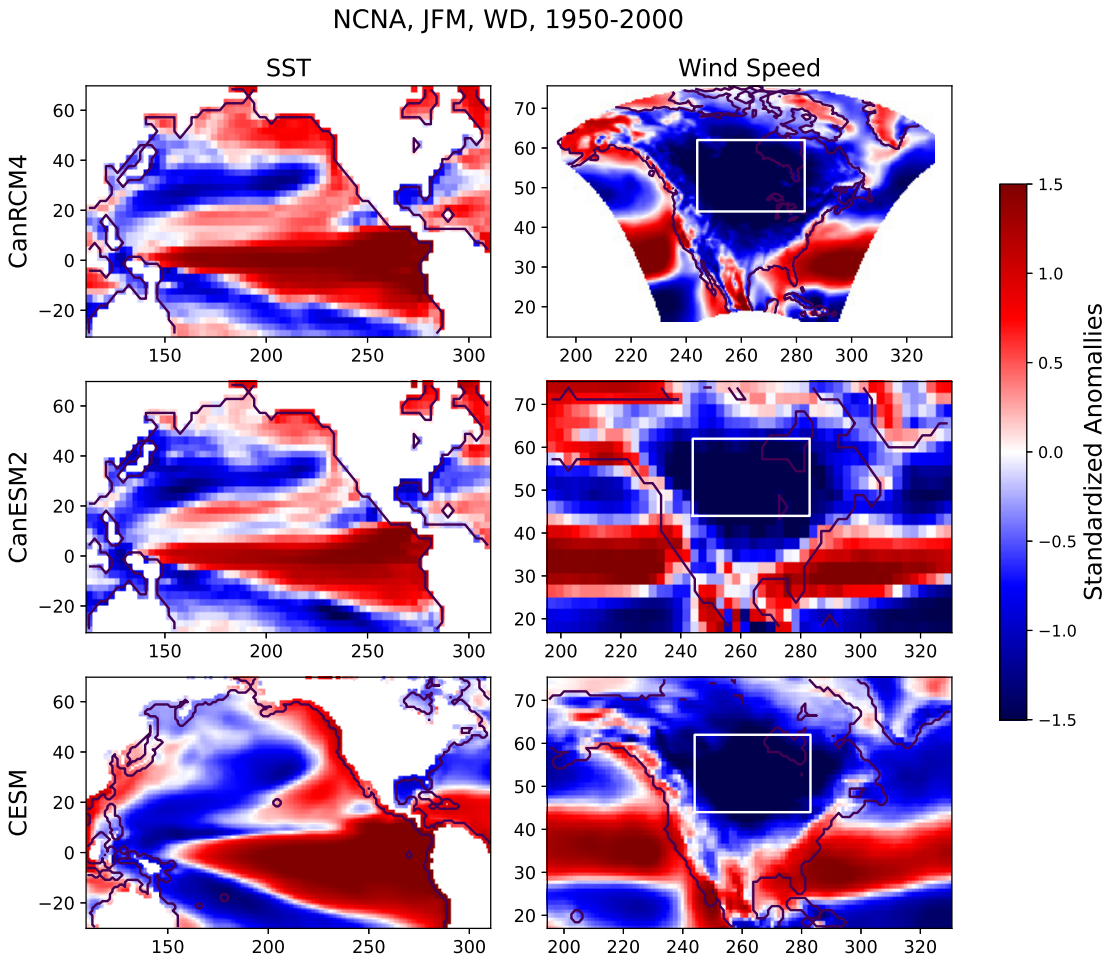

Figure A.17: JFM mean of standardized anomaly of Sea Surface Temperature and surface wind speed in NCNA for WD events, in 1950-2000. First row: CanRCM4 , second row: CanESM2, third row: CESM.

2. AMJ

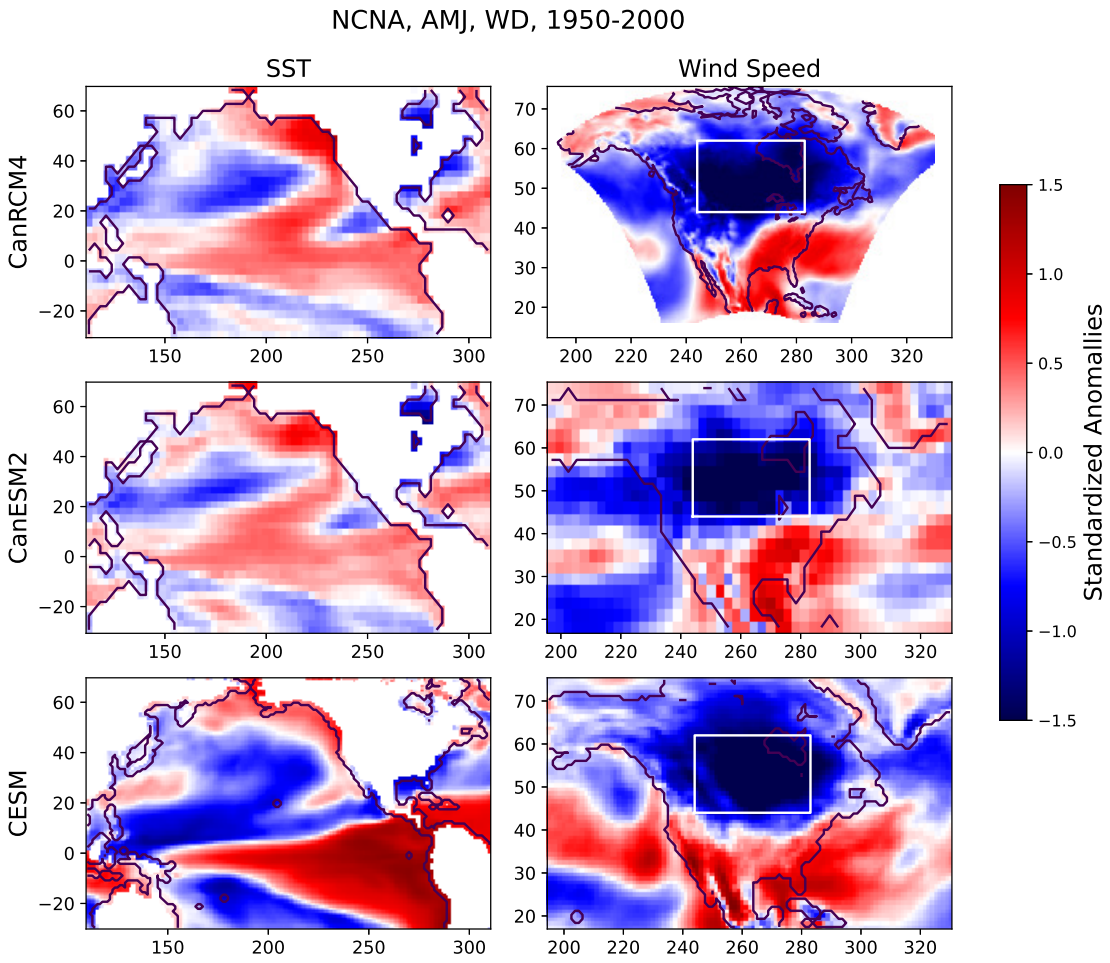

Figure A.18: AMJ mean of standardized anomaly of Sea Surface Temperature and surface wind speed in NCNA for WD events, in 1950-2000. First row: CanRCM4 , second row: CanESM2, third row: CESM.

3. JAS

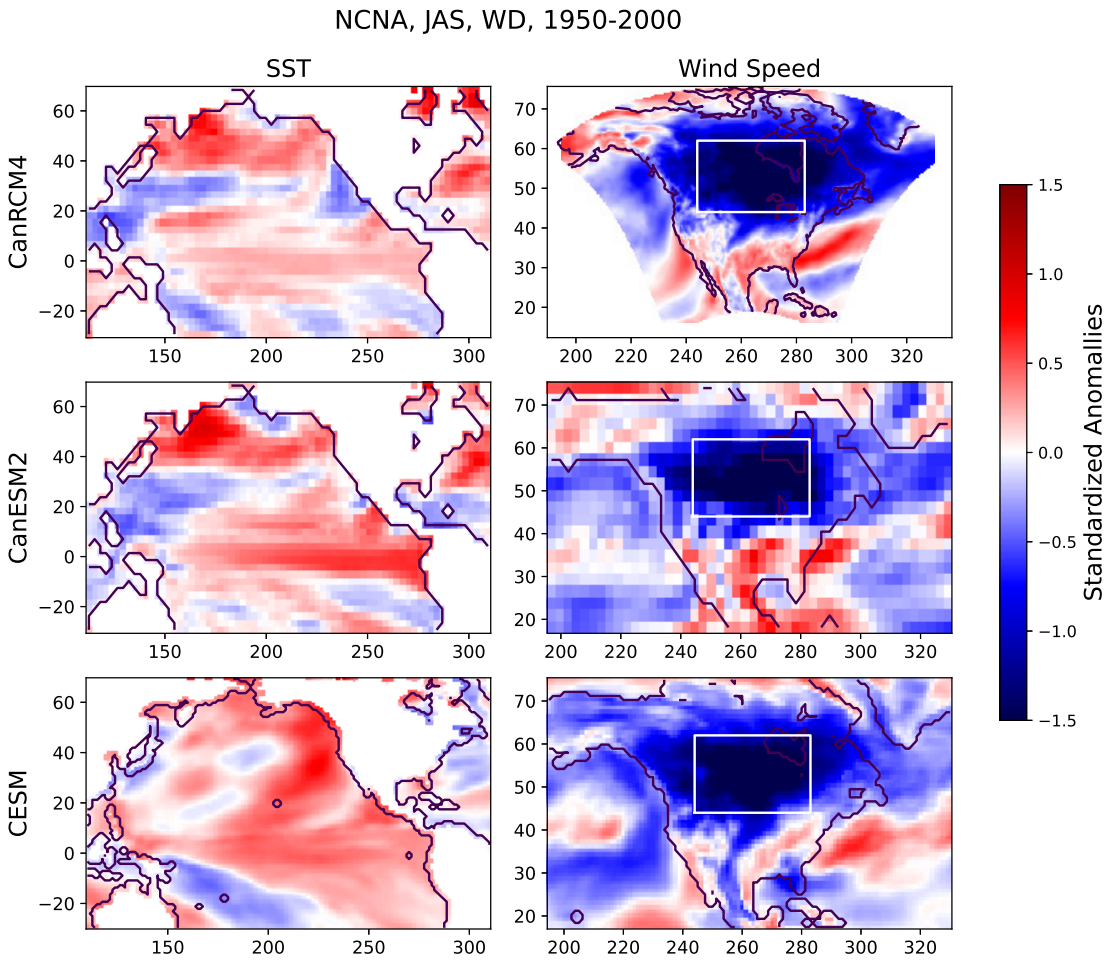

Figure A.19: JAS mean of standardized anomaly of Sea Surface Temperature and surface wind speed in NCNA for WD events, in 1950-2000. First row: CanRCM4 , second row: CanESM2, third row: CESM.

4. OND

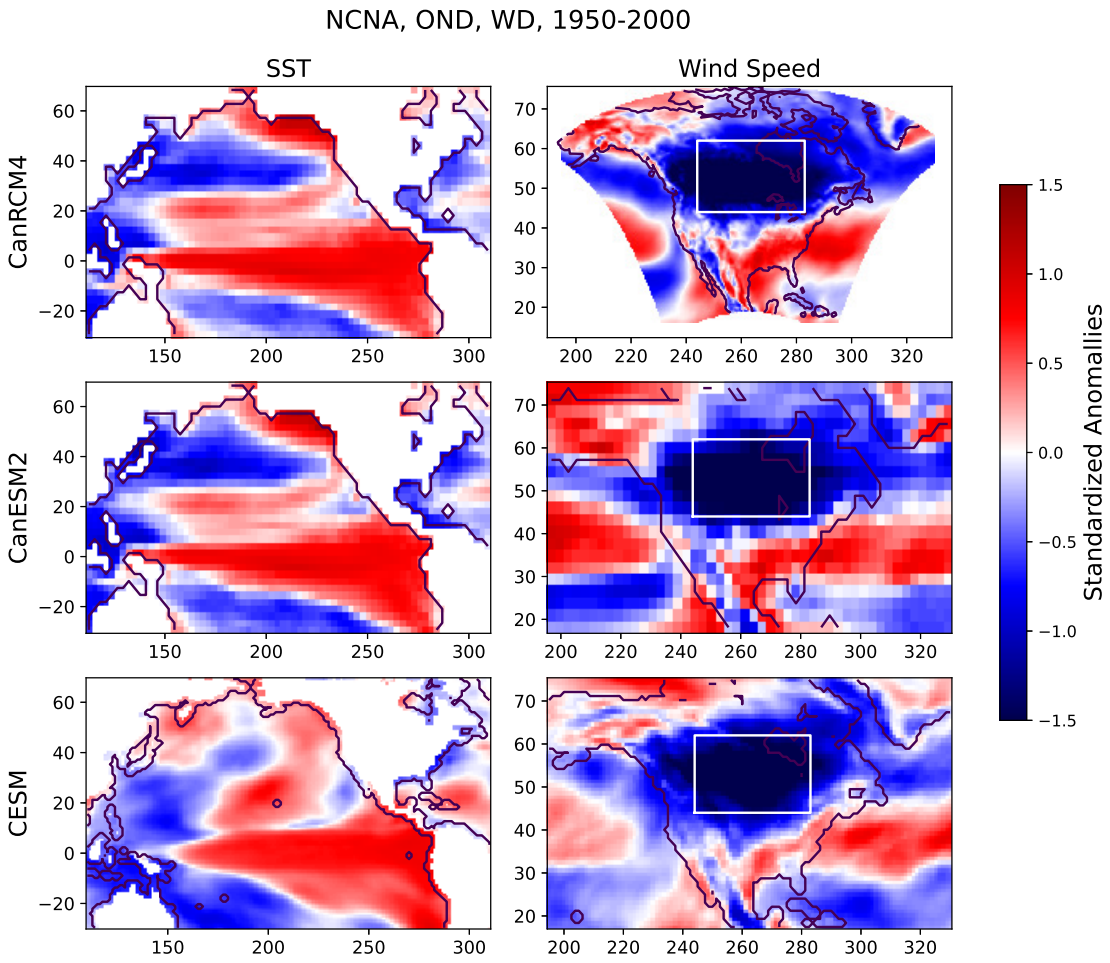

Figure A.20: OND mean of standardized anomaly of Sea Surface Temperature and surface wind speed in NCNA for WD events, in 1950-2000. First row: CanRCM4 , second row: CanESM2, third row: CESM.

A.1.6 NENA

1. JFM

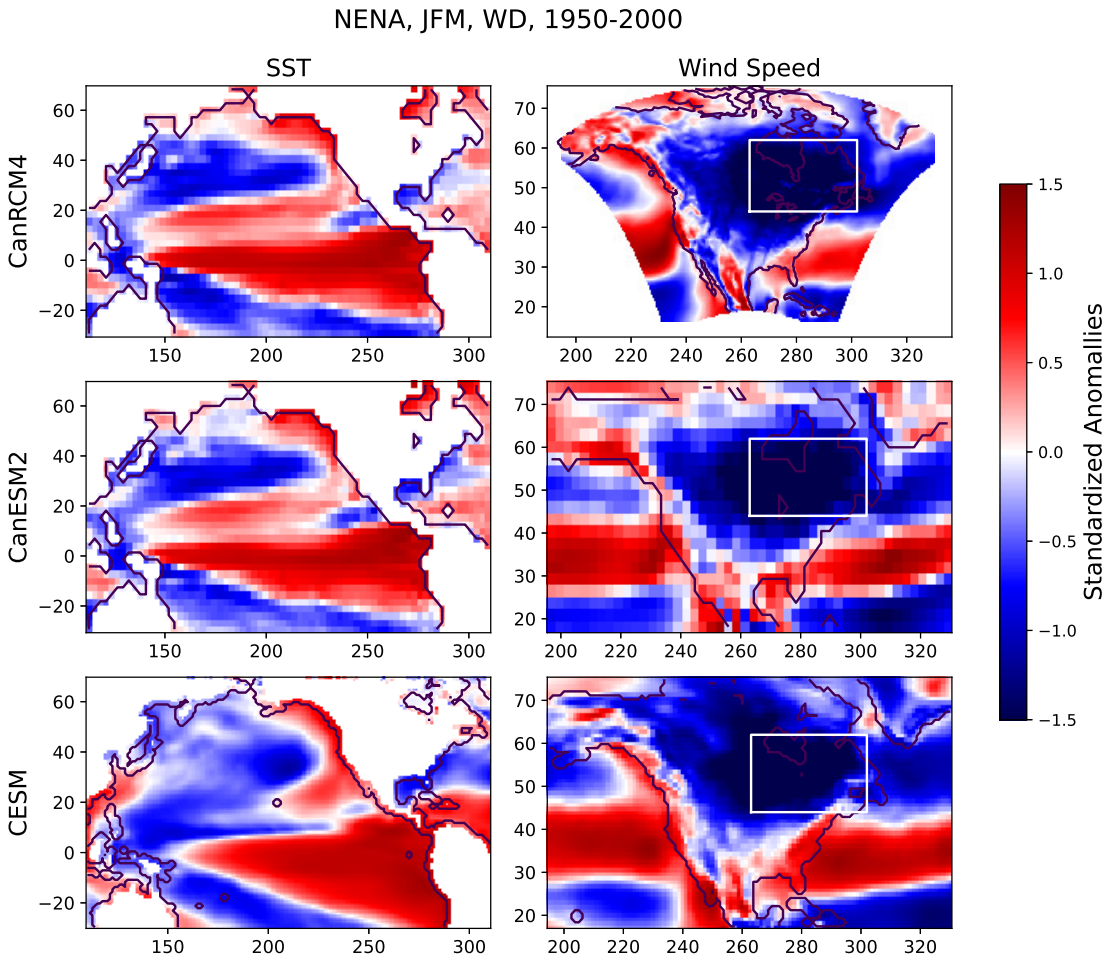

Figure A.21: JFM mean of standardized anomaly of Sea Surface Temperature and surface wind speed in NENA for WD events, in 1950-2000. First row: CanRCM4 , second row: CanESM2, third row: CESM.

2. AMJ

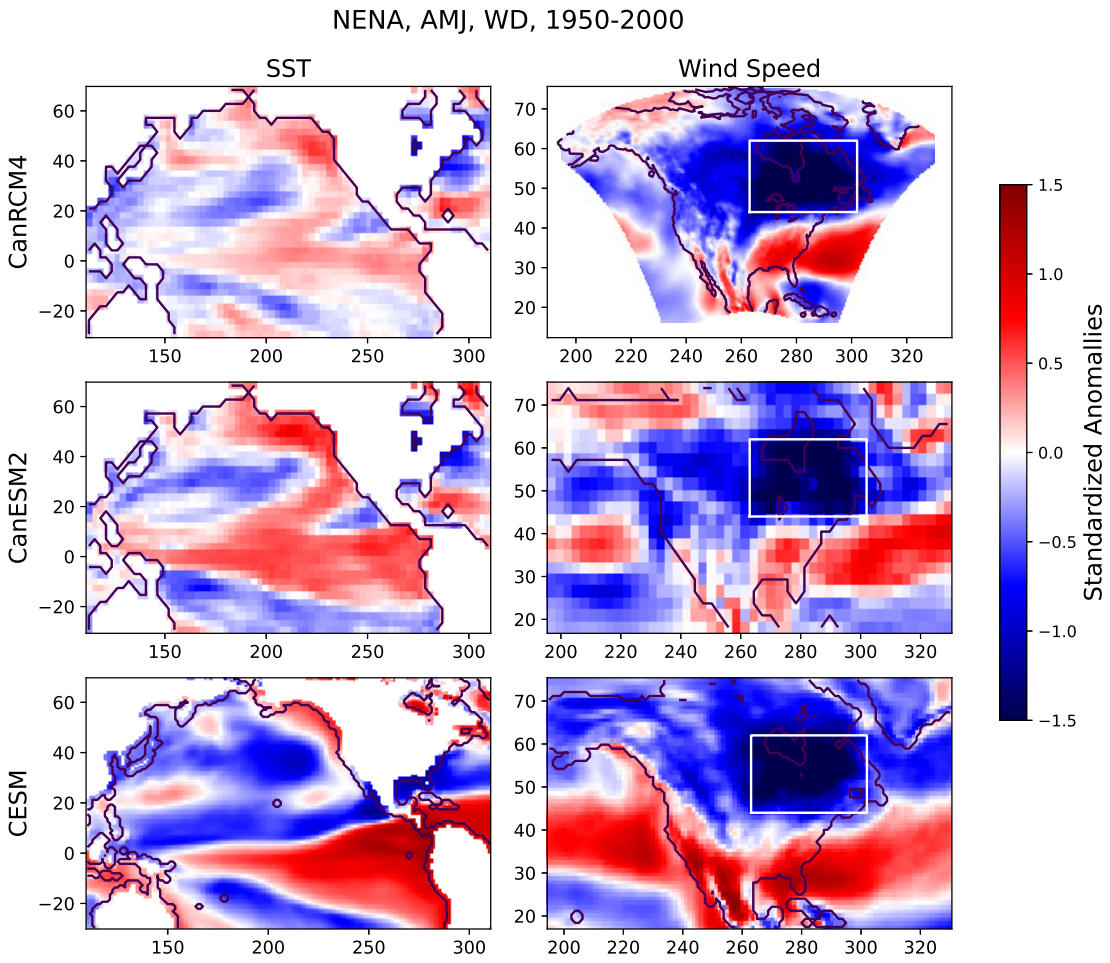

Figure A.22: AMJ mean of standardized anomaly of Sea Surface Temperature and surface wind speed in NENA for WD events, in 1950-2000. First row: CanRCM4 , second row: CanESM2, third row: CESM.

3. JAS

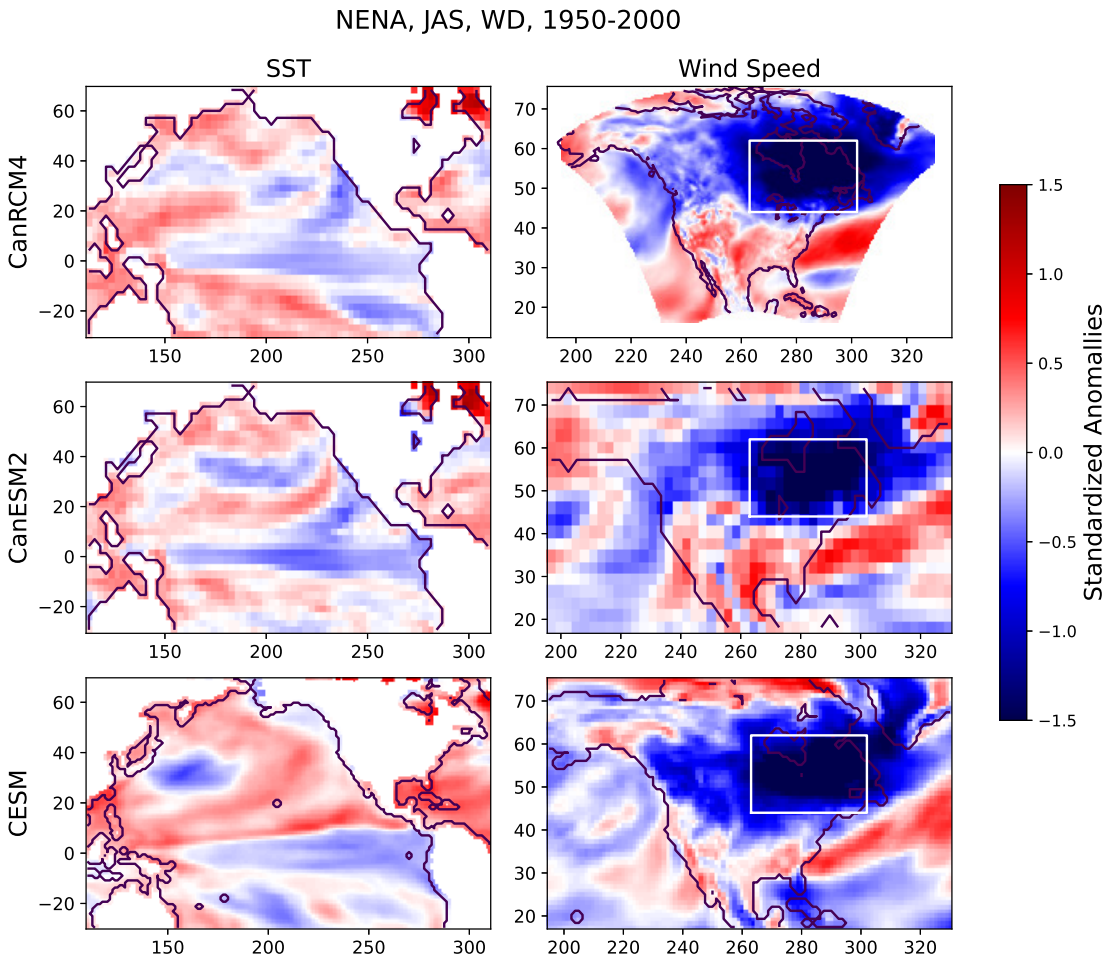

Figure A.23: JAS mean of standardized anomaly of Sea Surface Temperature and surface wind speed in NENA for WD events, in 1950-2000. First row: CanRCM4 , second row: CanESM2, third row: CESM.

4. OND

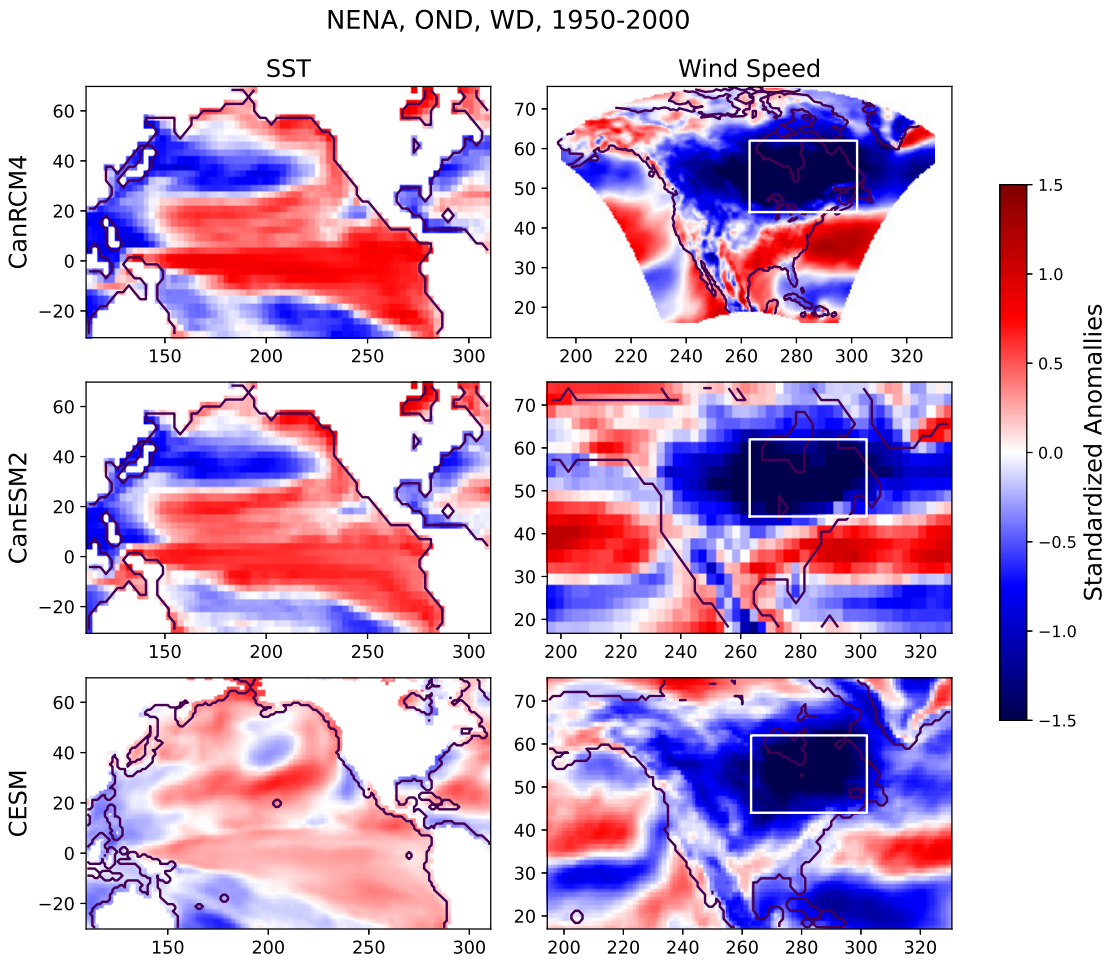

Figure A.24: OND mean of standardized anomaly of Sea Surface Temperature and surface wind speed in NENA for WD events, in 1950-2000. First row: CanRCM4 , second row: CanESM2, third row: CESM.

A.2 Wind Flood

A.2.1 SWNA

1. JFM

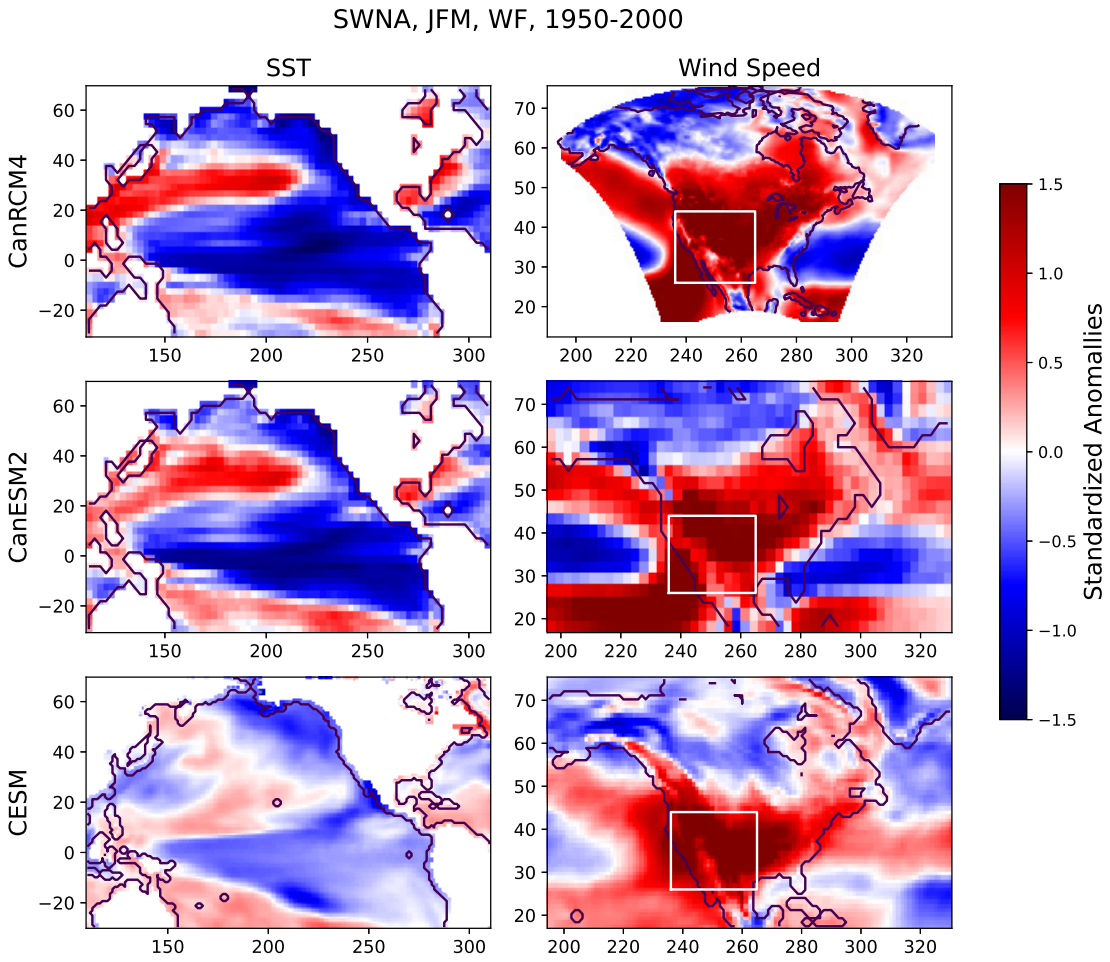

Figure A.25: JFM mean of standardized anomaly of Sea Surface Temperature and surface wind speed in SWNA for WF events, in 1950-2000. First row: CanRCM4 , second row: CanESM2, third row: CESM.

2. AMJ

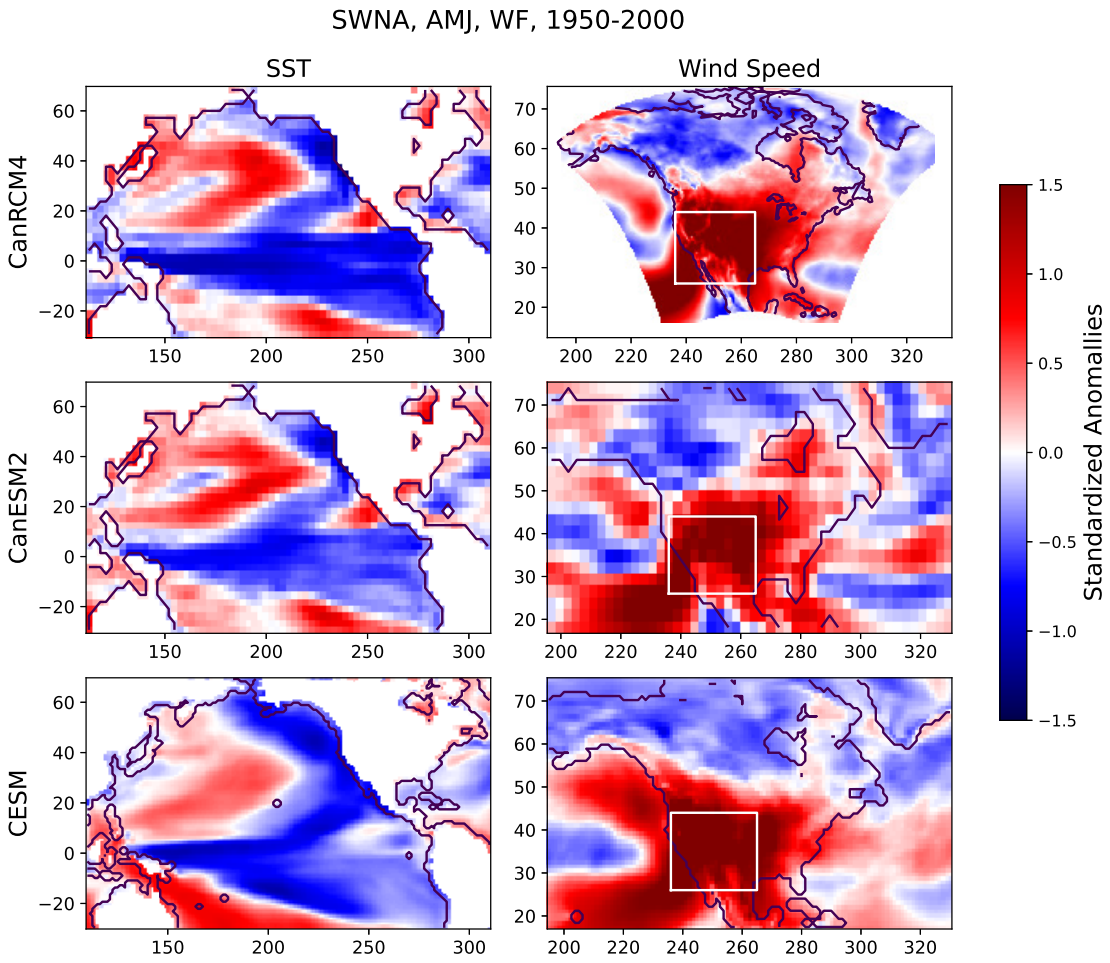

Figure A.26: AMJ mean of standardized anomaly of Sea Surface Temperature and surface wind speed in SWNA for WF events, in 1950-2000. First row: CanRCM4 , second row: CanESM2, third row: CESM.

3. JAS

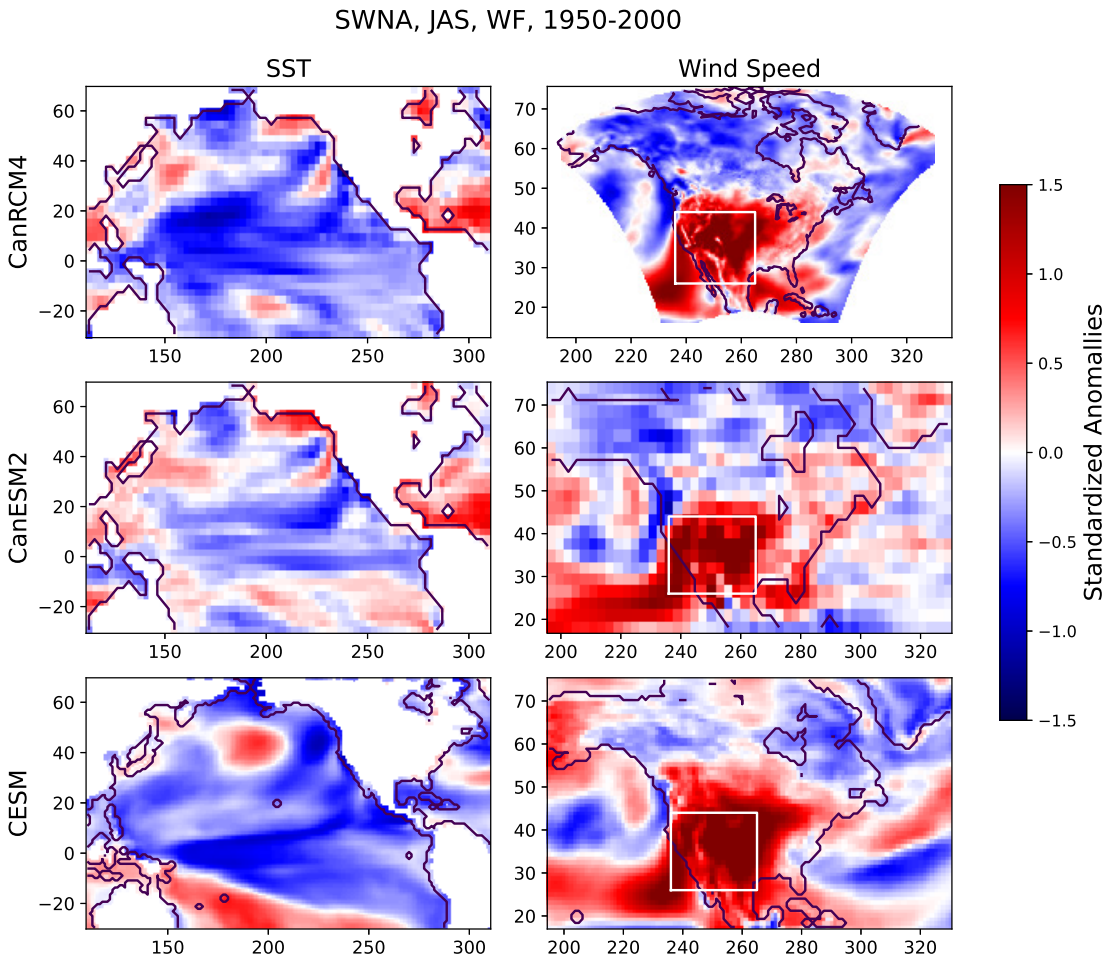

Figure A.27: JAS mean of standardized anomaly of Sea Surface Temperature and surface wind speed in SWNA for WF events, in 1950-2000. First row: CanRCM4 , second row: CanESM2, third row: CESM.

4. OND

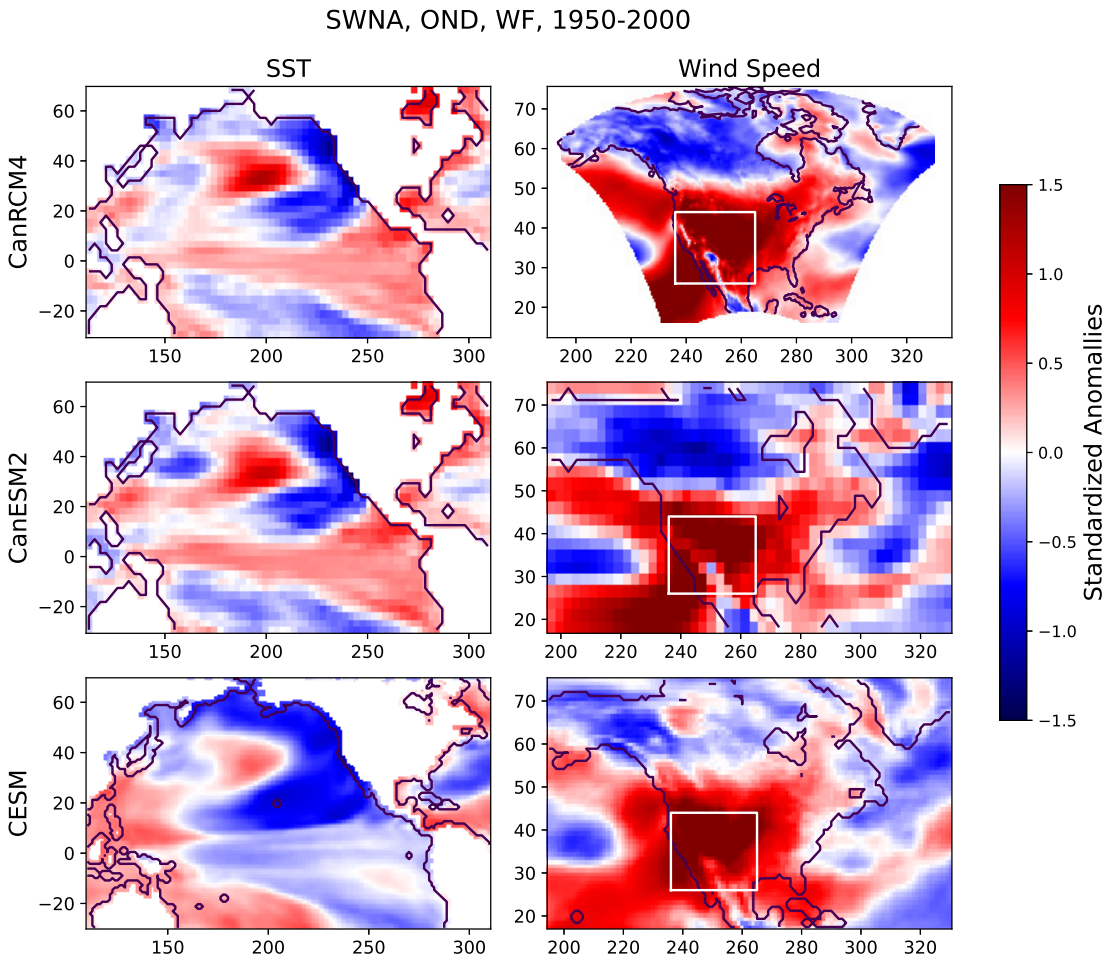

Figure A.28: OND mean of standardized anomaly of Sea Surface Temperature and surface wind speed in SWNA for WF events, in 1950-2000. First row: CanRCM4 , second row: CanESM2, third row: CESM.

A.2.2 SCNA

1. JFM

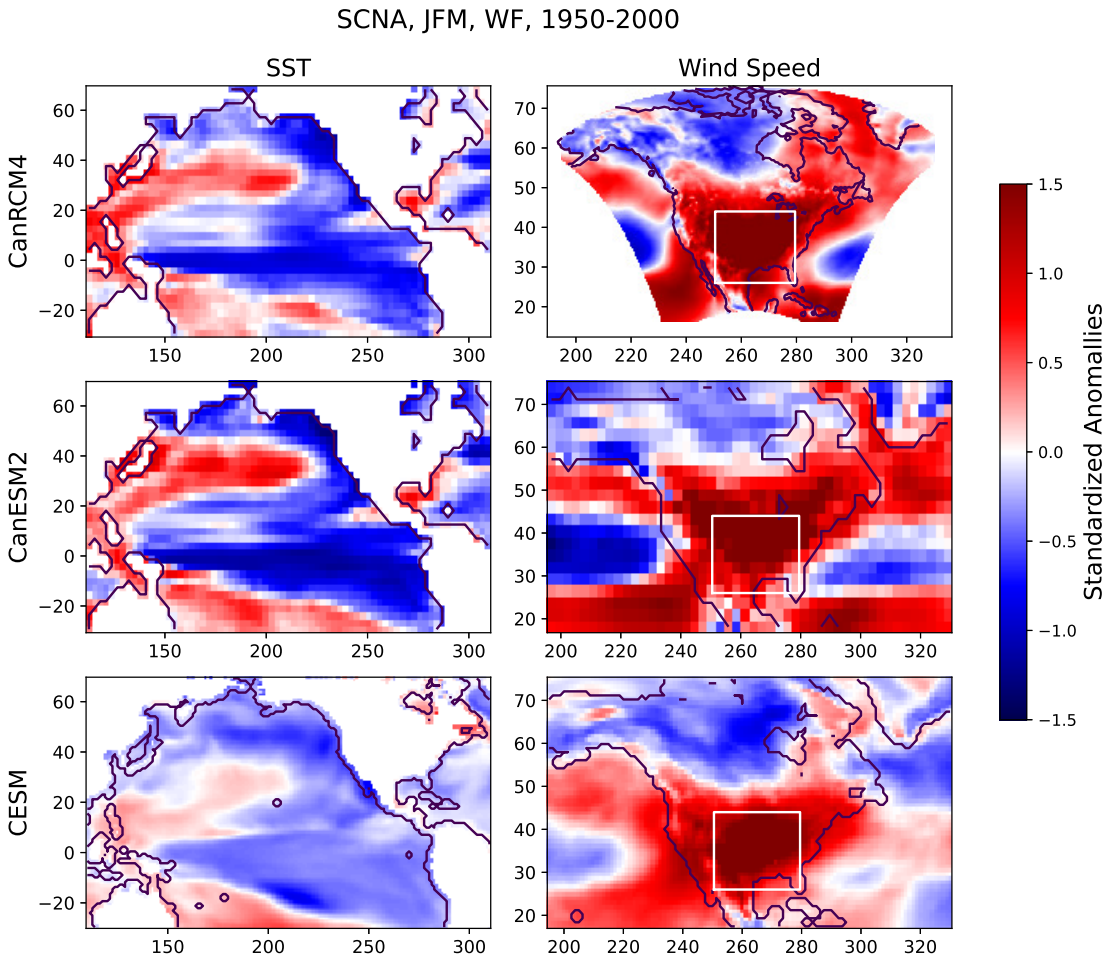

Figure A.29: JFM mean of standardized anomaly of Sea Surface Temperature and surface wind speed in SCNA for WF events, in 1950-2000. First row: CanRCM4 , second row: CanESM2, third row: CESM.

2. AMJ

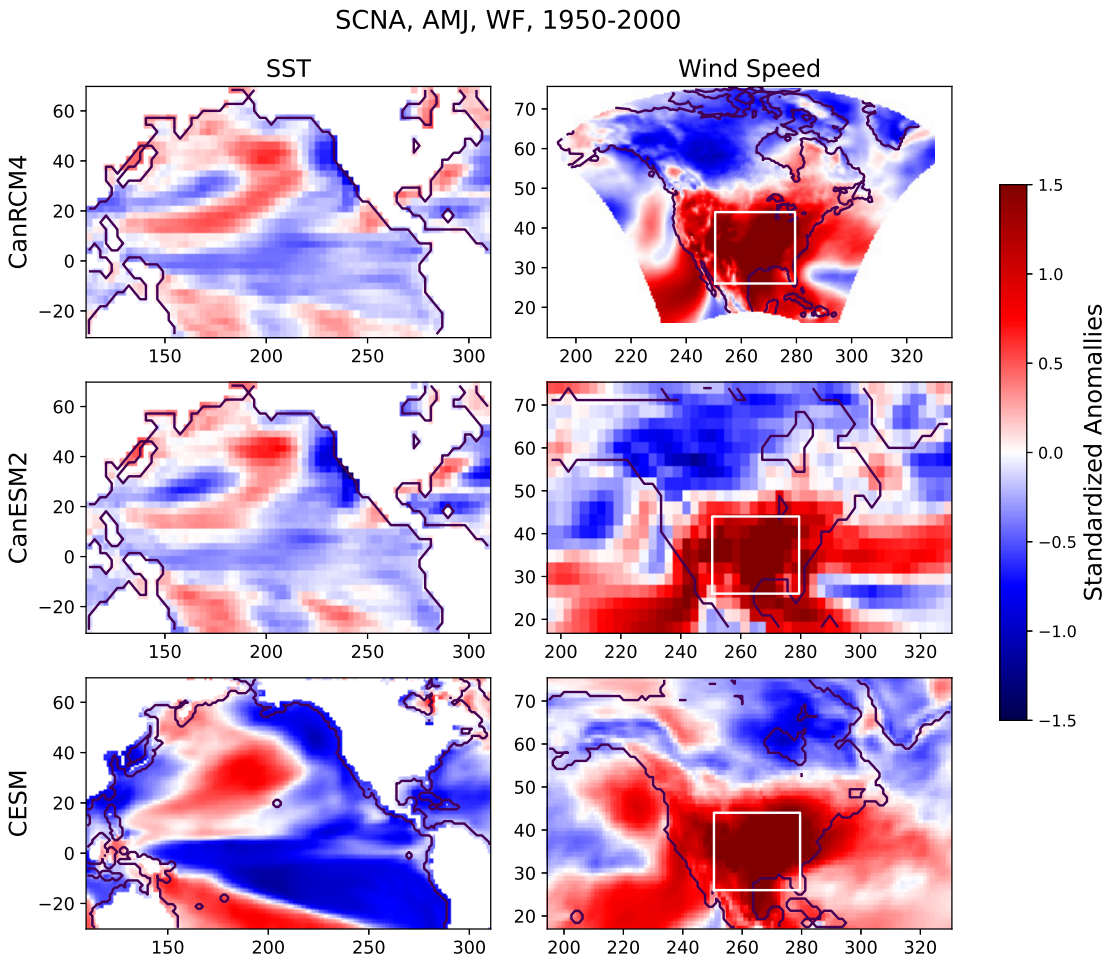

Figure A.30: AMJ mean of standardized anomaly of Sea Surface Temperature and surface wind speed in SCNA for WF events, in 1950-2000. First row: CanRCM4 , second row: CanESM2, third row: CESM.

3. JAS

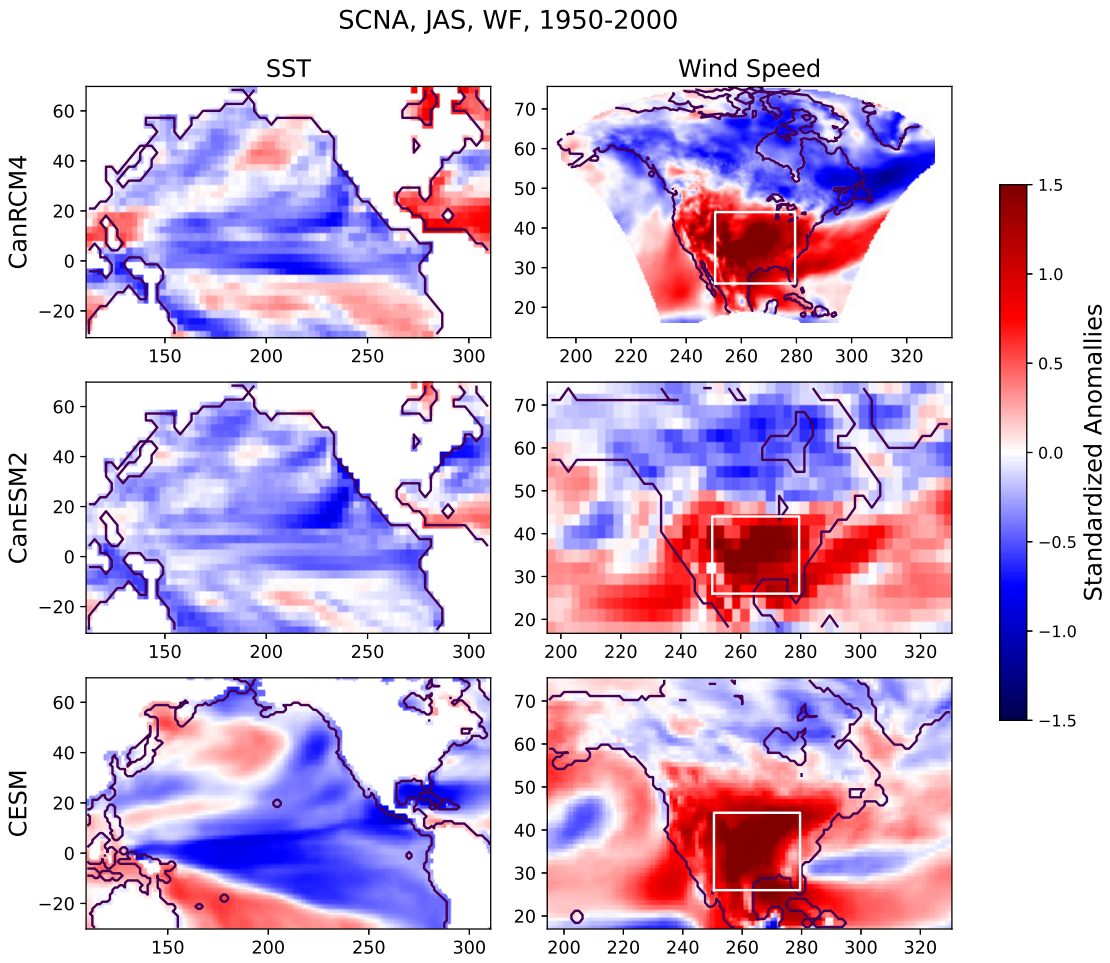

Figure A.31: JAS mean of standardized anomaly of Sea Surface Temperature and surface wind speed in SCNA for WF events, in 1950-2000. First row: CanRCM4 , second row: CanESM2, third row: CESM.

4. OND

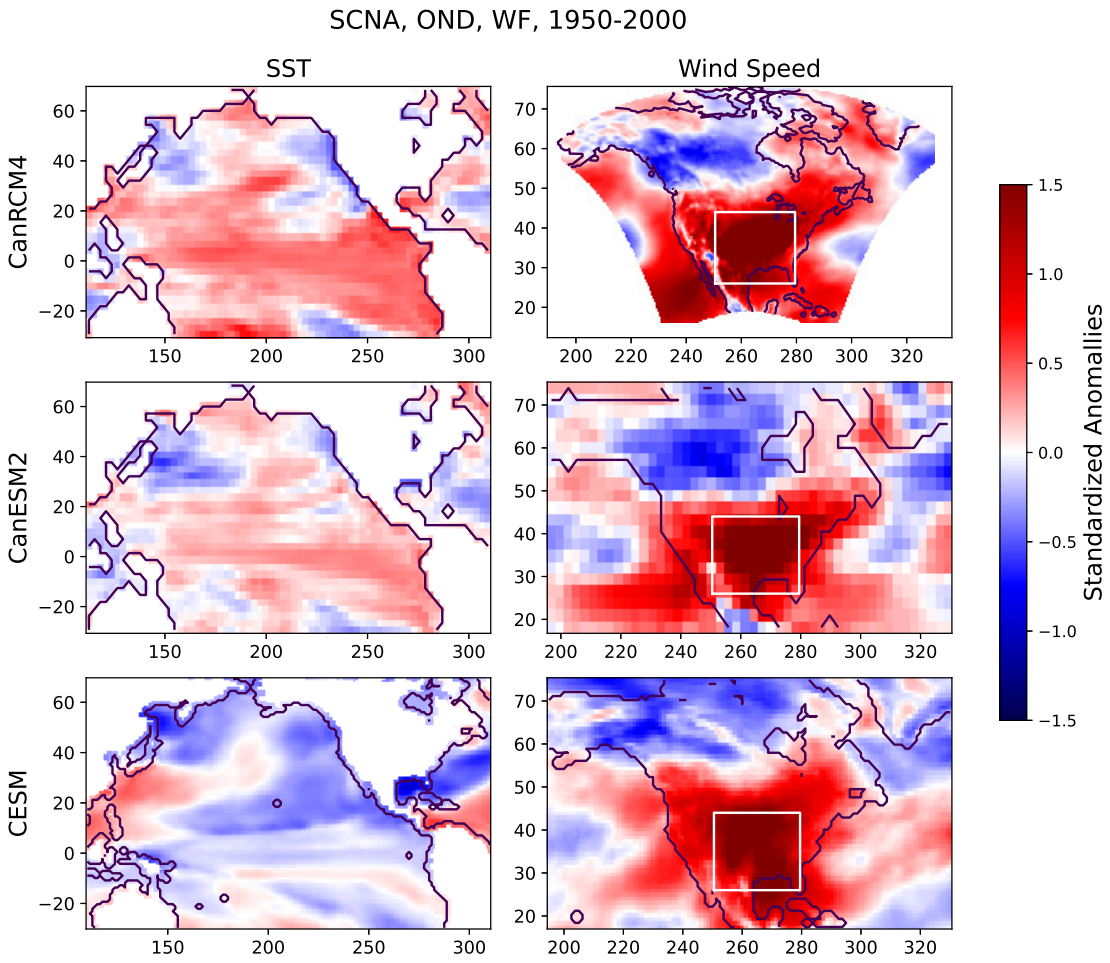

Figure A.32: OND mean of standardized anomaly of Sea Surface Temperature and surface wind speed in SCNA for WF events, in 1950-2000. First row: CanRCM4 , second row: CanESM2, third row: CESM.

A.2.3 SENA

1. JFM

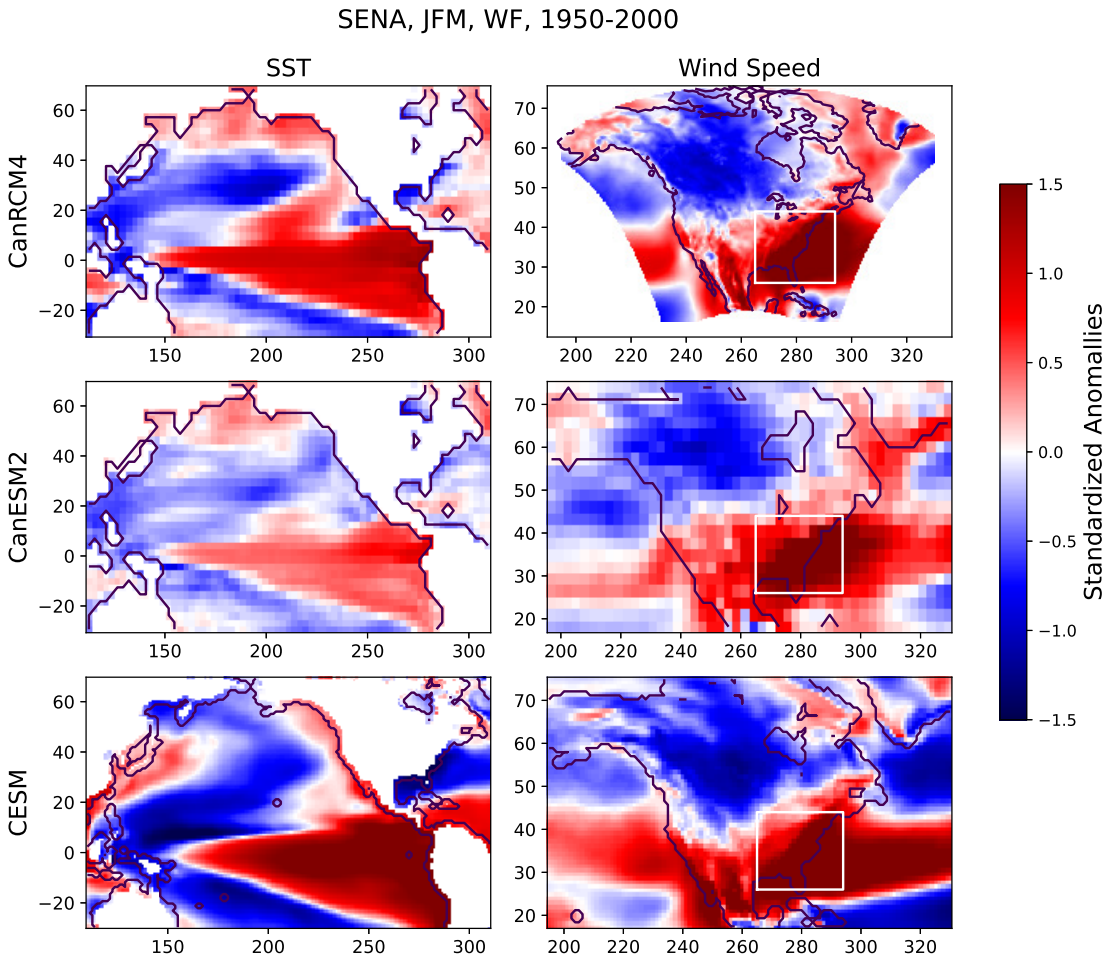

Figure A.33: JFM mean of standardized anomaly of Sea Surface Temperature and surface wind speed in SENA for WF events, in 1950-2000. First row: CanRCM4 , second row: CanESM2, third row: CESM.

2. AMJ

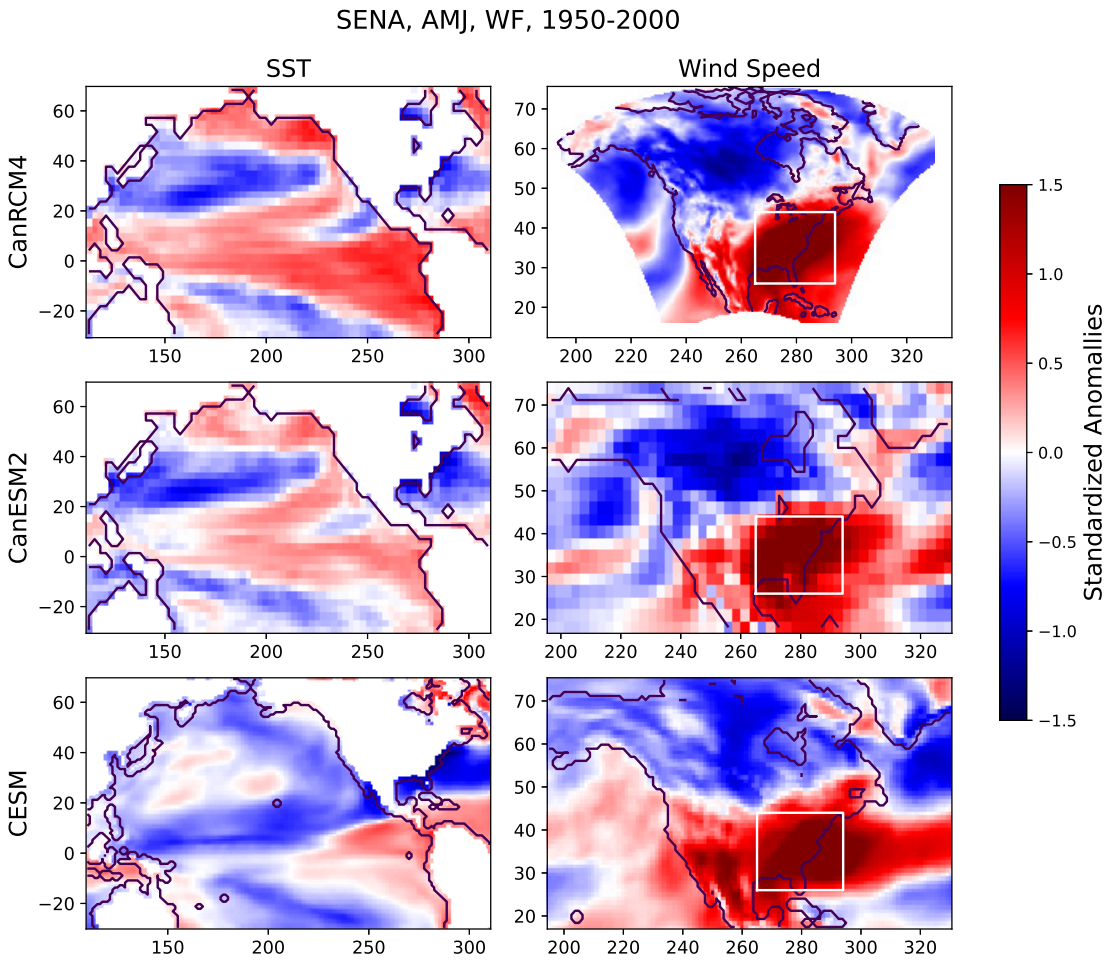

Figure A.34: AMJ mean of standardized anomaly of Sea Surface Temperature and surface wind speed in SENA for WF events, in 1950-2000. First row: CanRCM4 , second row: CanESM2, third row: CESM.

3. JAS

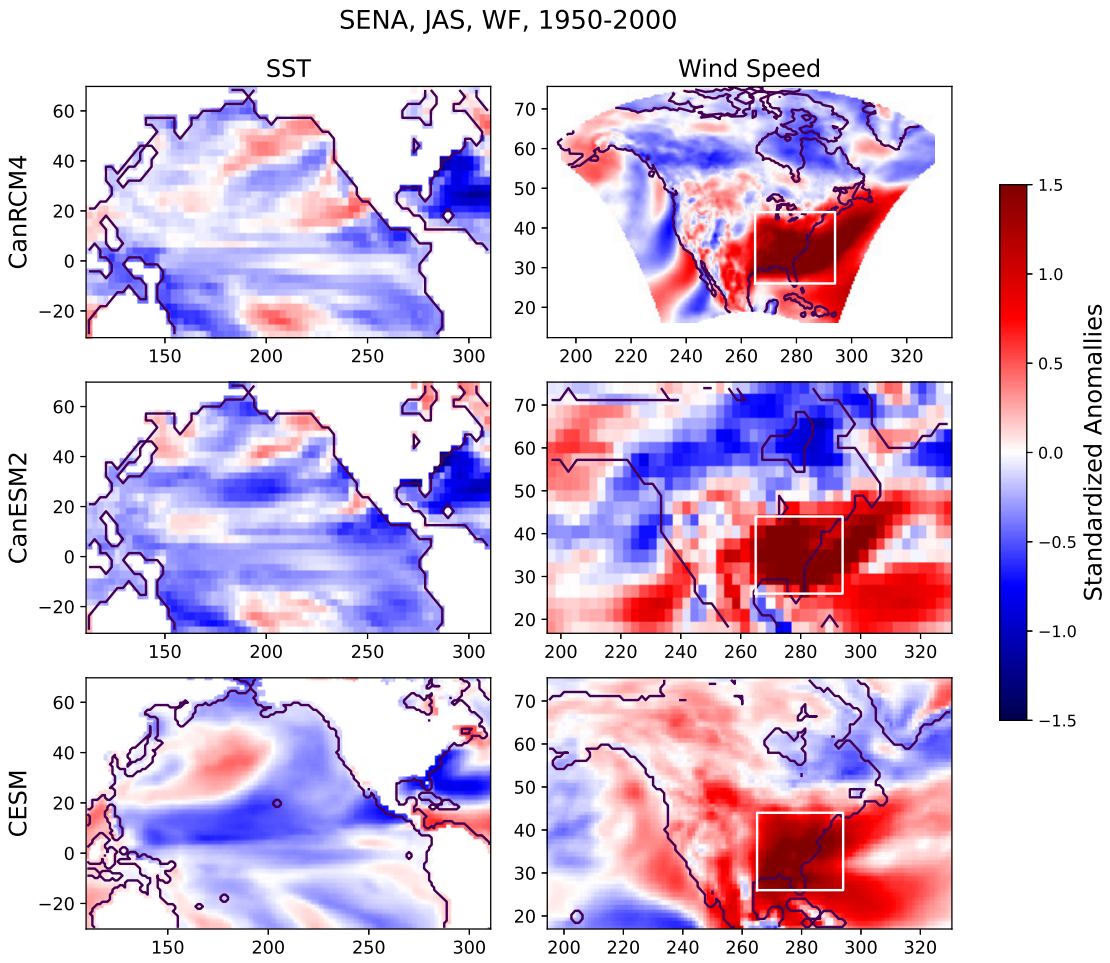

Figure A.35: JAS mean of standardized anomaly of Sea Surface Temperature and surface wind speed in SENA for WF events, in 1950-2000. First row: CanRCM4 , second row: CanESM2, third row: CESM.

4. OND

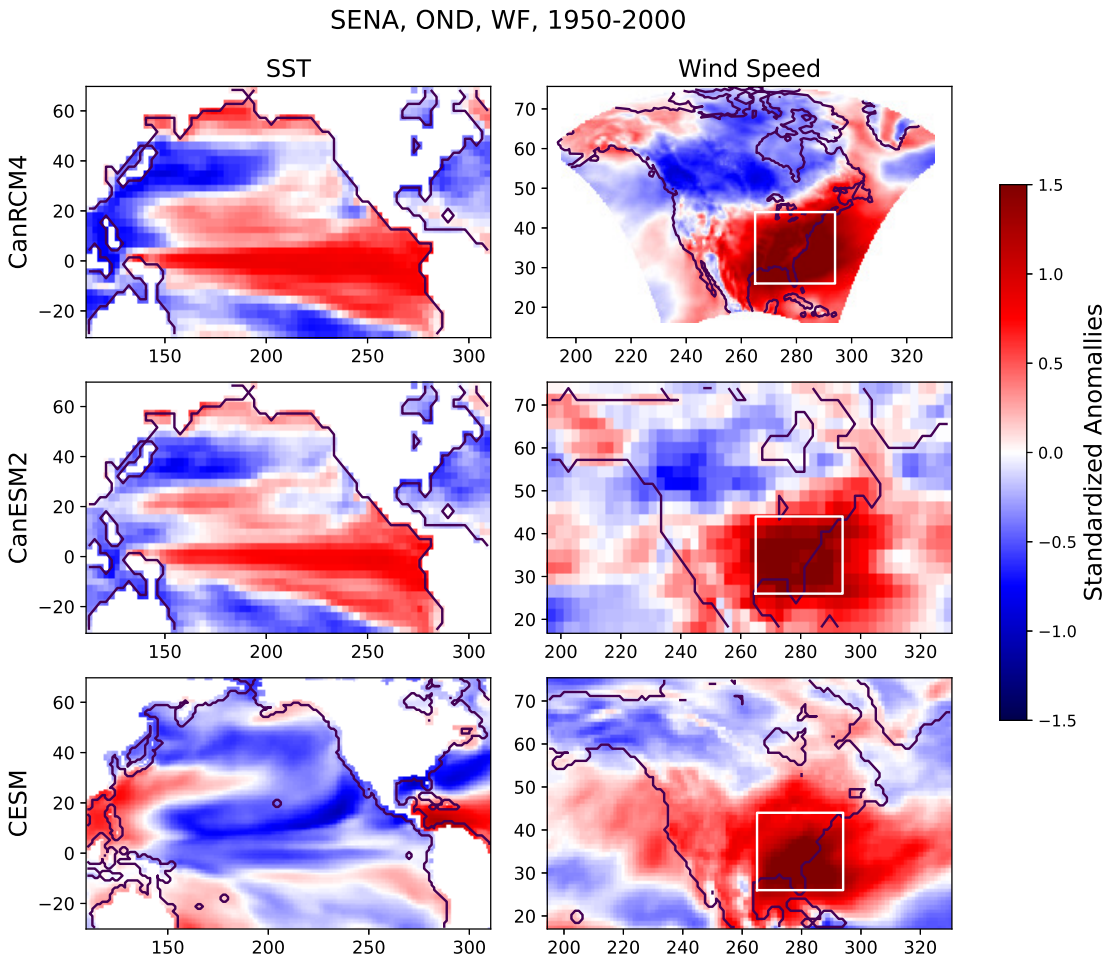

Figure A.36: OND mean of standardized anomaly of Sea Surface Temperature and surface wind speed in SENA for WF events, in 1950-2000. First row: CanRCM4 , second row: CanESM2, third row: CESM.

A.2.4 NWNA

1. JFM

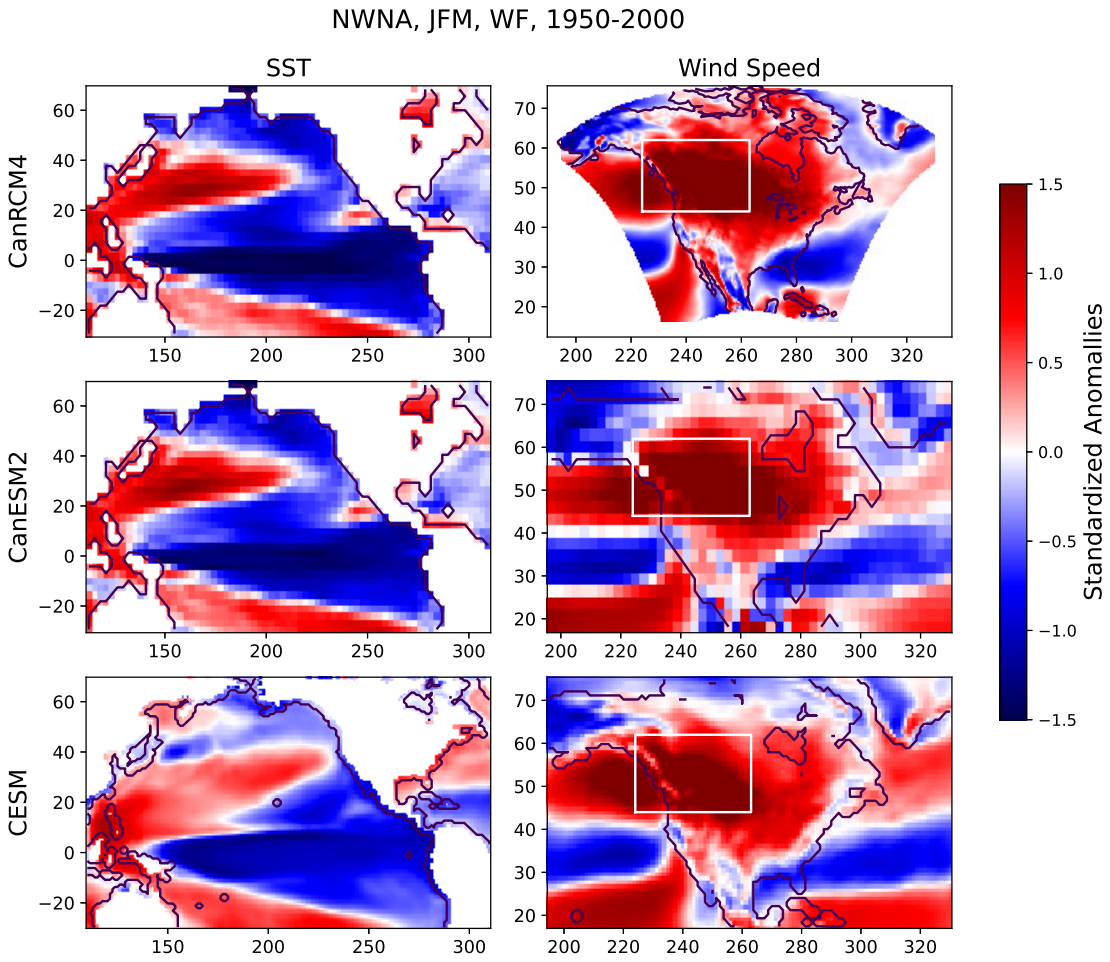

Figure A.37: JFM mean of standardized anomaly of Sea Surface Temperature and surface wind speed in NWNA for WF events, in 1950-2000. First row: CanRCM4 , second row: CanESM2, third row: CESM.

2. AMJ

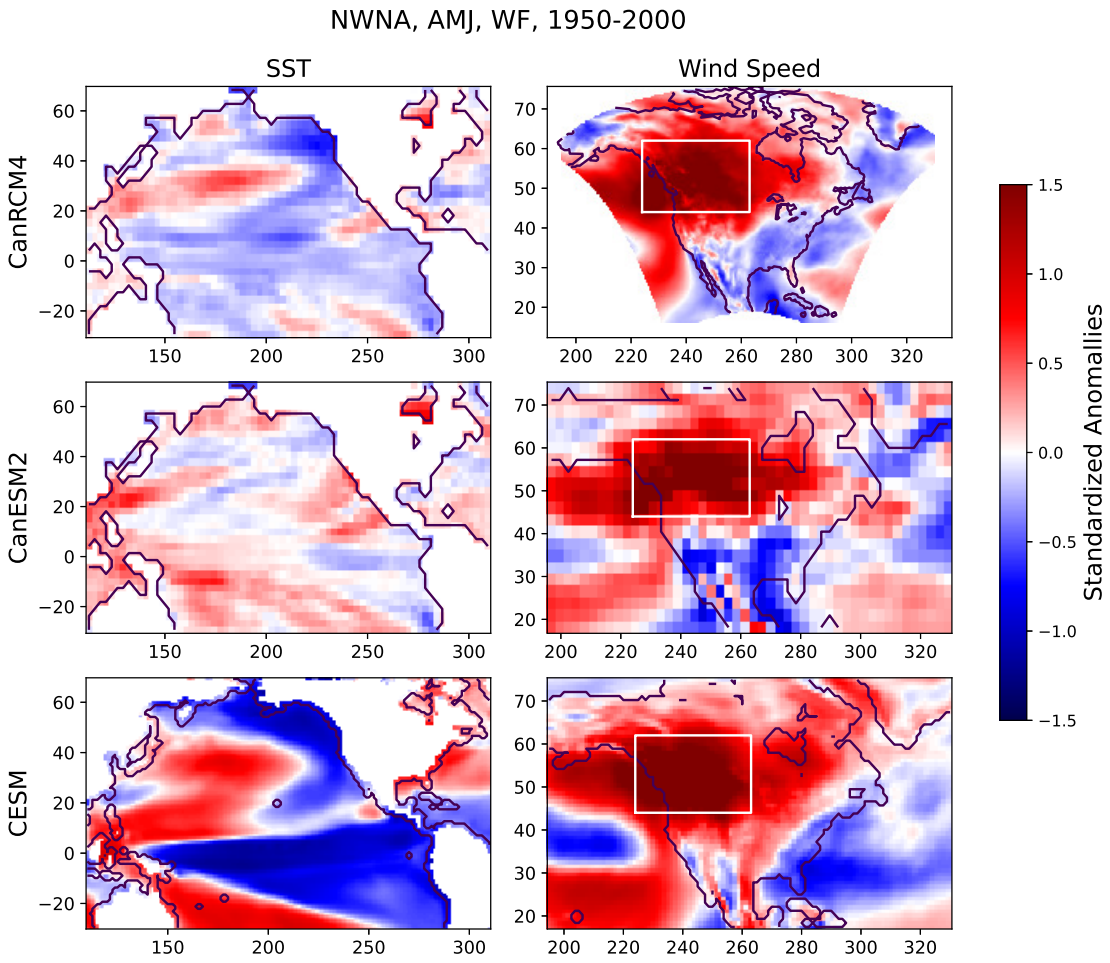

Figure A.38: AMJ mean of standardized anomaly of Sea Surface Temperature and surface wind speed in NWNA for WF events, in 1950-2000. First row: CanRCM4 , second row: CanESM2, third row: CESM.

3. JAS

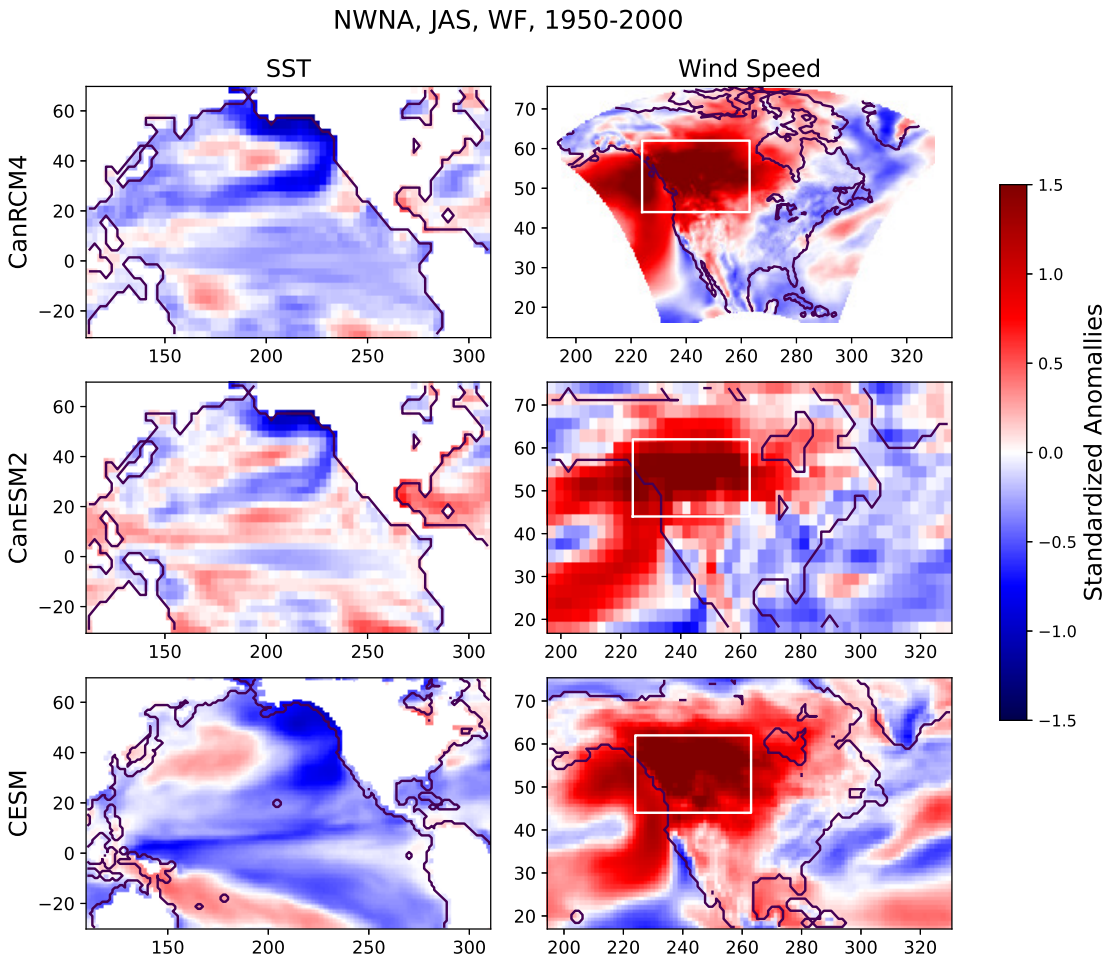

Figure A.39: JAS mean of standardized anomaly of Sea Surface Temperature and surface wind speed in NWNA for WF events, in 1950-2000. First row: CanRCM4 , second row: CanESM2, third row: CESM.

4. OND

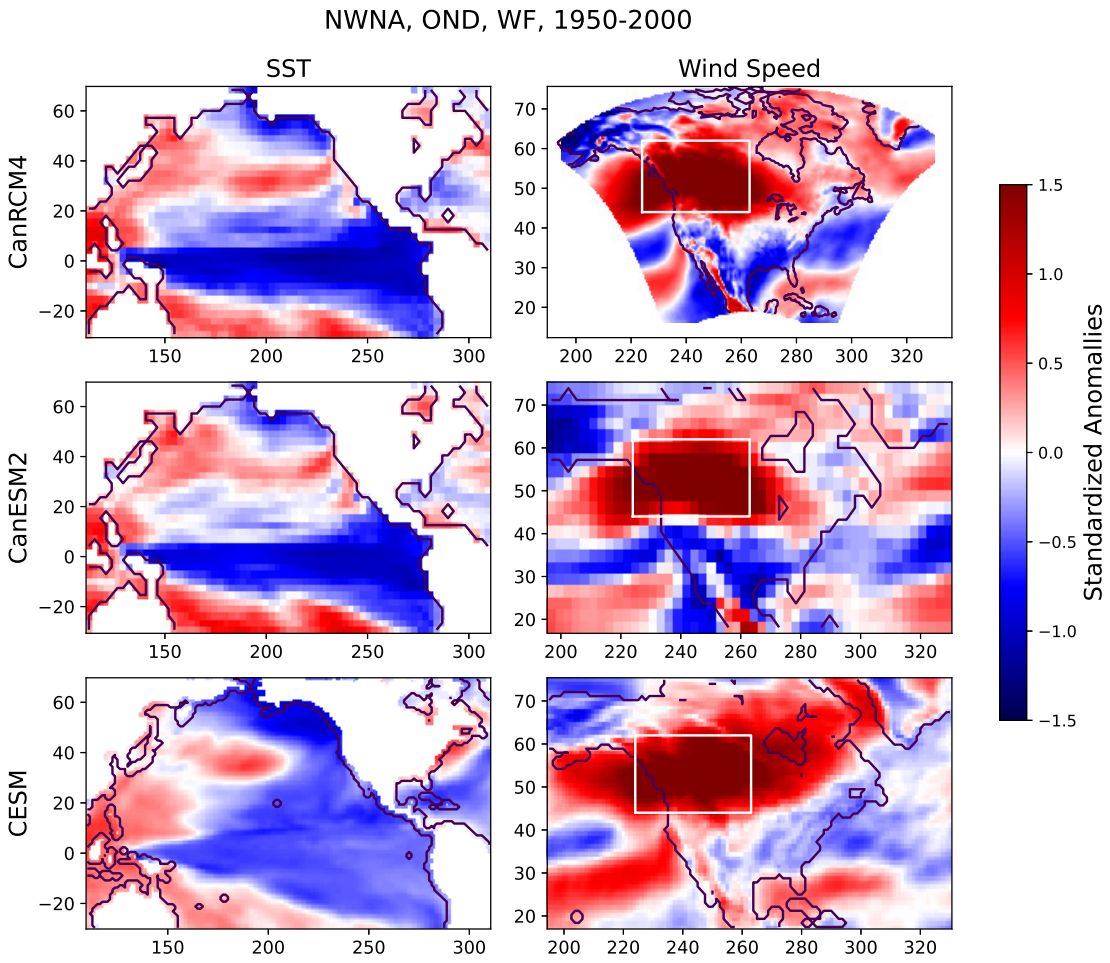

Figure A.40: OND mean of standardized anomaly of Sea Surface Temperature and surface wind speed in NWNA for WF events, in 1950-2000. First row: CanRCM4 , second row: CanESM2, third row: CESM.

A.2.5 NCNA

1. JFM

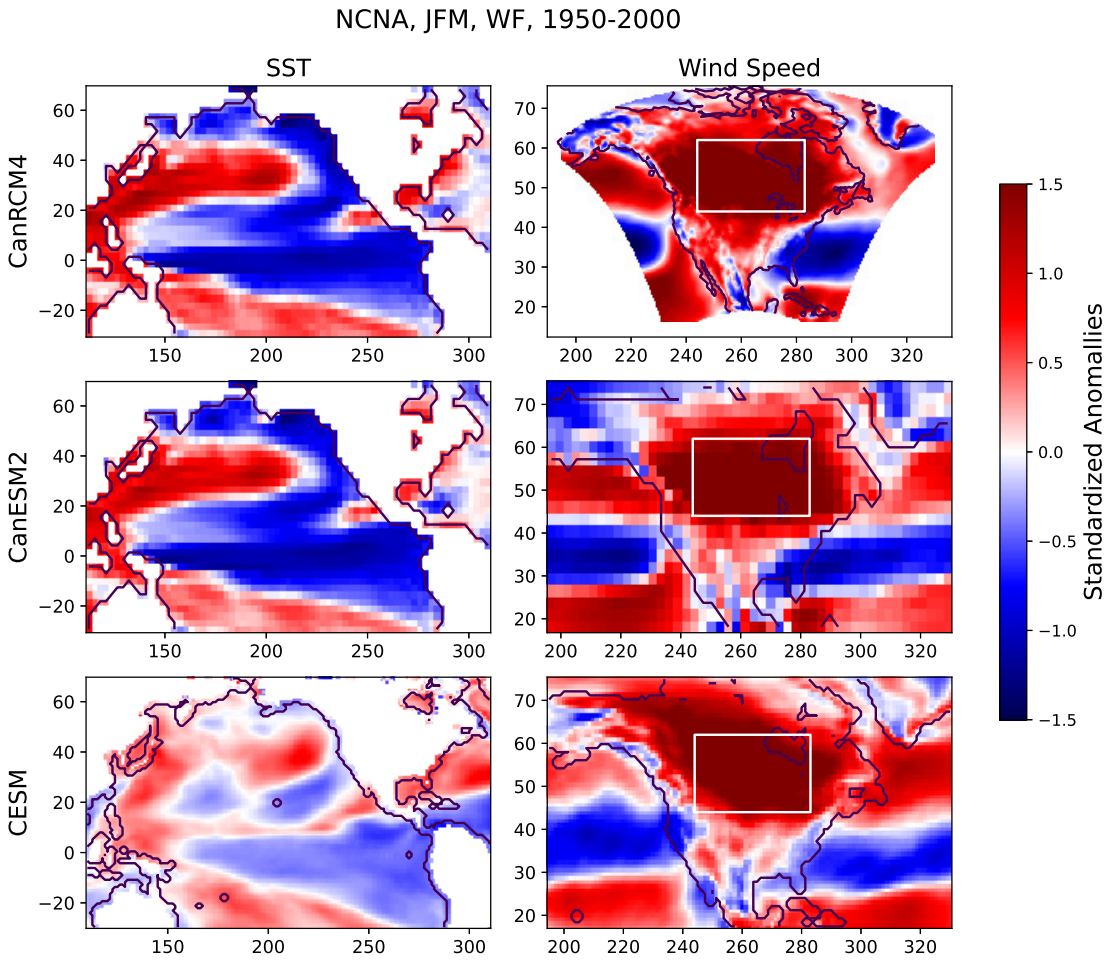

Figure A.41: JFM mean of standardized anomaly of Sea Surface Temperature and surface wind speed in NCNA for WF events, in 1950-2000. First row: CanRCM4 , second row: CanESM2, third row: CESM.

2. AMJ

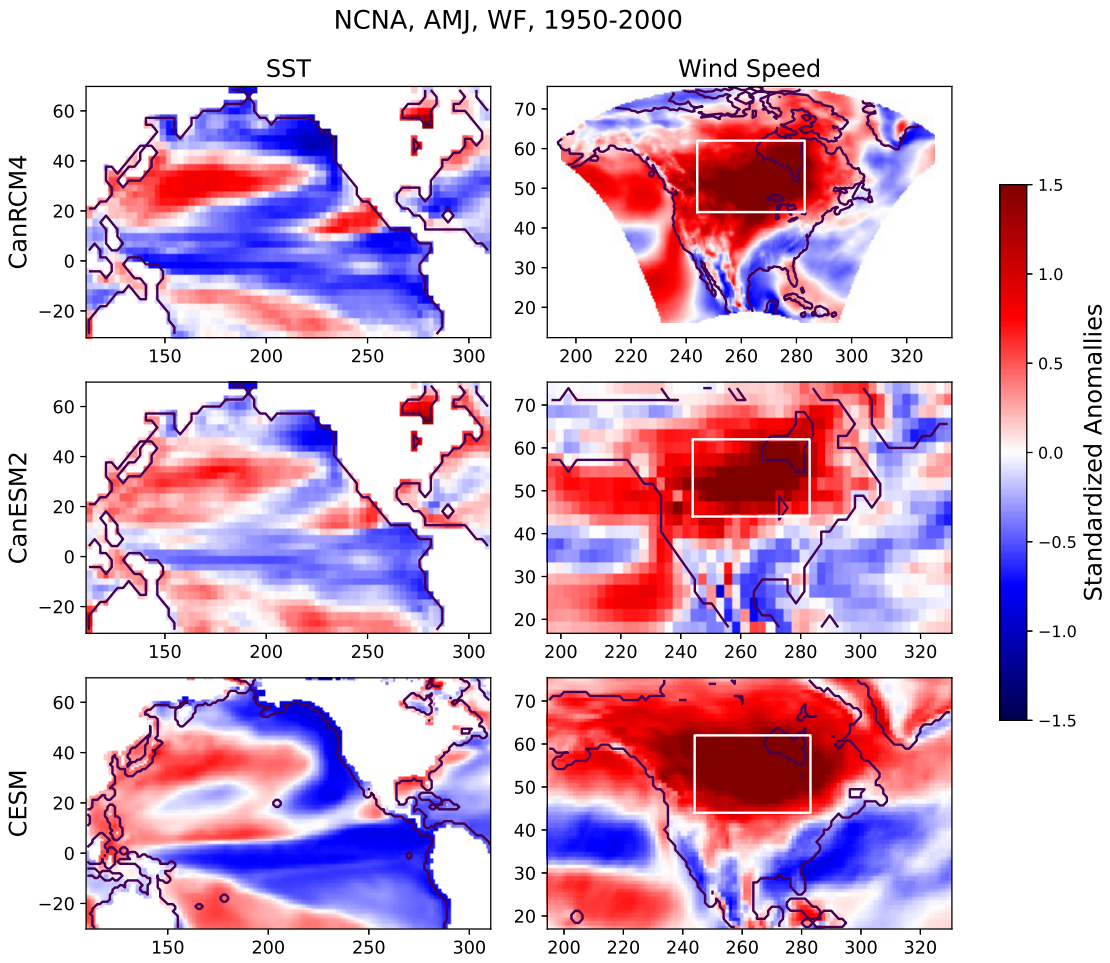

Figure A.42: AMJ mean of standardized anomaly of Sea Surface Temperature and surface wind speed in NCNA for WF events, in 1950-2000. First row: CanRCM4 , second row: CanESM2, third row: CESM.

3. JAS

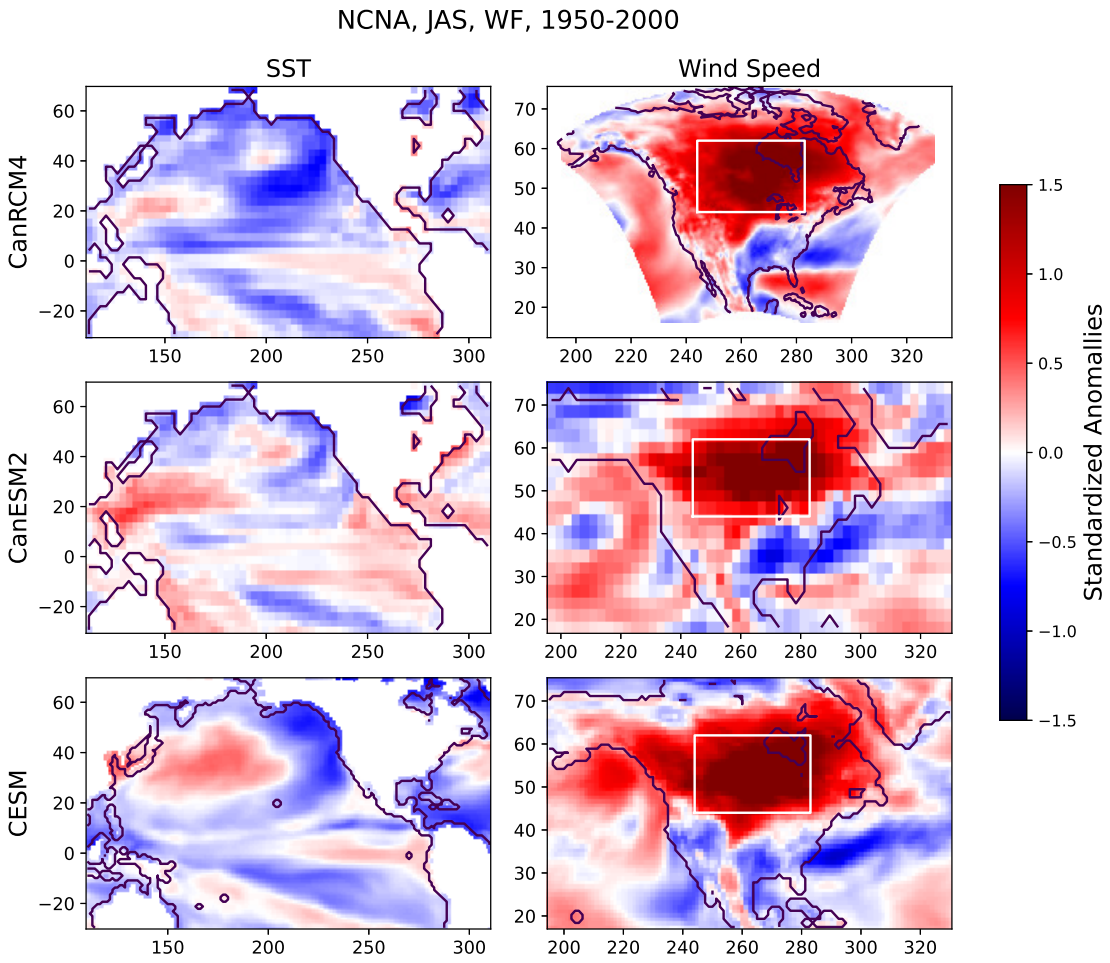

Figure A.43: JAS mean of standardized anomaly of Sea Surface Temperature and surface wind speed in NCNA for WF events, in 1950-2000. First row: CanRCM4 , second row: CanESM2, third row: CESM.

4. OND

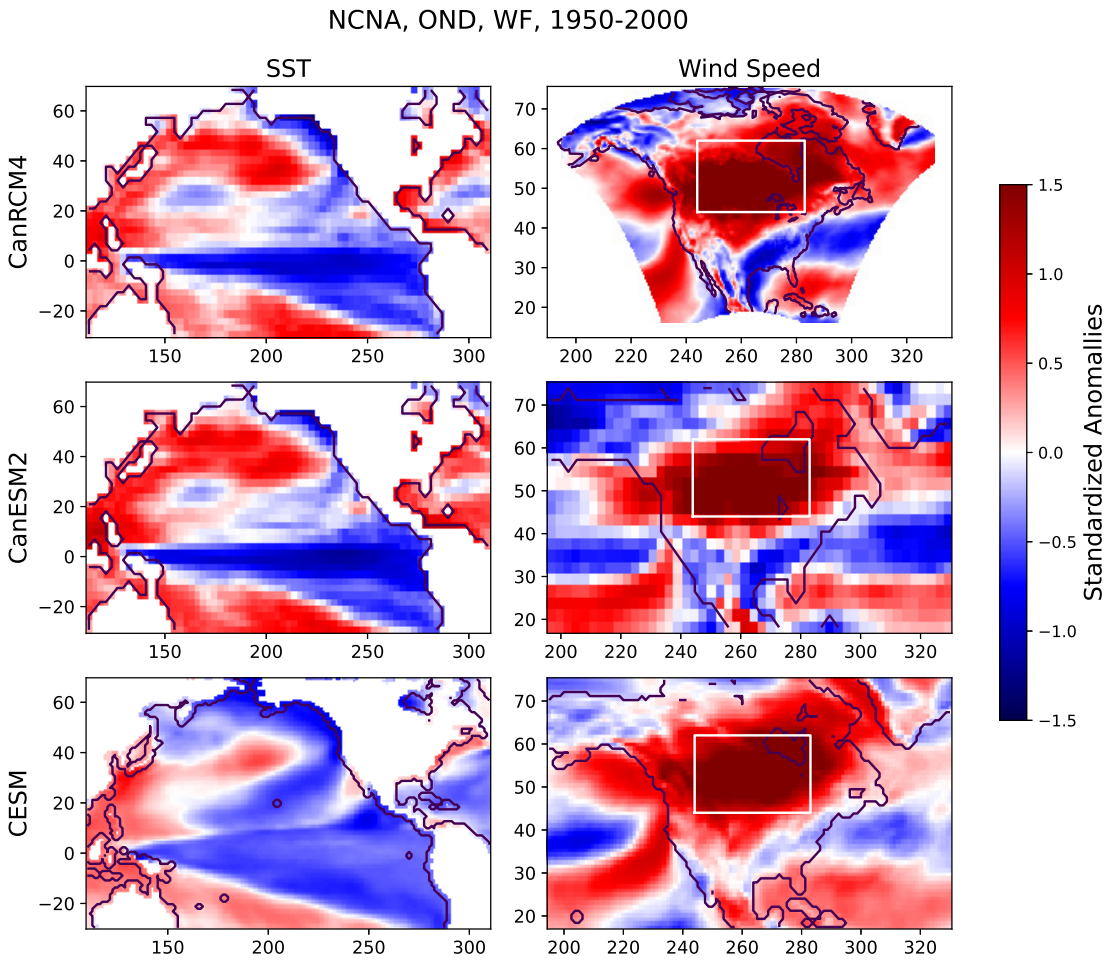

Figure A.44: OND mean of standardized anomaly of Sea Surface Temperature and surface wind speed in NCNA for WF events, in 1950-2000. First row: CanRCM4 , second row: CanESM2, third row: CESM.

A.2.6 NENA

1. JFM

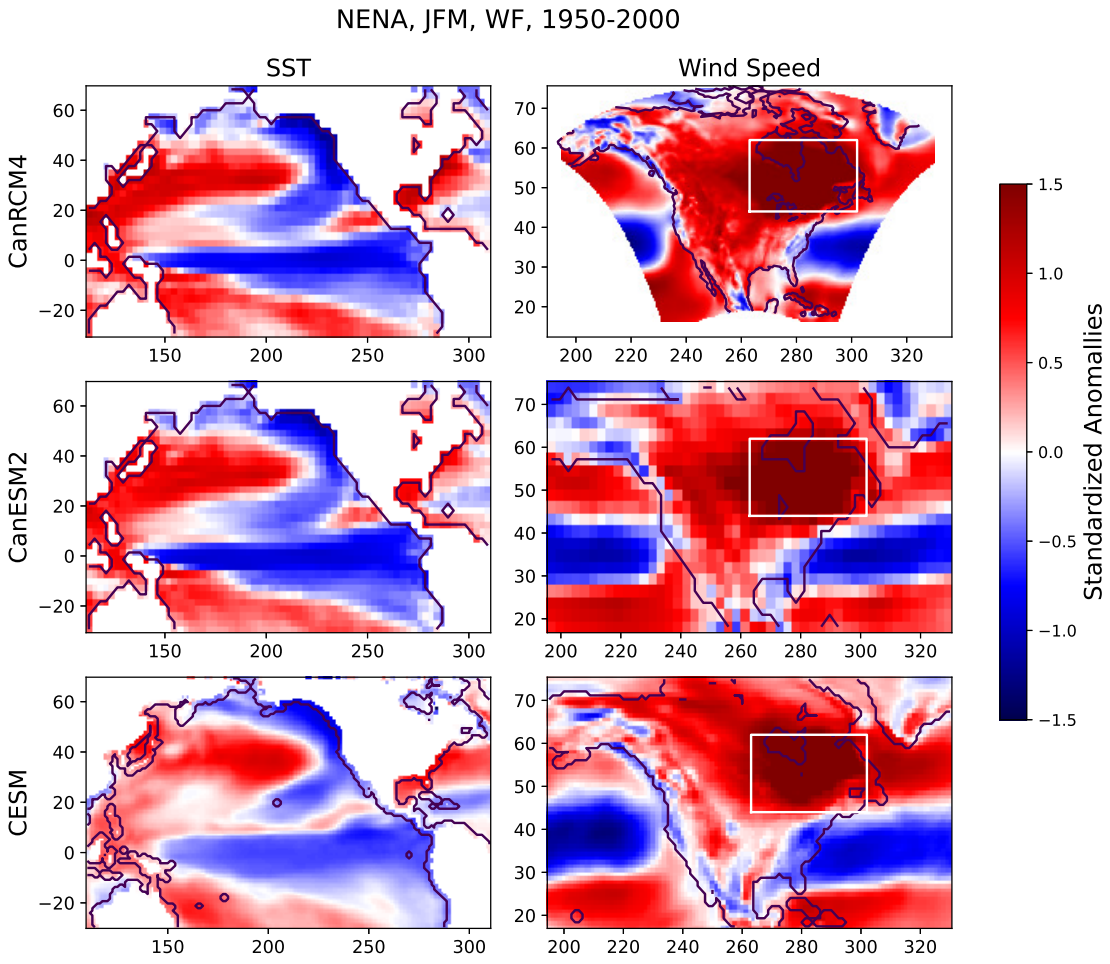

Figure A.45: JFM mean of standardized anomaly of Sea Surface Temperature and surface wind speed in NENA for WF events, in 1950-2000. First row: CanRCM4 , second row: CanESM2, third row: CESM.

2. AMJ

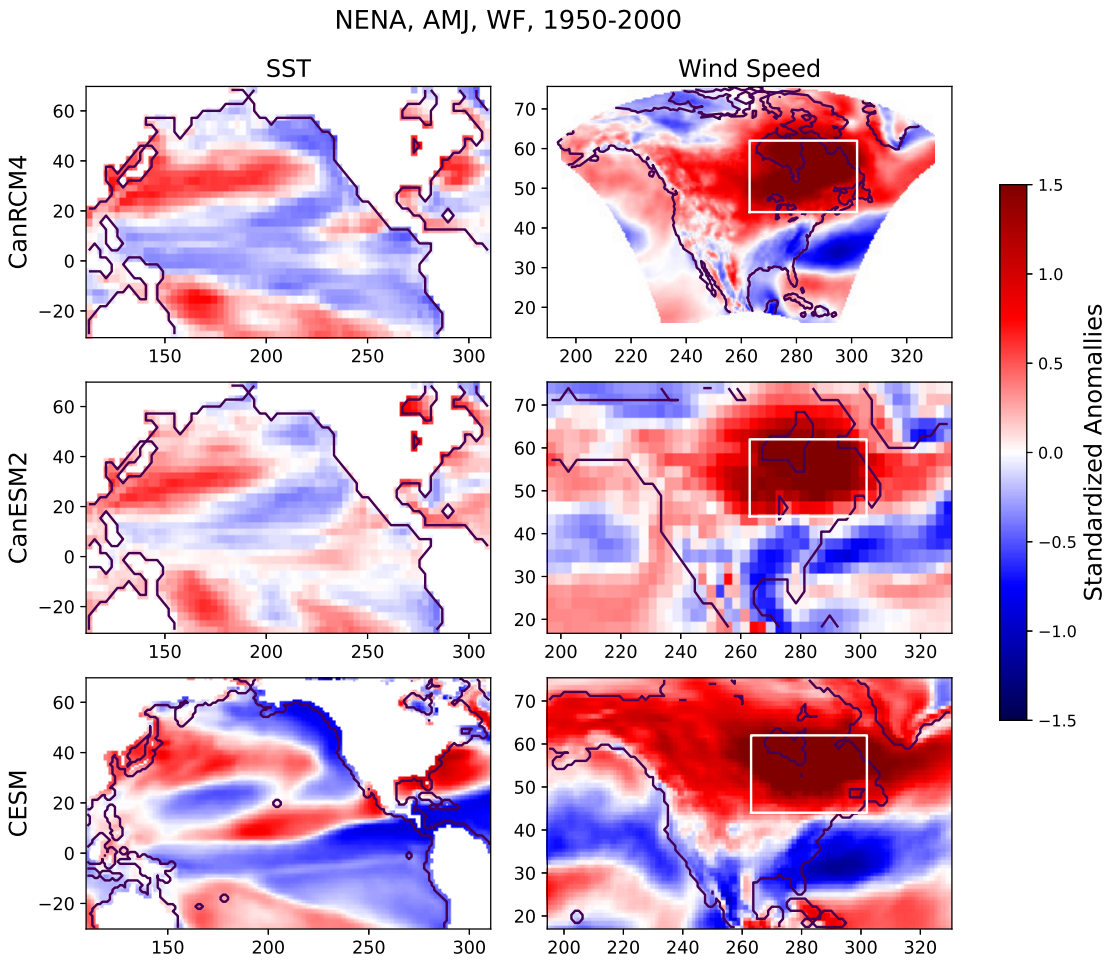

Figure A.46: AMJ mean of standardized anomaly of Sea Surface Temperature and surface wind speed in NENA for WF events, in 1950-2000. First row: CanRCM4 , second row: CanESM2, third row: CESM.

3. JAS

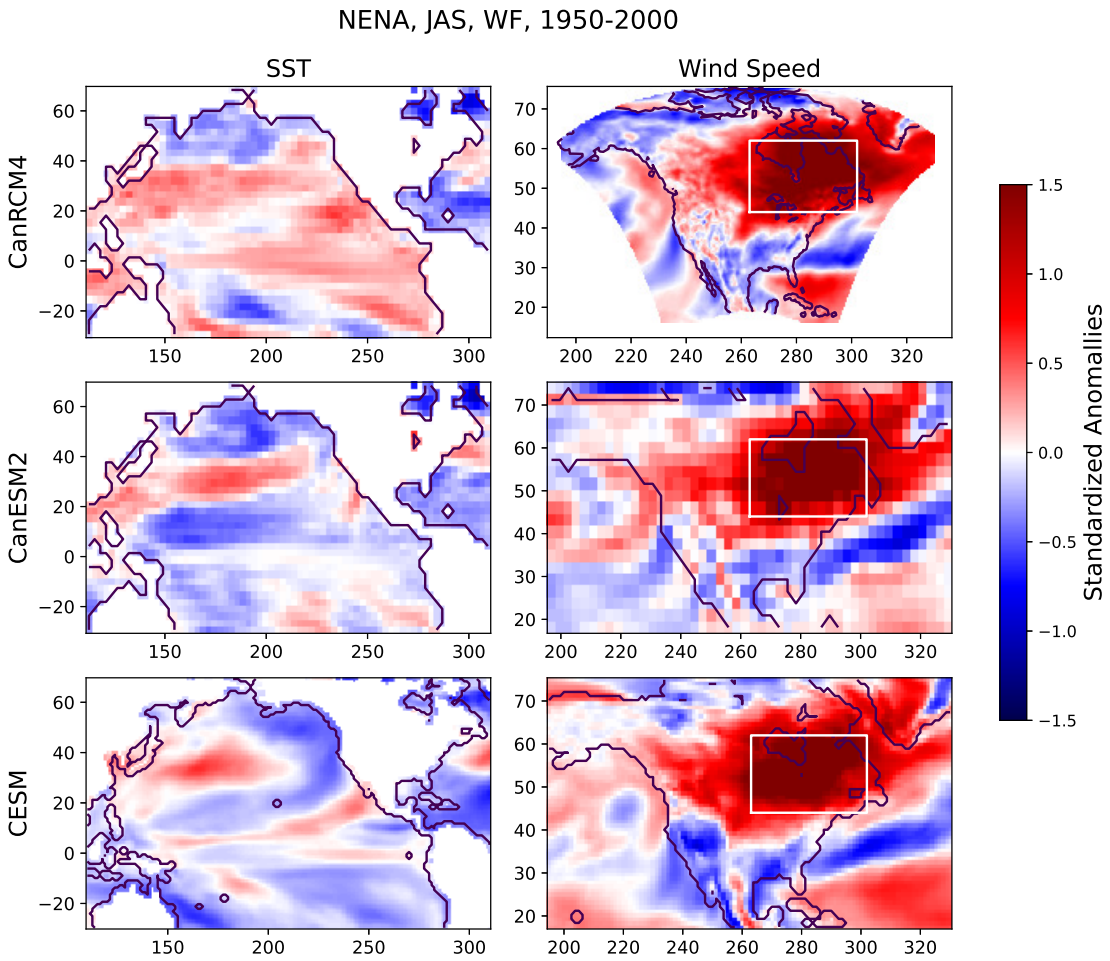

Figure A.47: JAS mean of standardized anomaly of Sea Surface Temperature and surface wind speed in NENA for WF events, in 1950-2000. First row: CanRCM4 , second row: CanESM2, third row: CESM.

4. OND

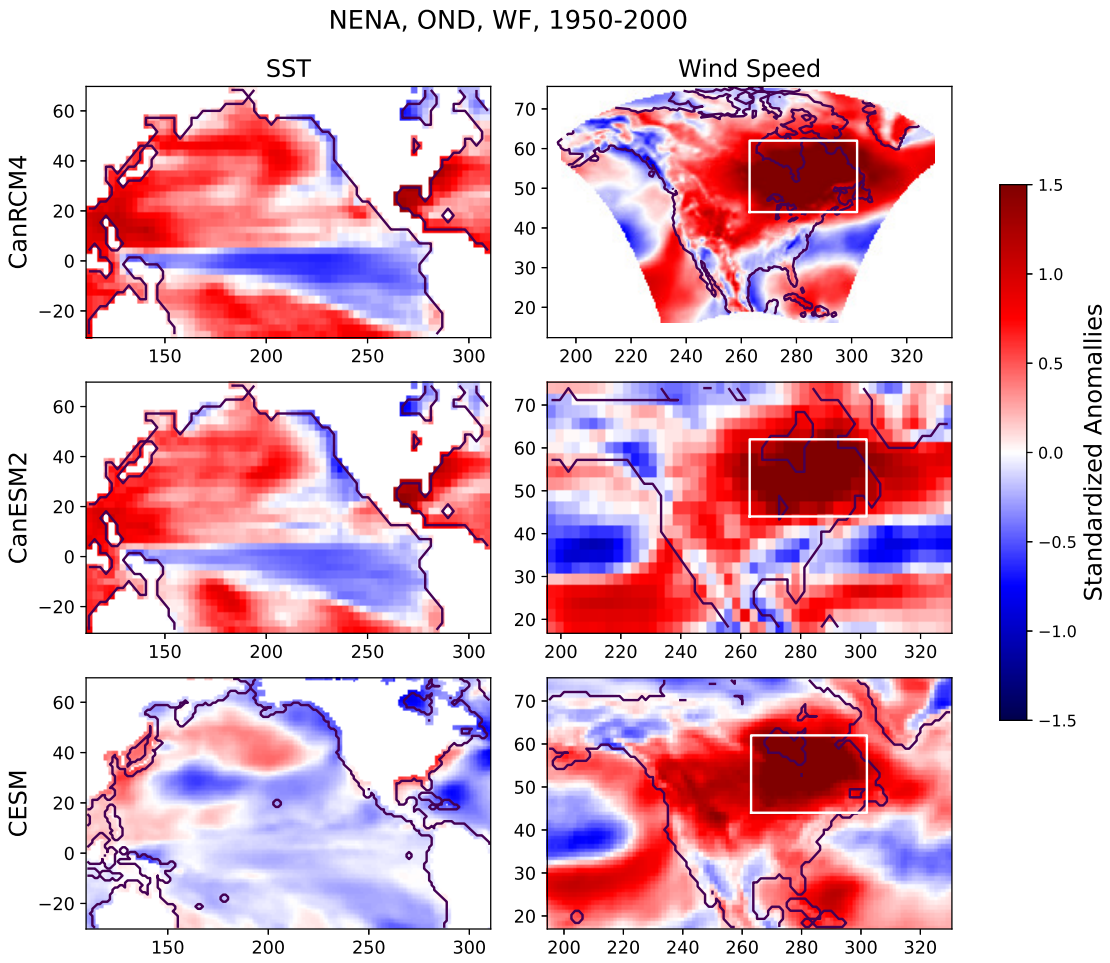

Figure A.48: OND mean of standardized anomaly of Sea Surface Temperature and surface wind speed in NENA for WF events, in 1950-2000. First row: CanRCM4 , second row: CanESM2, third row: CESM.

Appendix B

Additional Figures

B.0.1 Wind Drought Predictability

1. North Pacific

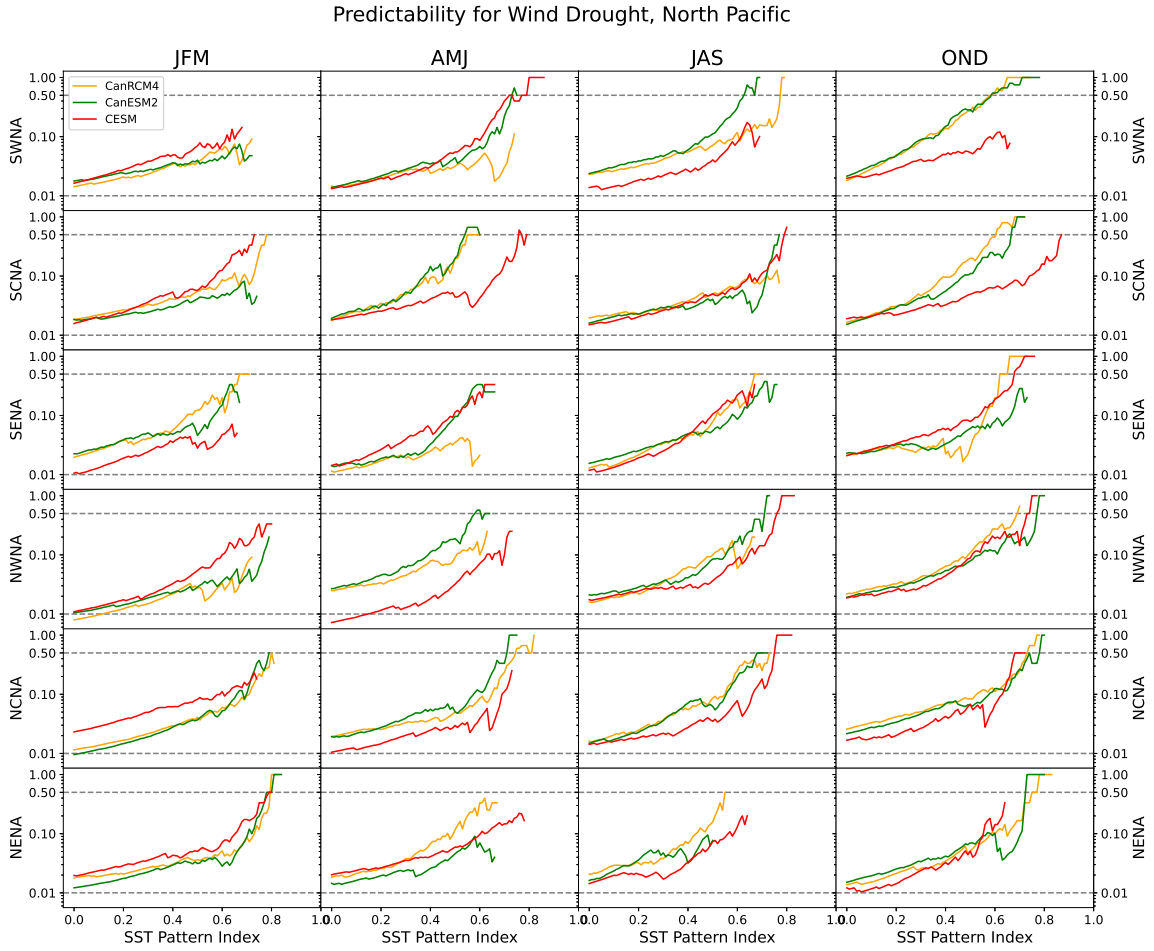

Figure B.1: Conditional Probability of Wind Drought events as a function of the North Pacific SST Pattern Index, in North American regions (rows) and seasons (columns) in 1950-2000; orange color represents the results of CanRCM4, green, CanESM2, and red, CESM.

2. Equatorial Pacific

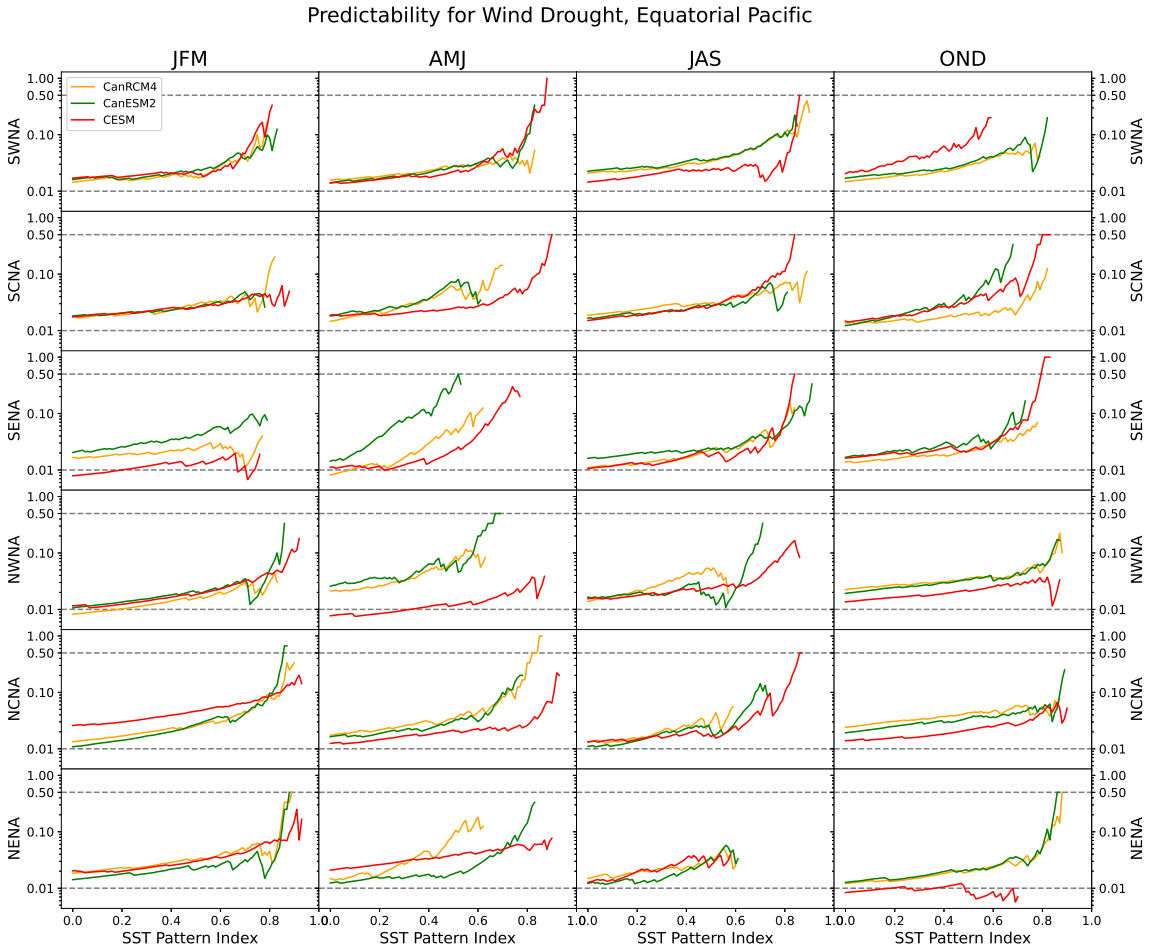

Figure B.2: Conditional Probability of Wind Drought events as a function of the Equatorial Pacific SST Pattern Index, in North American regions (rows) and seasons (columns) in 1950-2000; orange color represents the results of CanRCM4, green, CanESM2, and red, CESM.

B.0.2 Wind Flood Predictability

1. North Pacific

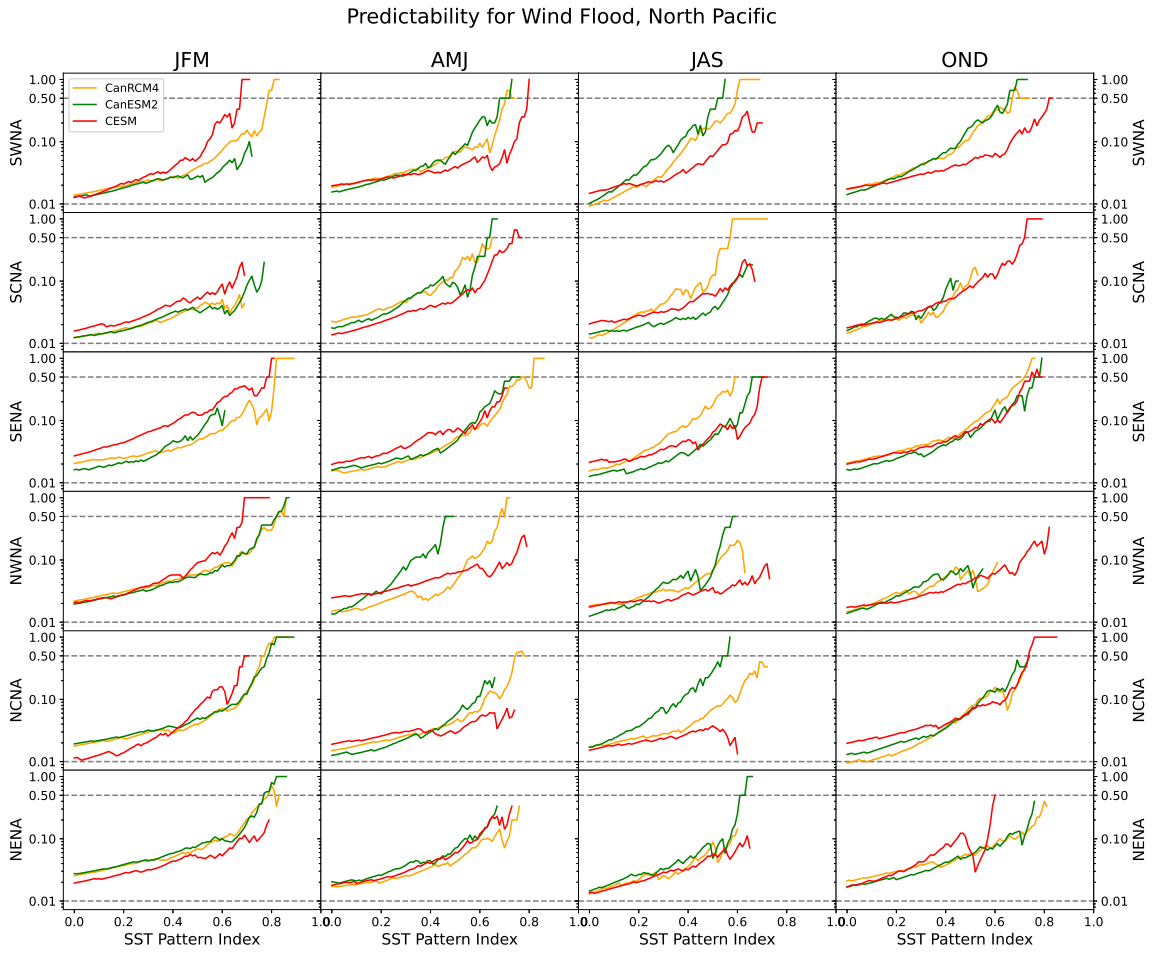

Figure B.3: Conditional Probability of Wind Flood events as a function of the North Pacific SST Pattern Index, in North American regions (rows) and seasons (columns) in 1950-2000; orange color represents the results of CanRCM4, green, CanESM2, and red, CESM.

2. Equatorial Pacific

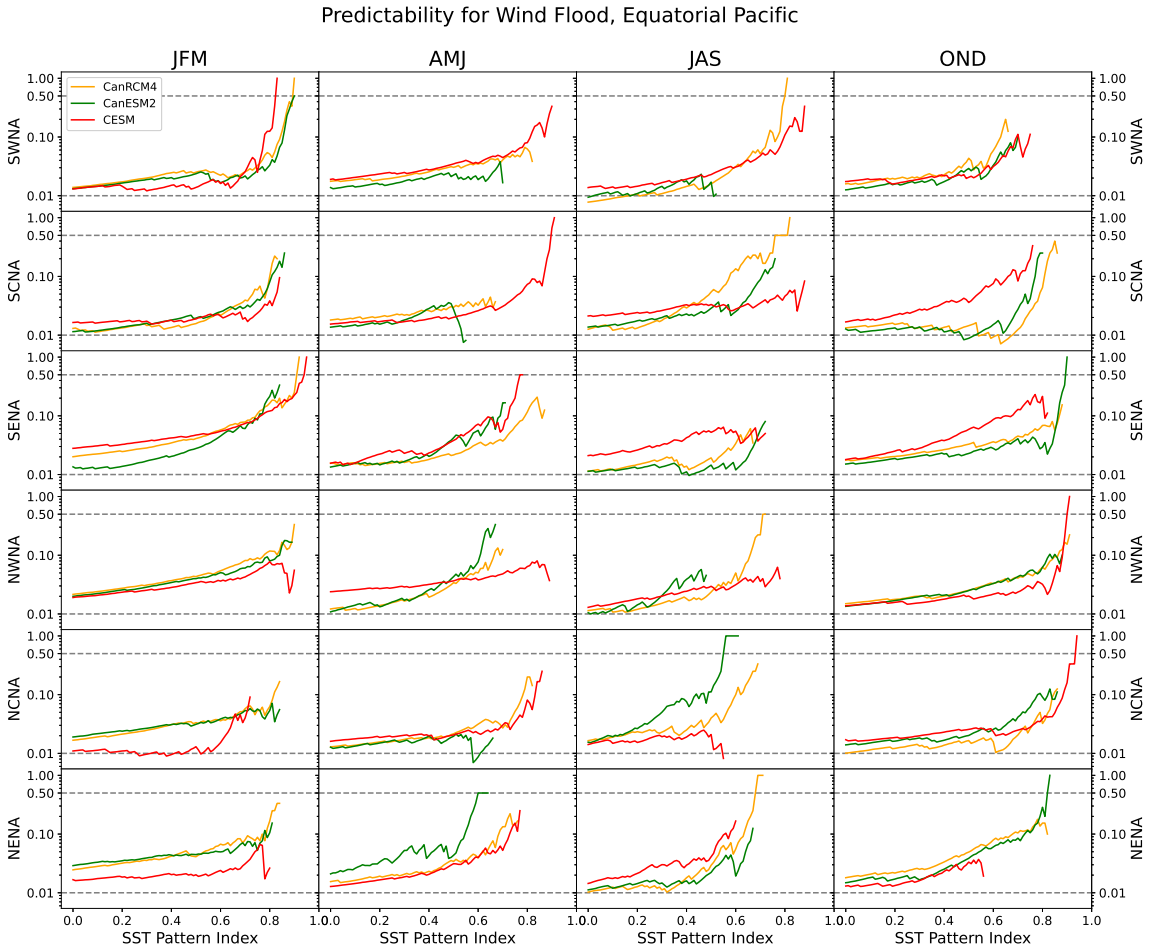

Figure B.4: Conditional Probability of Wind Flood events as a function of the Equatorial Pacific SST Pattern Index, in North American regions (rows) and seasons (columns) in 1950-2000; orange color represents the results of CanRCM4, green, CanESM2, and red, CESM.

B.0.3 Predictability of extratropical versus tropical SST domains

1. Extratropical domain

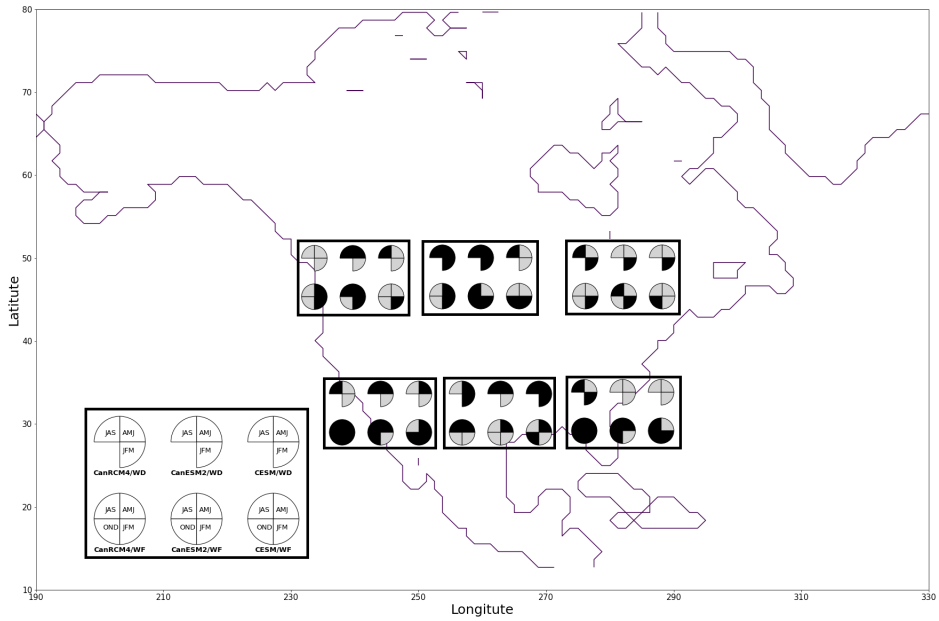

Figure B.5: Predictability summary for WD and WF events across North American regions based on extratropical (20° to 70°N, 110° to 310°E) SST. Black, grey, and white colors show different classes of predictability: "beyond a coin flip", "beyond random chance", and "not predictable". SWNA, SCNA, and SENA are displayed in the bottom row, and NWNA, NCNA, and NENA in the top row. Each region displays predictability results for three climate models (CanRCM4, CanESM2, and CESM), with each model represented by a circle divided into seasonal quarters as shown in the legend.

2. Tropical domain

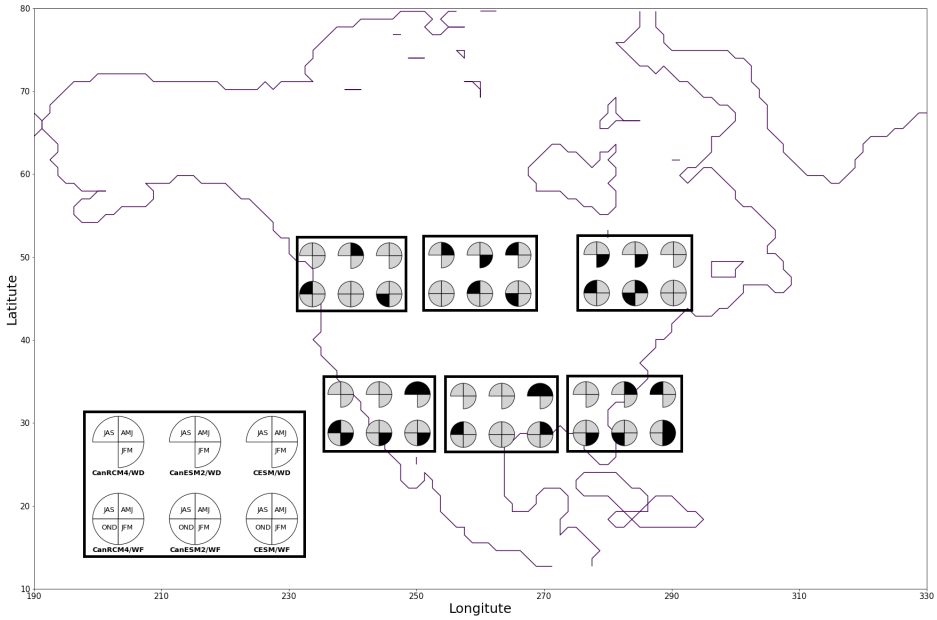

Figure B.6: Predictability summary for WD and WF events across North American regions based on tropical (-30° to 20°N, 110° to 310°E) SST. Black, grey, and white colors show different classes of predictability: "beyond a coin flip", "beyond random chance", and "not predictable". SWNA, SCNA, and SENA are displayed in the bottom row, and NWNA, NCNA, and NENA in the top row. Each region displays predictability results for three climate models (CanRCM4, CanESM2, and CESM), with each model represented by a circle divided into seasonal quarters as shown in the legend.

Bibliography

Arora, V. K., Scinocca, J. F., Boer, G. J., Christian, J. R., and Denman, K. L. (2011). Carbon emission limits required to satisfy future representative concentration pathways of greenhouse gases. *GEOPHYSICAL RESEARCH LETTERS*, 38.

Baxter, S. and Nigam, S. (2015). Key role of the north pacific Oscillation–West pacific pattern in generating the extreme 2013/14 north american winter. *Journal of Climate*, 28:8109–8117.

Bellprat, O., García-Serrano, J., Fučkar, N., Massonnet, F., Guemas, V., and Doblas-Reyes, F. (2016). The role of arctic sea ice and sea surface temperatures on the cold 2015 february over north america. *Bulletin of the American Meteorological Society*, 97(12):36–41.

Bitz, C. M. and Battisti, D. S. (1999). Interannual to decadal variability in climate and the glacier mass balance in washington, western canada, and alaska. *J. Clim.*, 12(11):3181–3196.

Cai, W., Santoso, A., Collins, M., Dewitte, B., Karamperidou, C., Kug, J.-S., Lengaigne, M., McPhaden, M. J., Stuecker, M. F., Taschetto, A. S., Timmermann, A., Wu, L., Yeh, S.-W., Wang, G., Ng, B., Jia, F., Yang, Y., Ying, J., Zheng, X.-T., Bayr, T., Brown, J. R., Capotondi, A., Cobb, K. M., Gan, B., Geng, T., Ham, Y.-G., Jin, F.-F., Jo, H.-S., Li, X., Lin, X., McGregor, S., Park, J.-H., Stein, K., Yang, K., Zhang, L., and Zhong, W. (2021). Changing el niño–southern oscillation in a warming climate. *Nature Reviews Earth Environment*, 2(9):628–644.

Cannon, A. J., Alford, H., Shrestha, R. R., Kirchmeier-Young, M. C., and Najafi, M. R. (2022). Canadian large ensembles adjusted dataset version 1 (CanLEADv1):

Multivariate bias-corrected climate model outputs for terrestrial modelling and attribution studies in north america. *Geosci. Data J.*, 9(2):288–303.

Danabasoglu, G., Lamarque, J.-F., Bacmeister, J., Bailey, D. A., DuVivier, A. K., Edwards, J., Emmons, L. K., Fasullo, J., Garcia, R., Gettelman, A., Hannay, C., Holland, M. M., Large, W. G., Lauritzen, P. H., Lawrence, D. M., Lenaerts, J. T. M., Lindsay, K., Lipscomb, W. H., Mills, M. J., Neale, R., Oleson, K. W., Otto-Bliesner, B., Phillips, A. S., Sacks, W., Tilmes, S., Kampenhout, L., Vertenstein, M., Bertini, A., Dennis, J., Deser, C., Fischer, C., Fox-Kemper, B., Kay, J. E., Kinnison, D., Kushner, P. J., Larson, V. E., Long, M. C., Mickelson, S., Moore, J. K., Nienhouse, E., Polvani, L., Rasch, P. J., and Strand, W. G. (2020). The community earth system model version 2 (CESM2). *J. Adv. Model. Earth Syst.*, 12(2).

Deser, C., Knutti, R., Solomon, S., and Phillips, A. S. (2012a). Communication of the role of natural variability in future north american climate. *Nat. Clim. Chang.*, 2(11):775–779.

Deser, C., Phillips, A., Bourdette, V., and Teng, H. (2012b). Uncertainty in climate change projections: the role of internal variability. *Clim. Dyn.*, 38(3-4):527–546.

Deser, C., Phillips, A. S., Alexander, M. A., and Smoliak, B. V. (2014). Projecting north american climate over the next 50 years: Uncertainty due to internal variability. *J. Clim.*, 27(6):2271–2296.

Hartmann, B. and Wendler, G. (2005). The significance of the 1976 pacific climate shift in the climatology of alaska. *Journal of Climate*, 18:4824–4839.

Hartmann, D. L. (2015). Pacific sea surface temperature and the winter of 2014. *Geophysical Research Letters*, 42(6):1894–1902.

Hu, S., Zhang, W., Jin, F.-F., Hong, L.-C., Jiang, F., and Stuecker, M. F. (2023). Seasonal dependence of the Pacific–North american teleconnection associated with ENSO and its interaction with the annual cycle. *J. Clim.*, 36(20):7061–7072.

Karmalkar, A. V. (2018). Interpreting results from the NARCCAP and NA-CORDEX ensembles in the context of uncertainty in regional climate change projections. *Bull. Am. Meteorol. Soc.*, 99(10):2093–2106.

Kay, J. E., Deser, C., Phillips, A., Mai, A., Hannay, C., Strand, G., Arblaster, J. M., Bates, S. C., Danabasoglu, G., Edwards, J., Holland, M., Kushner, P., Lamarque, J.-F., Lawrence, D., Lindsay, K., Middleton, A., Munoz, E., Neale, R., Oleson, K., Polvani, L., and Vertenstein, M. (2015). The community earth system model (CESM) large ensemble project: A community resource for studying climate change in the presence of internal climate variability. *Bull. Am. Meteorol. Soc.*, 96(8):1333–1349.

Kirchmeier-Young, M. C., Zwiers, F. W., and Gillett, N. P. (2017). Attribution of extreme events in arctic sea ice extent. *J. Clim.*, 30(2):553–571.

Klink, K., Fisher, H. D., Force, G. K., Thorpe, J. L., and Young, J. M. (2003). Interannual variability of wind speed and wind power at five tall-tower sites in minnesota (1996-2001). *Phys. Geogr.*, 24(3):183–195.

Kushner, P. J., Mudryk, L. R., Merryfield, W., Ambadan, J. T., Berg, A., Bichet, A., Brown, R., Derksen, C., Déry, S. J., Dirkson, A., Flato, G., Fletcher, C. G., Fyfe, J. C., Gillett, N., Haas, C., Howell, S., Laliberté, F., McCusker, K., Sigmond, M., Sospedra-Alfonso, R., Tandon, N. F., Thackeray, C., Tremblay, B., and Zwiers, F. W. (2018). Canadian snow and sea ice: assessment of snow, sea ice, and related climate processes in canada's earth system model and climate-prediction system. *Cryosphere*, 12(4):1137–1156.

L'Heureux, M. L. and Thompson, D. W. J. (2006). Observed relationships between the el Niño–Southern oscillation and the extratropical zonal-mean circulation. *J. Clim.*, 19(2):276–287.

Lledó, L., Bellprat, O., Doblas-Reyes, F. J., and Soret, A. (2018). Investigating the effects of pacific sea surface temperatures on the wind drought of 2015 over the united states. *J. Geophys. Res.*, 123(10):4837–4849.

Ma, X., Li, Y., and Li, Z. (2022). The projection of canadian wind energy potential in future scenarios using a convection-permitting regional climate model. *Energy Rep.*, 8:7176–7187.

McCabe, G. J., Palecki, M. A., and Betancourt, J. L. (2004). Pacific and atlantic ocean influences on multidecadal drought frequency in the united states. *Proc. Natl. Acad. Sci. U. S. A.*, 101(12):4136–4141.

Pryor, S. C., Barthelmie, R. J., Bukovsky, M. S., Ruby Leung, L., and Sakaguchi, K. (2020). Climate change impacts on wind power generation.

Pryor, S. C., Barthelmie, R. J., Young, D. T., Takle, E. S., Arritt, R. W., Flory, D., Gutowski, W. J., Nunes, A., and Roads, J. (2009). Wind speed trends over the contiguous united states. *Journal of Geophysical Research: Atmospheres*, 114(D14).

Qian, H. and Zhang, R. (2021). Future changes in wind energy resource over the northwest passage based on theCMIP6climate projections. *Int. J. Energy Res.*, 45(1):920–937.

Rodgers, K. B., Lee, S. S., Rosenbloom, N., Timmermann, A., Danabasoglu, G., Deser, C., and Yeager S (2021). Ubiquity of human-induced changes in climate variability. *Earth System Dynamics*, 12(4):1393–1411.

Scinocca, J. F., Kharin, V. V., Jiao, Y., Qian, M. W., Lazare, M., Solheim, L., Flato, G. M., Biner, S., Desgagne, M., and Dugas, B. (2016). Coordinated global and regional climate modeling. *J. Clim.*, 29(1):17–35.

St. George, S. and Wolfe, S. A. (2009). El niño stills winter winds across the southern canadian prairies. *Geophys. Res. Lett.*, 36(23).

Thomson, S. and Vallis, G. (2018a). Atmospheric response to SST anomalies. part I: Background-state dependence, teleconnections, and local effects in winter. *J. Atmos. Sci.*

Thomson, S. and Vallis, G. (2018b). Atmospheric response to SST anomalies. part II: Background-state dependence, teleconnections, and local effects in summer. *J. Atmos. Sci.*

Tuller, S. E. (2004). Measured wind speed trends on the west coast of canada. *Int. J. Climatol.*, 24(11):1359–1374.

von Salzen, K., Scinocca, J. F., McFarlane, N. A., Li, J., Cole, J. N. S., Plummer, D., Verseghy, D., Reader, M. C., Ma, X., Lazare, M., and Solheim, L. (2013). The canadian fourth generation atmospheric global climate model (CanAM4). part I: Representation of physical processes. *Atmosphere-Ocean*, 51(1):104–125.

Wan, H., Wang, X. L., and Swail, V. R. (2010). Homogenization and trend analysis of canadian near-surface wind speeds. *J. Clim.*, 23(5):1209–1225.

Wang, S., Zhu, J., Huang, G., Baetz, B., Cheng, G., Zeng, X., and Wang, X. (2020). Assessment of climate change impacts on energy capacity planning in ontario, canada using high-resolution regional climate model. *J. Clean. Prod.*, 274(123026):123026.

Yang, X., Delworth, T. L., Jia, L., Johnson, N. C., Lu, F., and McHugh, C. (2024). Skillful seasonal prediction of wind energy resources in the contiguous united states. *Commun. Earth Environ.*, 5(1):1–12.

Yuan, J., Tan, B., Feldstein, S. B., and Lee, S. (2015). Wintertime north pacific teleconnection patterns: Seasonal and interannual variability. *J. Clim.*, 28(20):8247–8263.

Zinaman, O., Miller, M., Adil, A., Arent, D., Cochran, J., Vora, R., Aggarwal, S., Bipath, M., Linvill, C., David, A., Futch, M., Kaufman, R., Arcos, E. V., Valenzuela, J. M., Martinot, E., Noll, D., Bazilian, M., and Kumar Pillai, R. (2015). Power systems of the future. *Electr. J.*, 28(2):113–126.